Mechanically Spliced Precast Bridge Columns

Ted Sjurseth
South Dakota State University

MECHANICALLY SPLICED PRECAST BRIDGE COLUMNS

BY

TED SJURSETH

A thesis submitted in partial fulfillment of the requirements for the

Master of Science

Major in Civil Engineering

South Dakota State University

2021

THESIS ACCEPTANCE PAGE

Theodore Sjurseth

This thesis is approved as a creditable and independent investigation by a candidate for the master's degree and is acceptable for meeting the thesis requirements for this degree. Acceptance of this does not imply that the conclusions reached by the candidate are necessarily the conclusions of the major department.

Mostafa Tazarv
Advisor Date

Nadim Wehbe
Department Head Date

Nicole Lounsbery, PhD
Director, Graduate School Date

ACKNOWLEDGEMENTS

This project was jointly funded by the Mountain-Plains Consortium (MPC) – University Transportation Center (UTC) and industry partners including Dayton Superior Corp., Dextra America, Inc., nVent LENTON Corp., Headed Reinforcement Corp., Splice Sleeve North America, Inc., and Contractors Materials Company. Their support and feedback are greatly appreciated. The contents of this report reflect the views of the authors, who are responsible for the facts and the accuracy of the information presented. This document is disseminated under the sponsorship of the Department of Transportation, University Transportation Centers Program, in the interest of information exchange. The U.S. Government assumes no liability for the contents or use thereof.

First, I would like to thank my advisor Dr. Mostafa Tazarv. I am grateful for the guidance he provided throughout the process of conducting this study. He provided me the opportunity to conduct this research and achieve all the goals I set forth at the beginning of my studies.

I would also like to acknowledge my fellow graduate research assistants whom I conferred with throughout my project. Matt LaVoy, Kallan Hart, Evan Greeneway, and undergraduate assistants Selene Renes and Aric Jensen. I am grateful for your assistance and support. I would also like to thank all faculty and staff in the Civil Engineering Department for their assistance especially Lisa Enstad.

Finally, I would like to thank my parents, family, friends and especially my wife Allie for the constant love, support, and encouragement. This would not have been possible without you all.

TABLE OF CONTENTS

LIST OF FIGURES

LIST OF TABLES

ABSTRACT

MECHANICALLY SPLICED PRECAST BRIDGE COLUMNS

THEODORE DAVID SJURSETH

2021

Mechanical bar splices provide an alternative to the traditional method of lap splicing to achieve reinforcement bar continuity in reinforced concrete. Even though mechanical bar splices can be used as new precast column connections to accelerate the bridge construction (ABC), The use of bar couplers in the plastic hinge region of bridge columns is prohibited by the current US codes since the effects of bar couplers on the seismic behavior of columns is not fully investigated. A bridge column including precast columns with couplers located in a high seismic region must be designed to handle large inelastic lateral deformations. The literature lacks a systematic performance database of mechanically spliced bridge columns. An experimental investigation was performed in the Lohr Structures Laboratory at South Dakota State University to determine the seismic performance of mechanically spliced bridge columns and to develop the first-of-its-kind mechanically spliced column performance database. Eight half-scale bridge columns were constructed and tested. However, only the first four columns are included in this document. One column was a cast-in-place (CIP) reference column and three were precast columns that incorporated different coupler products at the base of the precast columns (PGD with Dayton Sleeve-Lock coupler, PGS with NMB Splice Sleeve coupler, and PHD with Dextra Groutec S coupler). All columns were tested under the same slow cyclic displacement-controlled lateral loading. PGD, PGS, and PHD showed a 57, 14,

and 63% reduction in displacement capacity compared to CIP. All columns met the current code seismic requirements thus they are recommended for use in all 50 states of the nation. An analytical study is performed to verify the current modeling methods of bridge columns, specifically mechanically spliced columns. The CIP and precast models were able to successfully reproduce the force-displacement relationship of the columns. Overall, the proposed models were found viable and may be used for the analysis and design of bridge columns incorporating seismic couplers.

Chapter 1. Introduction

1.1 Introduction

Splicing reinforcing bars together is required to be able to achieve continuous members or an assembly of members with a total length longer than one piece of bar. Lap splicing is the conventional method of creating continuous and connected reinforced concrete structural elements. This is done by overlapping the ends of reinforcing bars and essentially splicing the bars together so that force can be transmitted as if there were one continuous reinforcing bar. Lap splicing is generally an adequate method for splicing rebar; however, it can lead to constructability issues in heavily reinforced and precast members.

One alternative to lap splicing is the use of a mechanical bar splice (MBS) also referred to as bar couplers. A bar coupler connects two ends of reinforcing bar through various mechanisms such as grout, threads, shear pins, and other mechanisms. This form of splicing is commonly used in accelerated bridge construction (ABC), but current US codes do not allow the MBS in the plastic hinge region of bridge columns in high seismic regions. Using bar couplers in construction has been shown to have the following benefits: 1) Reduced construction time, 2) reduced reinforcement congestion, 3) lower material costs due to less reinforcement being used, and 4) higher quality assurance.

The use of bar couplers in the plastic hinge region of bridge columns is prohibited by US code likely due to the fact that there is a lack of understanding on the effect of

seismic behavior of bridge columns and that there has not been an experiment conducted verifying column behavior with various configurations such as coupler type, section geometry, aspect ratio, axial load index, etc.

1.2 Objective and Scope

The objective of this study is to determine and verify the effects of mechanical bar splices on the displacement demand and capacity of bridge columns through experimentation. Four, half-scale bridge columns will be tested using cyclic loading. Each column will be connected to a footing using one conventional cast in place connection and seven different coupler connections within the plastic hinge region of the column. Each column will have the same aspect ratio, axial load index, and target ductility and similar cross-sections so that only variable is the connection type. Experimental performance of the columns will be verified with pushover analyses.

1.3 Document Outline

Chapter 1 presents an introduction to this study, scope of work, and a document outline. Chapter 2 presents a comprehensive literature review on coupler material models and performance and columns with coupler connections. Chapter 3 presents the experimental investigation conducted on the effect of seismic behavior of columns with couplers located in the plastic hinge region. Chapter 4 discusses the analytical investigation and verification on the effect of seismic behavior of columns with couplers located in the plastic hinge region. Chapter 5 presents a summary of the study and conclusions drawn from the experimental and analytical investigations.

Chapter 2. Literature Review

2.1 Introduction

Reinforcing bars in concrete structures are conventionally spliced together using lap splices. This can lead to congestion issues in highly reinforced sections. Alternatively, reinforcing bars can be spliced together by means of a mechanical bar splice, also referred to as a bar coupler. Couplers can be used to reduce congestion, cost, and construction while also improving quality control. The US codes currently do not allow couplers to be used in the plastic hinge region of bridge columns in high seismic zones. This section reviews past studies on couplers, especially those that pertain to the coupler effects on bridge column performance.

2.2 Mechanical Bar Splices

Mechanical bar splices are commercially available in several configurations and models produced by different manufacturers, but they are usually classified based on the mechanism utilized to transfer load between two bars: Shear Screw (SS), Headed (HC), Swaged (SW), Threaded (TH), Grouted (GC), or combination of the mechanisms, Hybrid (HY) (Tazarv and Saiidi 2016; Dahal and Tazarv 2020).

2.2.1 Shear Screw Couplers

Shear screw couplers connect two bars together using screws along the length of the coupler as shown in Fig. 2.1. The screws penetrate the bar and transfer the bar forces

through friction between the screws and bar. Shear screw couplers are typically long since it requires several screws to develop full strength to splice the bars.

Figure 2.1. Sample of Shear Screw Couplers (www.bar.us.com)

2.2.2 Headed Couplers

Headed couplers are made of two components that thread together as shown in Fig. 2.2. Headed couplers require the bar ends to be modified by creating an enlarged headed end. The headed end then transfers tension through the bar head bearing on the coupler and the compression through the headed ends bearing on each other. Headed couplers are typically one of the shortest couplers available in the market.

Figure 2.2. Sample of a Headed Couplers (Dahal et al., 2019)

2.2.3 Swaged Couplers

Swaged couplers splice two bars together through friction from a sleeve that is pressed on to the bars (Fig. 2.3). Each end of the bars is inserted into the sleeve and a special tool is used to clamp the sleeve on to the bars. Swaged couplers are typically long to develop the bars.

Figure 2.3. Example of a Swaged Coupler (Dahal et al., 2019)

2.2.4 Threaded Couplers

Threaded couplers have female threads where reinforcing bars with male threaded ends are threaded into. Threads on bars can either be created by forging a threaded component onto the bar or by cutting threads into the bar. Threads may also be either parallel or tapered as shown in Fig. 2.4. Threaded couplers tend to be one of the shortest type of couplers.

(a) Parallel Threaded Coupler (Dahal et al., 2019)

(b) Tapered Threaded Coupler (www.aleno.com)

Figure 2.4. Example of Threaded Couplers

2.2.5 Grouted Couplers

Figure 2.5 shows a grouted coupler in which bars are connected through a bond between the sleeve and a high-strength grout that is pumped into the sleeve after placement. Grouted couplers are typically the longest coupler types. They provide easy installation and allow large construction tolerances.

Figure 2.5. Example of a Grouted Coupler (Dahal et al., 2019)

2.2.6 Hybrid Couplers

Hybrid couplers are mechanical bar splices that use a combination of two or more of the previously mentioned connecting mechanisms. Figure 2.6 shows a hybrid coupler that uses a threaded connection at one end and grouted connection at the other. Use of hybrid couplers can be advantageous by combining the benefits of various coupler types.

Figure 2.6. Example of a Threaded-Grouted Hybrid Coupler (Dahal et al., 2019)

2.3 Material Model for Couplers

Couplers very in their shapes, sizes, lengths, thicknesses, and anchoring mechanisms, making them difficult to model and estimate their engineering behavior. A few studies have proposed models to simulate the coupler material behavior (Haber et al, 2015; Tazarv and Saiidi 2016; Ameli 2016). The coupler stress-strain material model developed by Tazarv and Saiidi (2016) was adopted in this study. A brief overview of this model is presented in the following section.

2.3.1 Material Model by Tazarv and Saiidi (2016)

Figure 2.7 shows of the key parameters of a mechanical bar splice defined by Tazarv and Saiidi. When a spliced bar is in tension, only a portion of the coupler is considered to contribute to the overall elongation while the remaining portion is assumed to be rigid. The rigid portion of the coupler (βL_{sp}) is due to the coupler anchoring mechanism. The coupler rigid length factor (β) estimates what length of the coupler does not contribute to the splice elongation. The rigid length factor can be different for different couplers and should be determined through experiment. The length of the

coupler region (L_{cr}) is the physical length of the coupler (L_{sp}) plus a distance (α times the bar diameters, αd_b) form each end of the coupler. Subjected to the same tensile force, the unspliced reference bar will elongate more than a spliced bar due to the coupler rigidity. Therefore, the strain of the unspliced bar (ε_s) will be greater than the strain of the corresponding spliced bar (ε_{sp}). Equation 2.1 or 2.2 can be used to relate the coupler stains to the reference bar strains.

$$\frac{\varepsilon_{sp}}{\varepsilon_s} = \frac{L_{cr} - \beta L_{sp}}{L_{cr}} \qquad \text{(Eq. 2-1)}$$

$$\frac{\varepsilon_{sp}}{\varepsilon_s} = \frac{(1-\beta)L_{sp} + 2\alpha d_b}{L_{sp} + 2\alpha d_b} \qquad \text{(Eq. 2-2)}$$

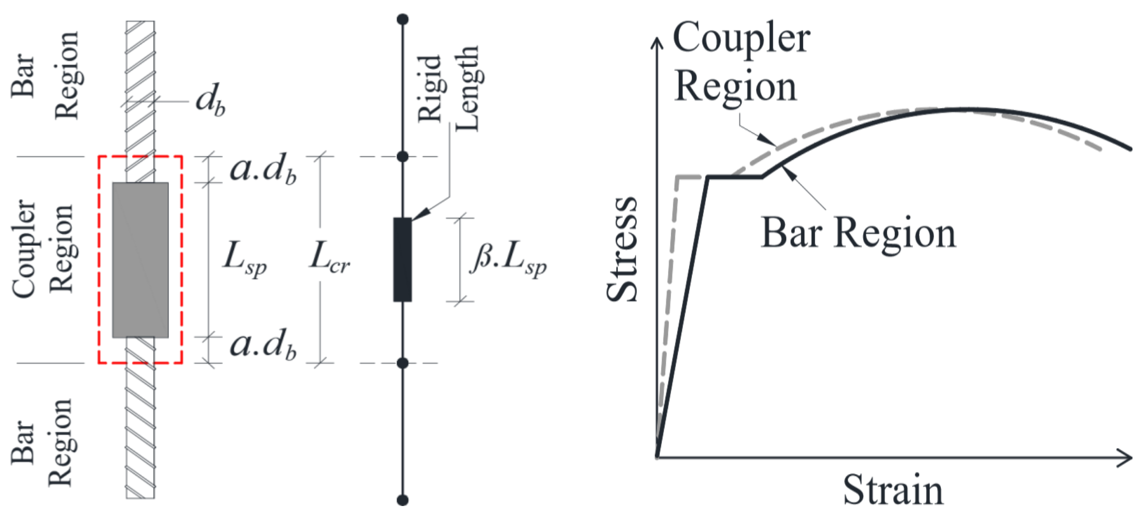

(a) Regions of a Mechanical Bar Splice (b) Stress-Strain Model

Figure 2.7. Stress-Strain Model for Mechanical Bar Splices by Tazarv and Saiidi (2016)

The model assumes that a tensile failure would happen outside of the coupler region (such splices were named as “seismic couplers”), therefore the coupler can be

modeled independent of stress properties. Rather, the strain properties of a reference bar can be modified to obtain the strain properties of the coupler.

The coupler rigid length factor (β) is the key to determine the stress-strain relationship of a mechanical bar splice. A spliced connection with a rigid length factor of zero would be emulative of a reference unspliced bar. As the rigid length factor increases the strain of the spliced connection decreases.

2.3.1.1 Study by Dahal and Tazarv (2020)

This study aimed to determine the behavior of mechanical bar splices through an extensive experimental work. The study developed a first-of-its-kind database for coupler performance and established the coupler properties in accordance with the modeling method proposed by Tazarv and Saiidi (2016). The study tested more than 160 mechanical bar splices including No. 5 (16-mm), No. 8 (24-mm), and No. 10 (32-mm) bars. The splices were tested to failure using both uniaxial monotonic and cyclic tensile loading. Table 2.1 presents the recommended coupler rigid length factors for different coupler types and sizes. Note that the manufacturer Erico was purchased by nVent. Coupler connections may fail by bar pullout from the coupler, coupler rupture, bar fracture within the coupler region, or bar fracture outside the coupler region. A coupler is only considered a seismic coupler if it consistently fails by bar rupture outside the coupler region.

Table 2.1. Coupler Rigid Length Factors Recommended by Dahal et al. (2019)

Coupler Type	No. 5 (16 mm)	No. 8 (24 mm)	No. 10 (32 mm)
Headed Reinforcement	0.80	0.75	0.55
Threaded (Dextra-Type A)	1.70	1.5	1.60
Threaded (Dextra-Type B)	1.60	1.5	1.65
Threaded (Erico)	0.95	1.10	1.05
Swaged	0.90	0.90	0.95
Grouted Sleeve (NMB)	0.95	0.65	0.85
Grouted Sleeve (Dayton)	0.70	0.70	0.65
Hybrid (Dextra)	0.80	0.90	0.85
Hybrid (Erico)	0.80	0.80	0.80

A parametric study was also performed in this work to investigate the seismic performance of bridge columns incorporating different couplers using the recommended rigid length factors. More than 240 pushover analyses were performed on columns with varying aspect ratio, axial load index, and ductility. Couplers were modeled using the Tazarv's model. It was found that the coupler size, type, and length all significantly affect the ductility of a bridge column. It was generally observed that columns with longer and/or higher rigid length factors showed lower displacement capacities.

2.4 Mechanically Spliced Columns

Tazarv and Saiidi (2016) conducted a state-of-the-art review of mechanical bar splices and mechanically spliced columns. The present literature review is to discuss the key past studies and to complement the review conducted by Tazarv and Saiidi (2016) with new studies became available afterwards.

2.4.1 Study by Haber et al. (2014)

Haber et al. developed new connections using headed (HC) and grouted (GC) couplers for accelerated bridge construction in regions of high seismicity. Figure 2.8 shows the two precast connections. The study tested five half-scale columns. Two of the

columns were attached to their footing with no intermediate sections labeled as “No Pedestal” (NP). Two other columns were attached to their footing via a precast pedestal (PP). Grouted couplers were used in two models and headed couplers were used in two other columns. The fifth column was a conventional cast-in-place model that served as the reference.

(a) Headed Coupler with Precast Pedestal (HCPP)

(b) Headed Coupler No Pedestal (HCNP)

Figure 2.8. Half-Scale Precast Columns Tested by Haber et al. (2014)

Figure 2.9 shows the force-displacement response of the four precast columns. The columns that used headed couplers exhibited similar performance to the cast-in-place reference column. The columns spliced with grouted couplers only achieved a maximum drift ratio of 6% while the cast-in-place column was able to reach a maximum drift ratio of 10%. The drift ratio is the ratio of the column lateral displacement to the column height. The study concluded that precast connections incorporating mechanical bar splices are feasible and are suitable for accelerated bridge construction in high seismic regions of the nation.

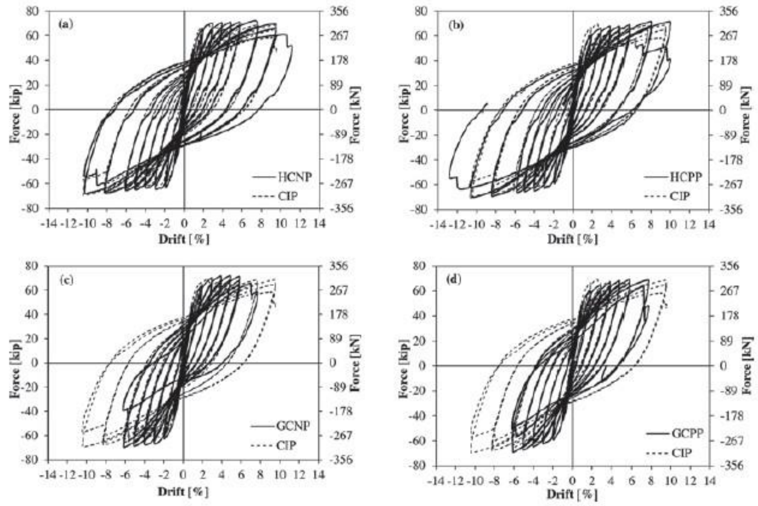

Figure 2.9. Force-Displacement Responses of Half-Scale Precast Columns by Haber et al. (2014)

2.4.2 Study by Tazarv and Saiidi (2014)

Tazarv and Saiidi (2014) conducted a study in which three half-scale precast bridge columns were tested (PNC, GCDP, and HCS). PNC used a connection in which reinforcing bar dowels extended from the column base into corrugate galvanized steel ducts that were embedded in the footing. The ducts were filled with ultra-high-performance concrete (UHPC). GCDP used grouted couplers and the bars were debonded near the coupler to reduce strain concentrations. GCDP also utilized a pedestal at the column-footing connection to shift the coupler higher in the plastic hinge region. Similar to PNC, HCS also used steel ducts in the footing. However, HCS used materials such as shape memory alloy (SMA), engineered cementitious composite (ECC), and headed bar couplers at the base of column. Figure 2.10 shows detailing of the precast columns.

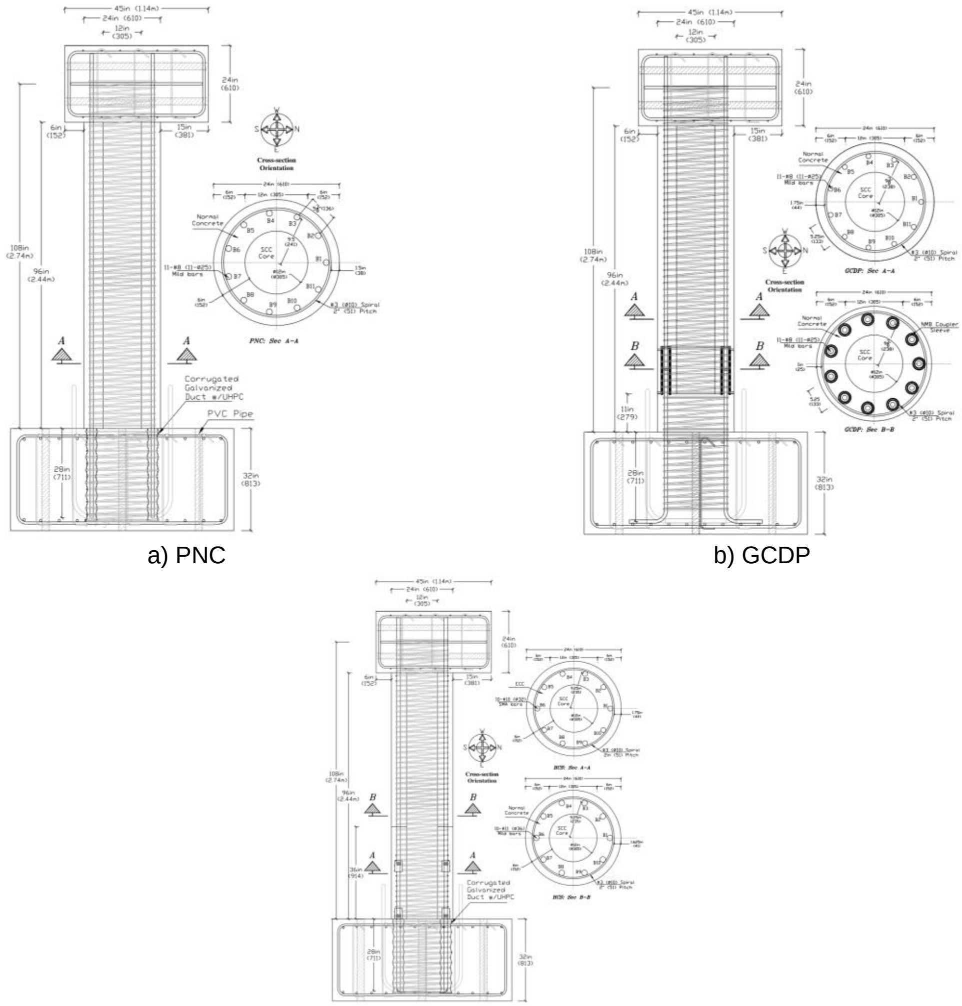

a) PNC b) GCDP

c) HCS

Figure 2.10. Half-Scale Precast Columns Tested by Tazarv and Saiidi (2014)

All columns failed due to longitudinal bar rupture and had large displacement capacities. The displacement capacities of PNC, GCDP, and HCS were 8, 8, and 10% respectively. PNC and GCDP had a 10% and 12% reduction in displacement capacity compared to a cast-in-place (CIP) reference column from a prior study (Haber 2014). HCS had 5% increase in displacement capacity than (CIP). Overall, the force-displacement relationship of the precast models was similar to the reference. Figure 2.11 shows the force-displacement relationship of the precast columns.

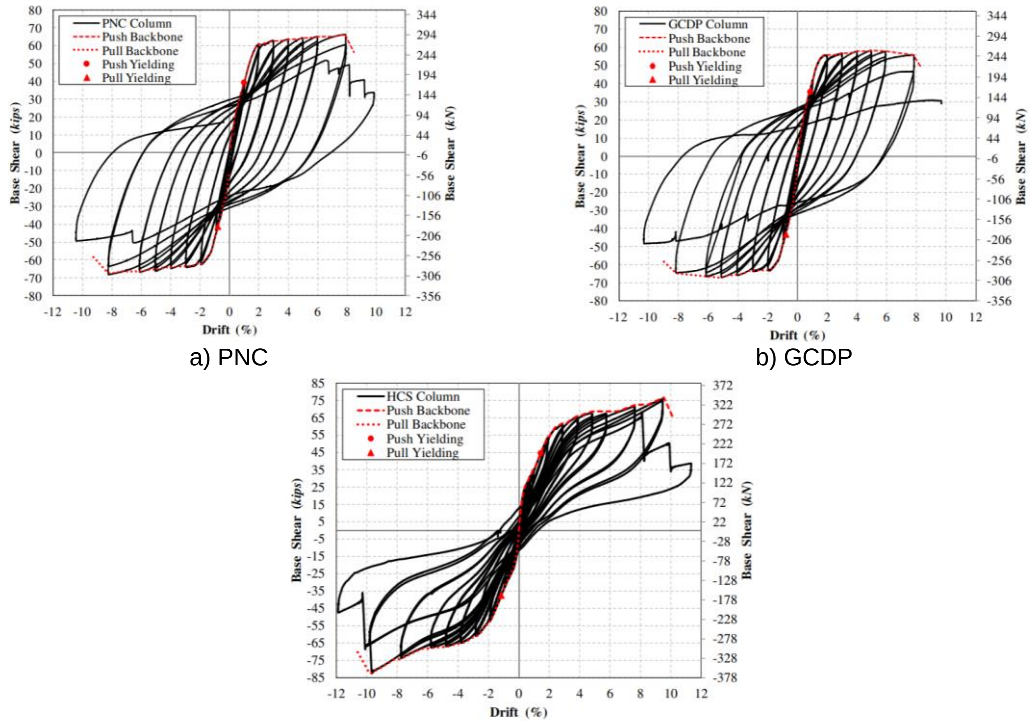

a) PNC b) GCDP

c) HCS

Figure 2.11. Force-Displacement Responses of Half-Scale Precast Columns by Tazarv and Saiidi (2014)

2.4.3 Study by Tazarv and Saiidi (2016)

Tazarv and Saiidi (2016) proposed the minimum acceptance criteria for couplers to be incorporated in the plastic hinge region of bridge columns as:

1) The total length of the mechanical bar coupler (L_{sp}) shall be no greater than $15d_b$ where d_b is the diameter of the smallest of two spliced bars.
2) A spliced bar shall fracture outside the coupler region regardless of loading scenario. The coupler region is defined as the physical length of the coupler plus $1.0d_b$ beyond each end of the coupler. Only ASTM A706 reinforcing bars shall be used in seismic regions.

Tazarv and Saiidi did not test any columns in this study. However, they performed an extensive analytical study and proposed modeling and design methods for

mechanically spliced bridge columns based on the analytical findings and data available from previously tested specimens.

2.4.43 Study by Ameli et al. (2014)

This study focused on determining the seismic performance of columns connected at the base using grouted couplers. Six half-scale precast bridge columns were tested using grouted couplers. Three of which were for a column-footing connection (GGSS) and three were for a column-cap beam connection (FGSS). A cast-in-place column was also tested for each connection type as the reference. Figure 2.12 shows the detailing of the precast columns with grouted couplers and cast-in-place columns.

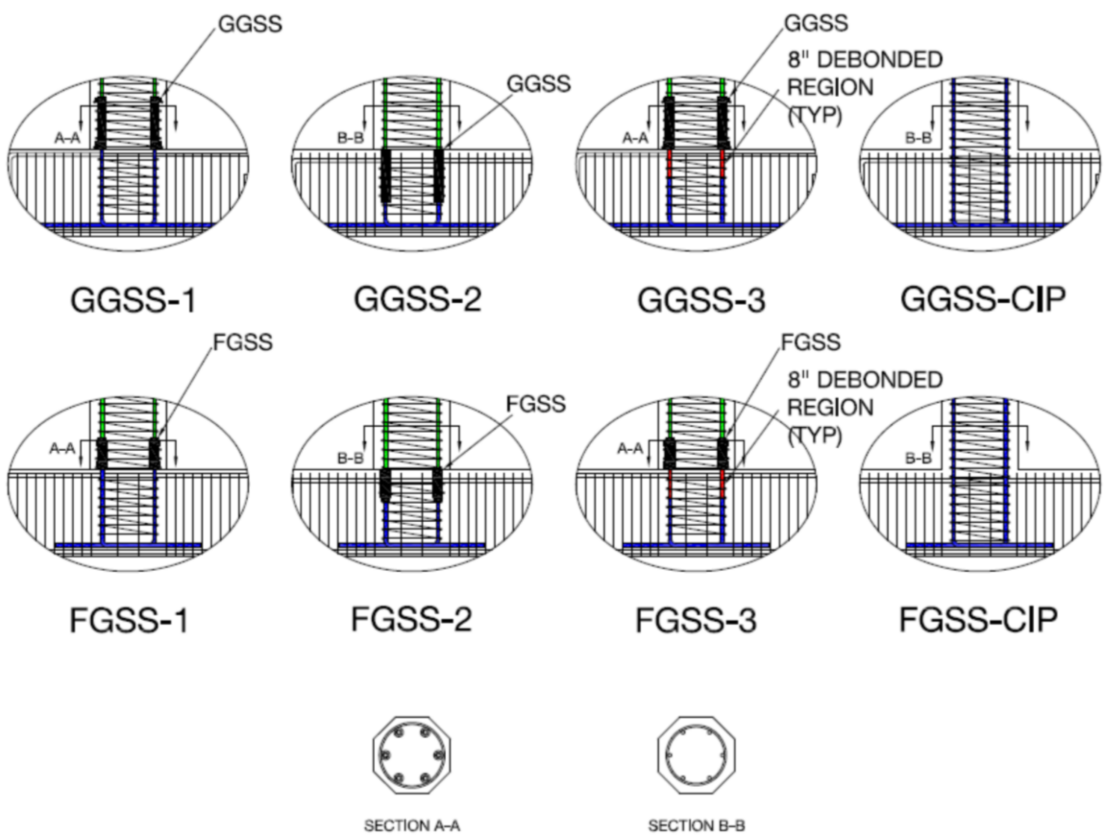

Figure 2.12. Half-Scale Precast Columns with Grouted Couplers Tested by Ameli et al. (2014)

The seismic performance of the precast columns was evaluated by placing the couplers at two alternative locations:

1) Couplers placed in the plastic hinge region with and without intentional debonding.

2) Couplers placed in the footing or cap beam.

The columns were tested laterally under cyclic loading to failure. The columns had an axial load index of 6% (the ratio of the column axial load to the product of the column concrete compressive strength and the column cross-section area). Figure 2.13 shows the force-displacement response of each column. The study concluded that the precast detailings were expected to perform adequately in high seismic regions.

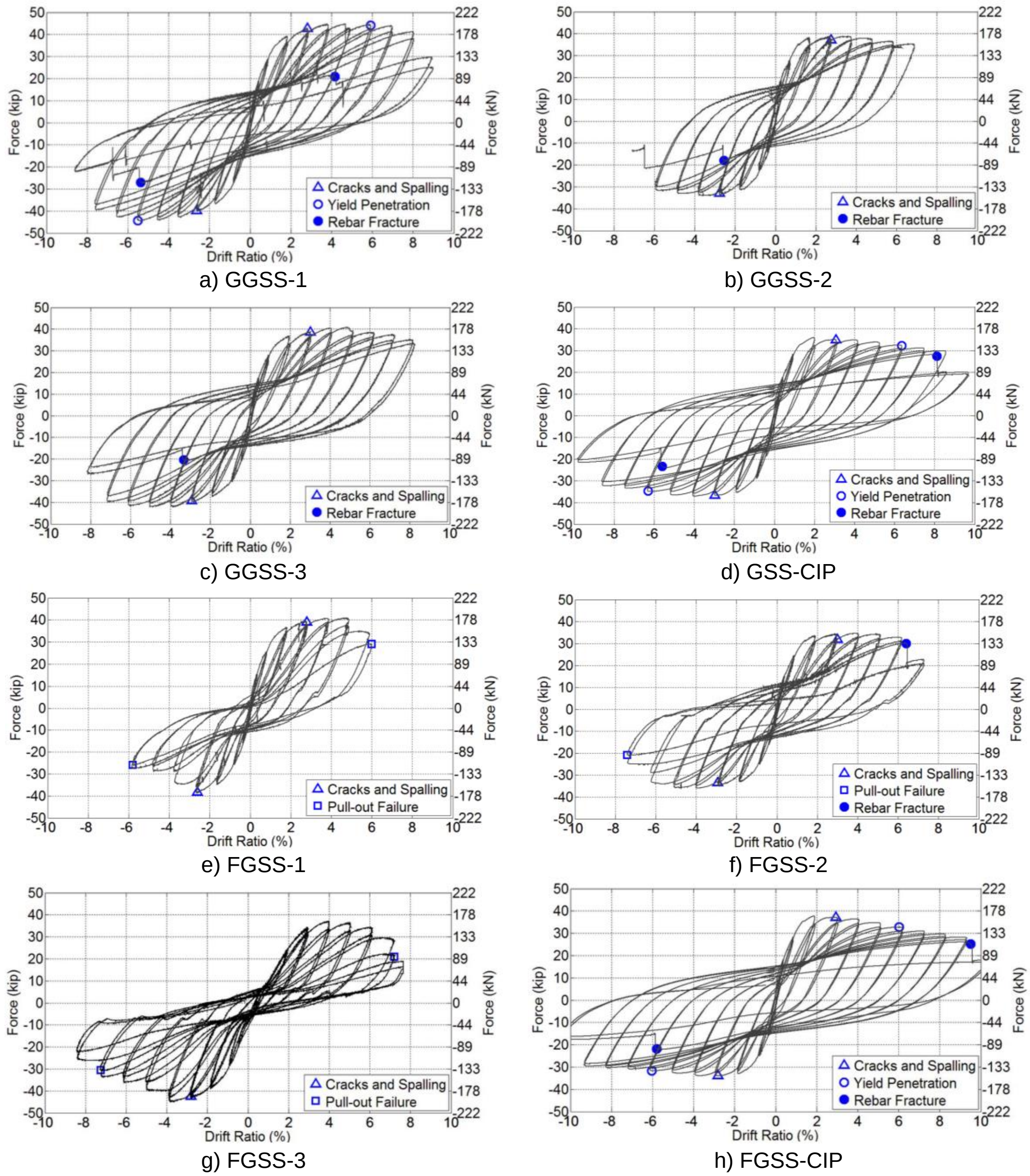

Figure 2.13. Force-Drift Responses of Half-Scale Precast Columns Tested by Ameli et al. (2014)

2.4.5 Study by Wang et al. (2018)

This study tested seven square, large-scale bridge columns of which three were relevant to the current study. One column was constructed as a conventional cast-in-place column to serve as the reference model. The other two relevant columns were precast and connected to the footing with grouted couplers embedded in either the footing

or the column (Fig. 2.14). The columns were subjected to quasi-static unidirectional lateral loading with a displacement-controlled loading. Figure 2.15 shows the full force-displacement relationship of each column. The column with the couplers embedded in the footing had a 15% reduction in ductility compared with the cast-in-place column. The column with couplers embedded at the base of the column had a 1.4% reduction in ductility compared with the reference column.

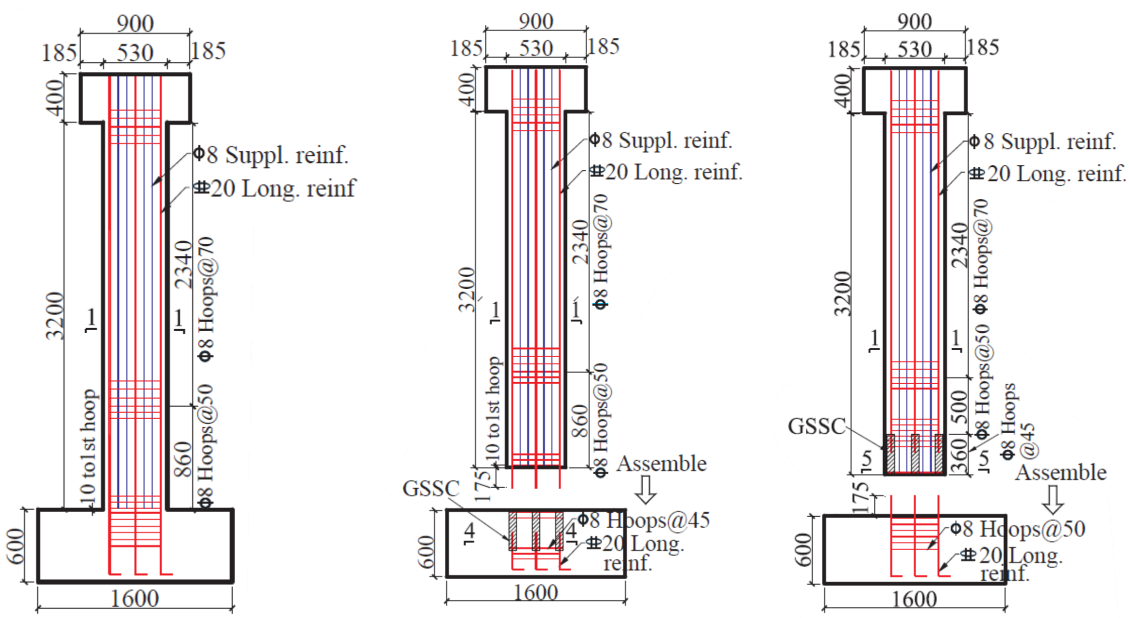

(a) CIP Section (b) Couplers Embedded in Footing (c) Couplers at Base of Column

Figure 2.14. Half-Scale Precast Columns tested by Wang et al. (2018)

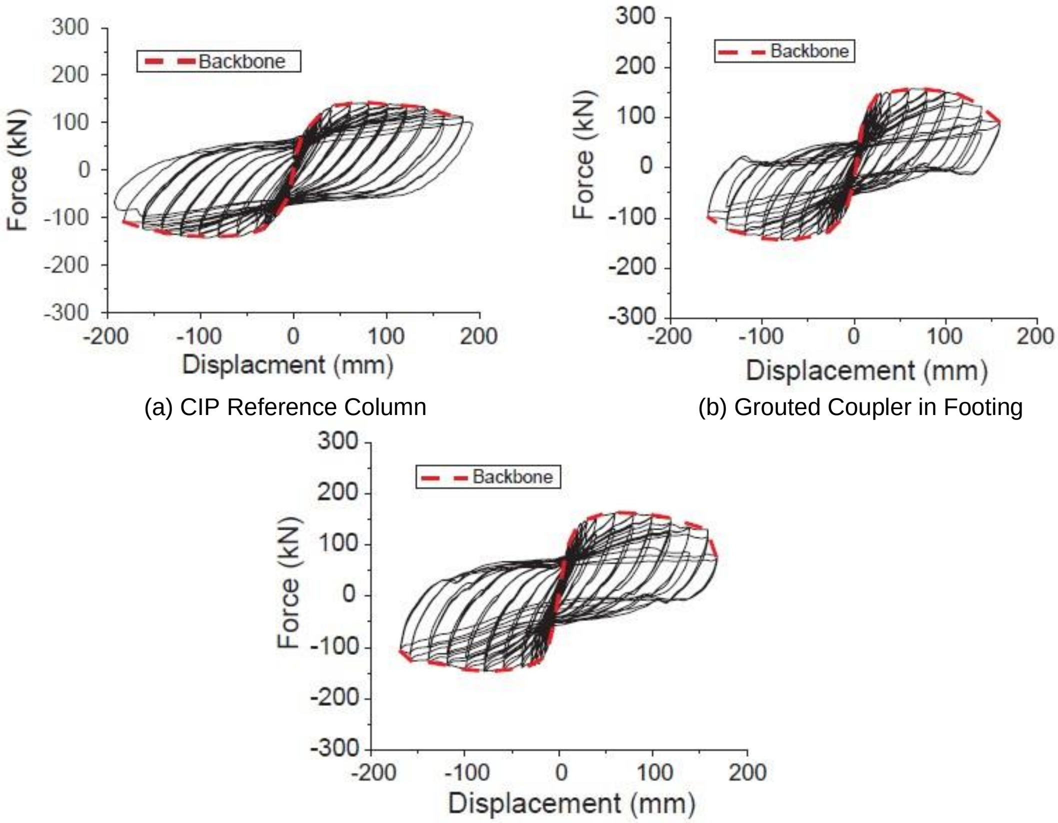

(a) CIP Reference Column (b) Grouted Coupler in Footing

c) Grouted Coupler in Column Base

Figure 2.15. Force-Displacement Response of the Large-Scale Columns Tested by Wang et al. 2018

2.4.6 Study by Bompa and Elghazouli (2019)

This study conducted an experimental investigation on the inelastic cyclic performance of reinforced concrete members that incorporated threaded couplers. Four beam-column specimens were tested, one had conventional continuous reinforcement which served as the reference model while the other three used a threaded coupler embedded at the column base. Figure 2.16 shows the specimen detailing. Of the three columns with couplers, one column used a considerably longer, hybrid swaged-threaded coupler. The last two specimens incorporated a shorter, compact coupler. One of the columns with the compact coupler was subjected to an axial load index of 15% during testing while the other columns had no axial load. Each column was subjected to quasi-static lateral cyclic loading until failure. The column named “C300-C0-N0” was the

reference column. "C300-CC-N0" and "C300-CC-N1" were the columns that used the compact couplers and had axial load indexes of 0.0% and 15%, respectively. "C300-CS-N0" was the column that used the slender hybrid swaged-threaded couplers.

Figure 2.17 shows the full force-displacement relationship of the columns. "C300-CC-N1" exhibited a higher lateral resistance but experienced strength degradation from concrete spalling and a 36% reduction in displacement capacity. The other specimens showed similar performance to each other.

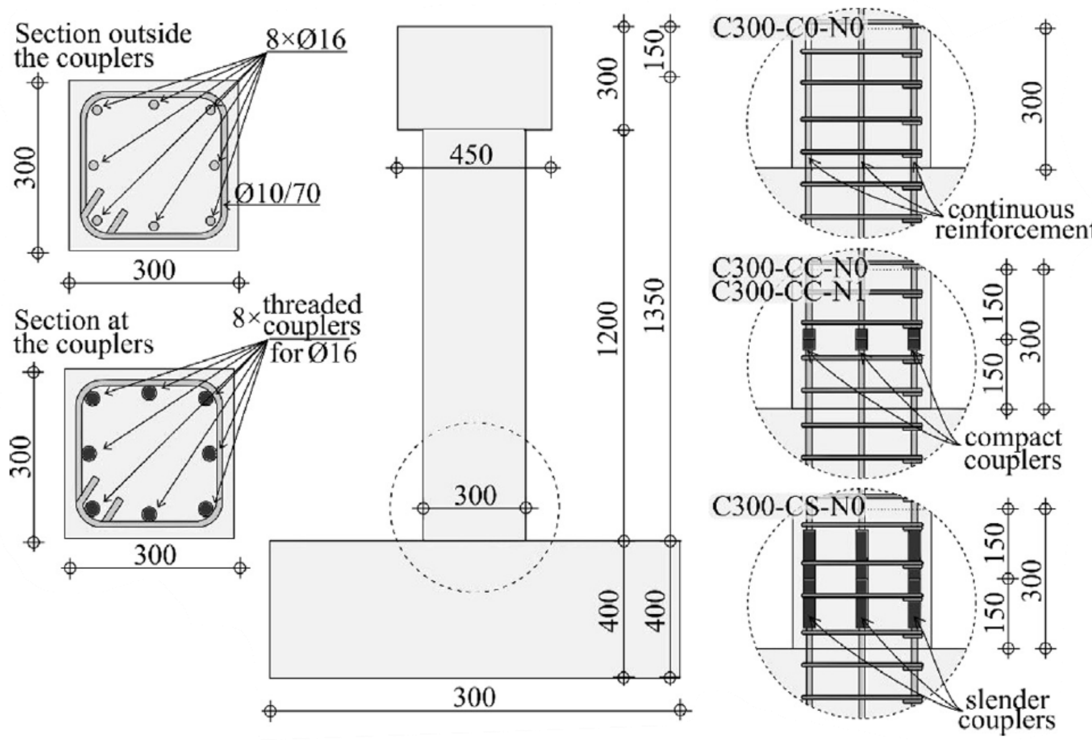

Figure 2.16. Details of Large-Scale Columns Tested by Bompa and Elghazouli (2019)

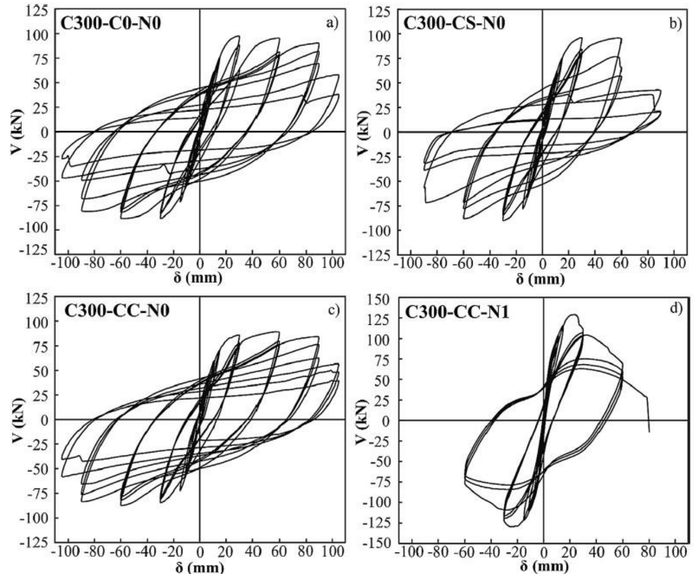

Figure 2.17. Force-Displacement Response of the Large-Scale Columns Tested by Bompa and Elghazouli (2019)

2.4.7 Study by Lavoy (2020)

This study conducted an analytical investigation to determine the effects that couplers have on seismic displacement demand and capacity when embedded at the base of the column. Analyses were performed on cast-in-place reference columns and columns that used nine different types of couplers. A total of 405 pushover analyses and 540 nonlinear dynamic analyses were completed on columns with various aspect ratios, axial load indices, displacement ductility, and either square or circular cross sections. Figure 2.18 shows the column analytical model and Fig. 2.19 shows a summary of the analyses. It was found that mechanically spliced columns generally exhibited lower displacement capacities compared with unspliced columns. The displacement capacity decreased as the coupler length and the coupler rigid length factor increased. Couplers had more profound effects on the displacement capacity when the columns had a lower aspect ratio, a lower axial load index, and had large displacement capacities in their reference unspliced versions. Couplers were found to reduce the displacement ductility

capacity of a bridge column by up to 45%. Furthermore, it was found that couplers have a minimal effect on the column displacement demands, not exceeding 8 %.

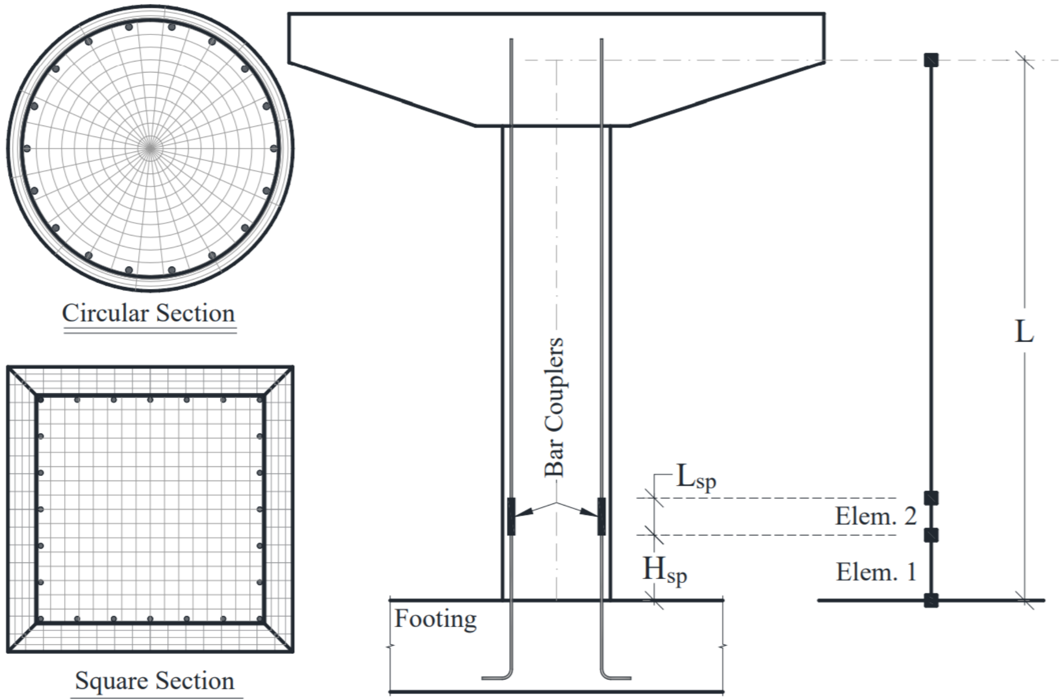

Figure 2.18. Mechanically Spliced Column Analytical Model (LaVoy 2020)

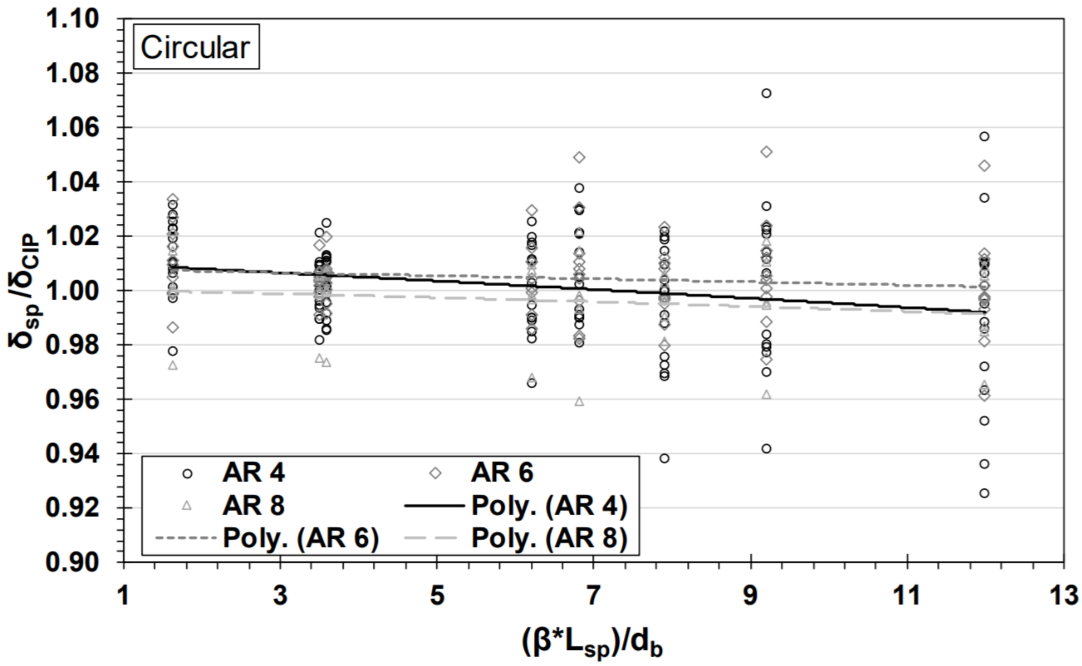

a) Summary Plot of Seismic Demand Analysis

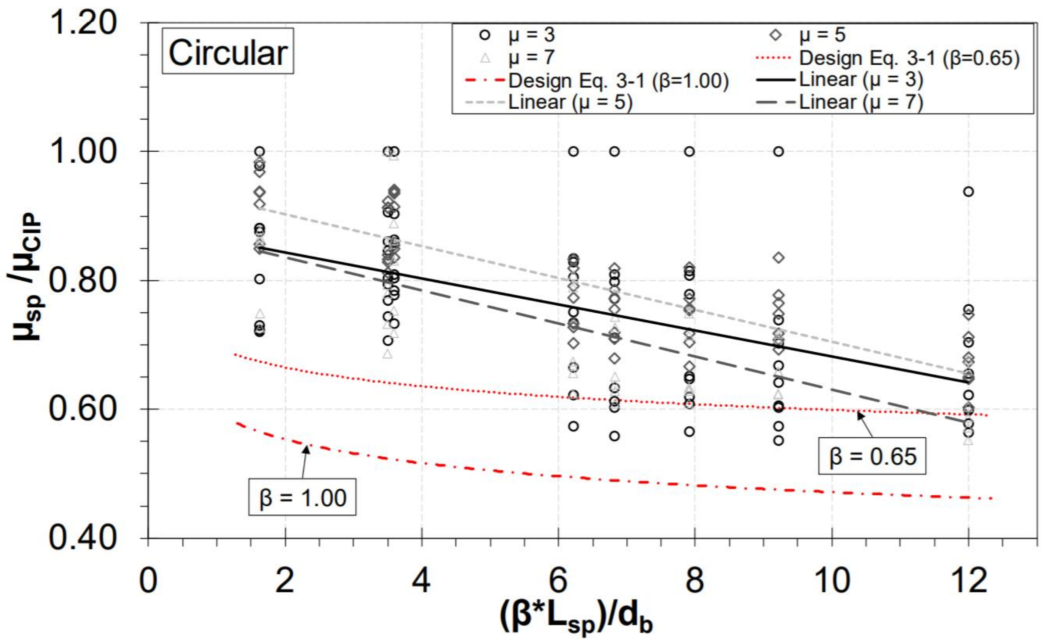

b) Capacity

Figure 2.19. Summary Plots of Seismic Demand and Capacity Analysis

2.5 References

Ameli, M.J., Brown, D.N., Parks, J.E., and Pantelides, C.P. (2014). "Seismic Evaluation of Grouted Splice Sleeve Connections for Precast RC Bridge Piers in ABC." Utah Department of Transportation, Research Division, Report No. UT-14.09.

Ameli, M.J., Brown, D.N., Parks, J.E., and Pantelides, C.P. (2016). “Seismic Column-to Footing Connections Using Grouted Splice Sleeves.” ACI Structure Journal, Vol. 113, No. 5, pp.1021-1030

Ameli, M.J. and. Pantelides, C.P (2016). “Seismic Analysis of Precast Concrete Bridge Columns Connected with Grouted Splice Sleeve Connectors.” Journal of Structural Engineering, 10.1061/(ASCE)ST.1943-541X.0001678, ASCE, Vol 143, No. 2.

Bompa, D.V., Elghazouli, A.Y. (2019), “Inelastic Behaviour of RC Members Incorporating Threaded Reinforcement Coupler.” Engineering Structures, DOI: 10.1016/j.engstruct.2018.11.053, Vol. 180, pp.468-483.

Dahal, P.K., Tazarv, M., and Wehbe, N. (2019). “Mechanical Bar Splices for Accelerated Construction of Bridge Columns,” North Dakota State University - Upper Great Plains Transportation Institute, Fargo: Mountain-Plains Consortium (MPC), MPC Report No. 19-372, 142 pp.

Dahal, P.K., and Tazarv, M. (2020). “Mechanical Bar Splices for Incorporation in Plastic Hinge Regions of RC Members,” Construction and Building Materials, Vol. 258, 120308, 17 pp.

Haber, ZB, Saiidi, MS, and Sanders, DH (2013). “Precast Column Footing Connections for Accelerated Bridge Construction in Seismic Zones.” Rep. No. CCEER 13-08 Center for Civil Engineering Earthquake Research, Dept. of Civil and Environmental Engineering, Univ. of Nevada, Reno. NV.

LaVoy, Mathew Ray, "Seismic Performance of Mechanically Spliced Bridge Columns through Analytical Studies" (2020). *Electronic Theses and Dissertations*. 3677.

Tazarv, M. and Saiidi, M.S. (2014). "Next Generation of Bridge Columns for Accelerated Bridge Construction in High Seismic Zones," Center For Civil Engineering Earthquake Research, Department of Civil and Environmental Engineering, University of Nevada, Reno, Nevada, Report No. CCEER-14-06, 400 pp.

Tazarv, M. and Saiidi, M.S. (2016). "Seismic Design of Bridge Columns Incorporating Mechanical Bar Splices in Plastic Hinge Regions," Engineering Structures, DOI: 10.1016/j.engstruct.2016.06.041, Vol 124, pp. 507-520

Wang, Z., Qu, H., Li, T., Wei, H., Wang, H., Duan, H. (2018). "Quasi-Static Cyclic Tests of Precast Bridge Columns with Different Connection Details for High Seismic Zones," Engineering Structures, DOI: 10.1016/j.engstruct.2017.12.035, Vol 158, pp. 13-27.

Chapter 3. Experimental Investigation

3.1 Introduction

A bridge column in a region with high seismic demand must be designed to handle large inelastic lateral deformations. An experimental investigation was performed in the Lohr Structures Laboratory at South Dakota State University to determine the seismic performance of mechanically spliced bridge columns. This chapter discusses the following items:

- Test matrix,
- Design and construction,
- Test setup,
- Instrumentation,
- Loading protocol, and
- Test results.

3.2 Test Matrix

A total of eight columns were initially planned to be tested in this project. However, due delays (mainly caused by the COVID-19 pandemic), seven columns have been built so far and five columns were tested. This thesis only covers the construction and testing of first four columns including one reference cast-in-place and three precast columns. The precast column test parameters were:

- Coupler Type

- Coupler Length (one may also relate it to the coupler diameter)
- Coupler Rigid Length Factor
- Connection Detailing

Table 3.1 presents the test matrix for the four columns discussed above. The specimens were identified by two broad classifications, cast-in-place (CIP) and precast (with a three-letter naming system starting with "P"). The second letter in the precast column name identifies the coupler type; "G" for grouted, "H" for hybrid combination of coupling mechanisms. The last letter of the precast column name identifies the coupler manufacturer; "D" for Dayton Superior, "S" for Splice Sleeve North America, and "D" for Dextra. Four feasible connection detailing alternatives shown in Fig. 3.1 were proposed for the precast specimens. Each specimen was detailed according to the alternative deemed most feasible. Note than other detailing alternatives were used in the other four columns that were not discussed in this thesis.

Table 3.1. Column Test Matrix

SP ID	Coupler Type	Manufacturer, Model	Coupler Length, $L_{sp,}$ and Diam., in. (mm)	Coupler Rigid Length Factor, β	Remark
CIP	N/A	N/A	N/A	N/A	Reference cast-in-place
PHD	Hybrid (Grouted-Threaded)	Dextra America, Inc., Groutec S with Bartec	9.45 (240) 2.17 (55)	0.79 (Based on present study)	Use ALT1 detailing
PGD	Grouted	Dayton Superior Corp., Sleeve Lock	16.5 (419) 2.89 (73)	0.70	Use ALT1 detailing
PGS	Grouted	Splice Sleeve North America, Inc., NMB	14.57 (370) 2.52 (64)	0.65	Use ALT1 detailing

Note: Coupler properties are for No. 8 (25-mm) bars based on a previous study at SDSU by Dahal and Tazarv (2020).

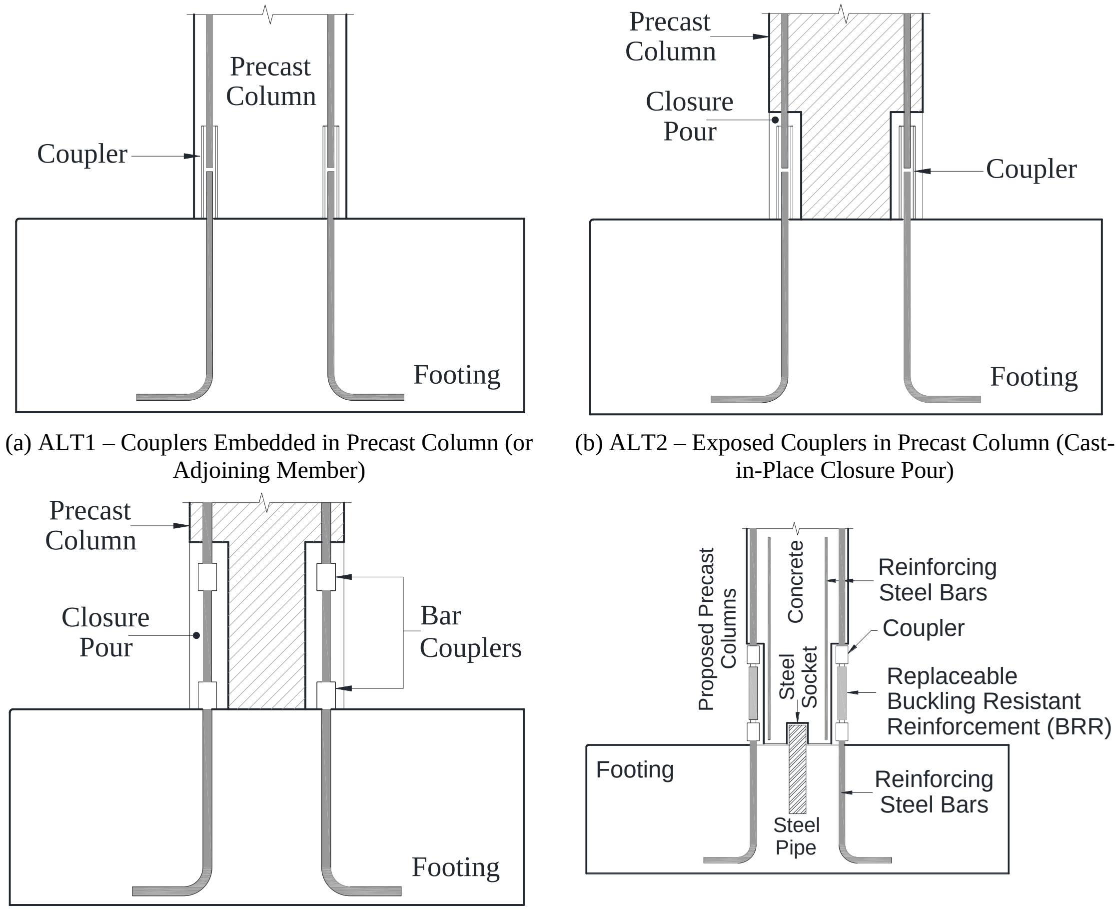

(a) ALT1 – Couplers Embedded in Precast Column (or Adjoining Member)

(b) ALT2 – Exposed Couplers in Precast Column (Cast-in-Place Closure Pour)

(c) ALT3 – Exposed Two-Level Couplers in Precast Column (Cast-in-Place Closure Pour)

(d) ALT4 – Repairable Precast Columns

Figure 3.1. Feasible Connection Details for Mechanically Spliced Precast Columns

3.3 Design and Construction of Column Specimens

This section presents a summary of the design and construction of the test specimens.

3.3.1 CIP Column Model

The test column overall geometry was determined based on a previous analytical study at SDSU in which it was found that coupler effects are more profound on columns with low aspect ratios, low axial loads, and a high displacement capacity. The coupler effect was the highest for a column with an aspect ratio (the column height to the column

diameter) of 4, an axial load index (the ratio of the column axial load to the product of concrete strength and the column cross-sectional area) of 5%, and a displacement ductility capacity of 7.0 (LaVoy, 2020). Therefore, these properties were adopted for the design of the reference test specimen. Furthermore, the final product of this study is new precast columns for bridges. Precast plants usually function in horizontal pour and specimen preparation in the vertical direction is limited. Even though circular reinforced concrete (RC) columns are the best and the most common shape for seismic performance due to high confinement provided by hoops, a rectilinear in lieu of curvilinear cross-section is preferred for precast products (Hewes, 2013). Therefore, an octagonal cross-section with circular bar arrangement was selected in this study for testing.

The prototype conventional CIP column was designed based on AASHTO SGS (2011) (also Caltrans Seismic Design Criteria (SDC) Version 2.0 (2019) was used). As discussed before, CIP serves as the reference column to comment on the performance of the mechanically spliced precast columns. The CIP model was a typical bridge column, but a thicker clear cover was used to account for the coupler diameter in the precast specimens. Due to the test setup limitation, a half-scale model of the prototype column was selected for testing. The scaling of the column properties was based on the recommendations by Krawinkler and Moncarz (1982).

Based on the abovementioned requirements and limitations, the cross section of the test specimen was selected to be octagonal with a medium diagonal of 24 in. (610 mm) and a height of 8 ft (2.44 m), from the top of the footing to the centerline of the hydraulic actuator used to apply lateral loads, resulting in an aspect ratio of 4.

The reinforcement schedule for the CIP column model was 10-#8 (10-Ø25 mm) longitudinal bars and #3 (Ø10 mm) transverse hoops spaced at 2 in. (51 mm) resulting in a longitudinal steel ration and a transverse volumetric steel ratio of 1.66% and 1.86%, respectively. Figure 3.2 shows the CIP column model reinforcement detailing. The axial load index was 5%. The column was designed with a concrete compressive strength of 6000 psi (41.4 MPa) and ASTM A706 bar was used for all reinforcement. The column was designed to achieve a minimum displacement ductility capacity of 7 based on Caltrans SDC (2019).

To secure the actuator to the column, the column cross-section at the tip was changed from octagonal to square with a side dimension of 24 in. (610 mm). PVC pipes were used to make holes to layer fix the actuator to the column using high-strength threaded rods.

To minimize test variations, only one batch of longitudinal reinforcement was used in all columns (expect the repairable column that is not included in this thesis). As the result, the single-batch A706 longitudinal reinforcement was purchased from a provided in Ohio, was shipped either to the coupler manufacturers for end preparation or to the Lohr Structures Laboratory for direct use in the columns. CIP was constructed at SDSU. However, Gage Brothers, a leading precast company in the region located in Sioux Falls, SD, was hired to construct the precast columns. To further minimize the test variations, the Gage Brother concrete mix design was used to mix the CIP column concrete.

The CIP column was constructed vertically at the Lohr Structures Laboratory by first casting the footing with the column cage embedded (Fig. 3.3) followed by casting

the column itself (Fig. 3.4). A ready mixed concrete company was hired to prepare the concrete for the CIP footing and column following the precast concrete mix design with a target design compressive strength of 6000 psi (41.4 MPa). Samples were collected and slump tests were performed before placement.

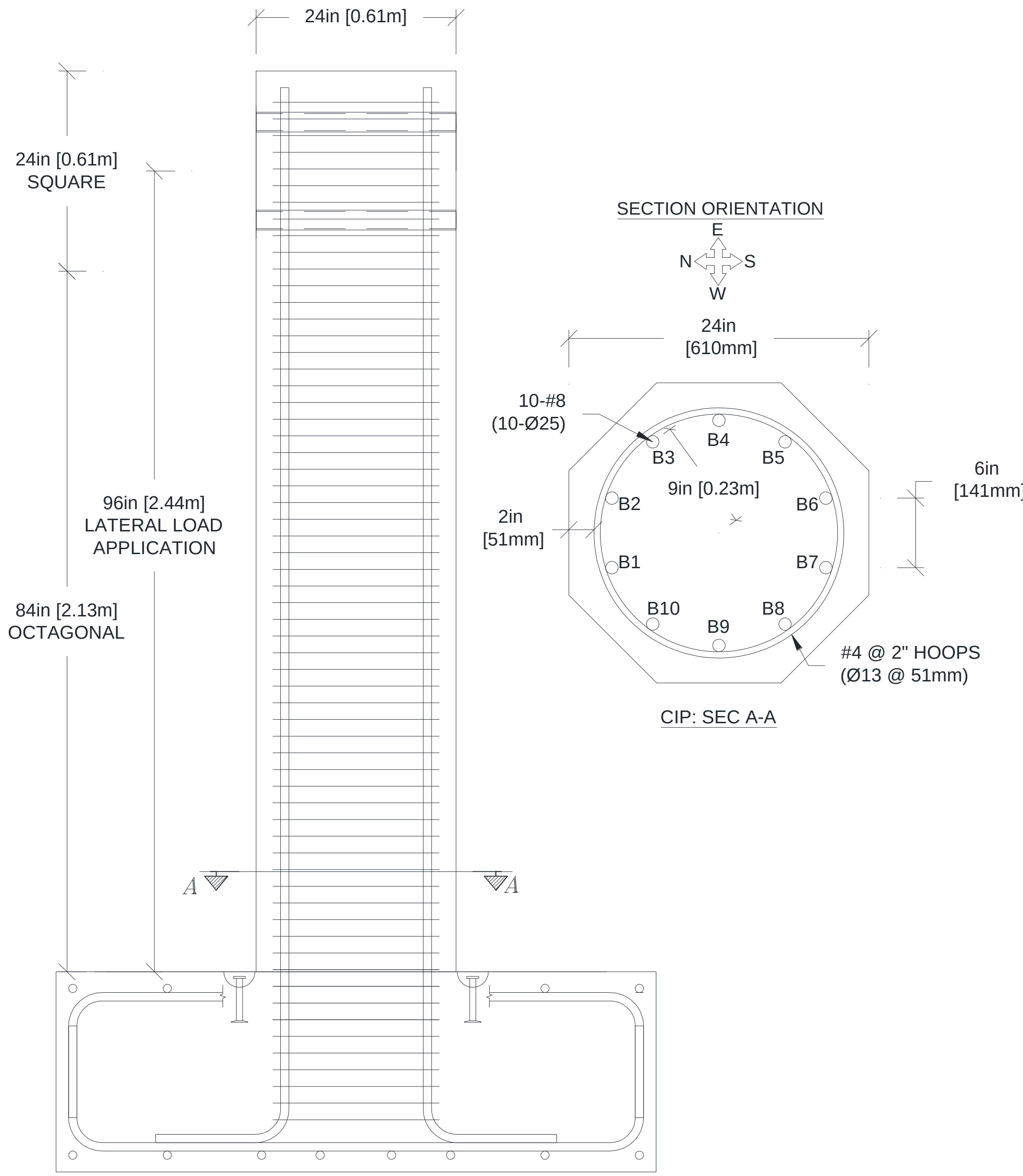

Figure 3.2. Reinforcement Detailing of CIP Column

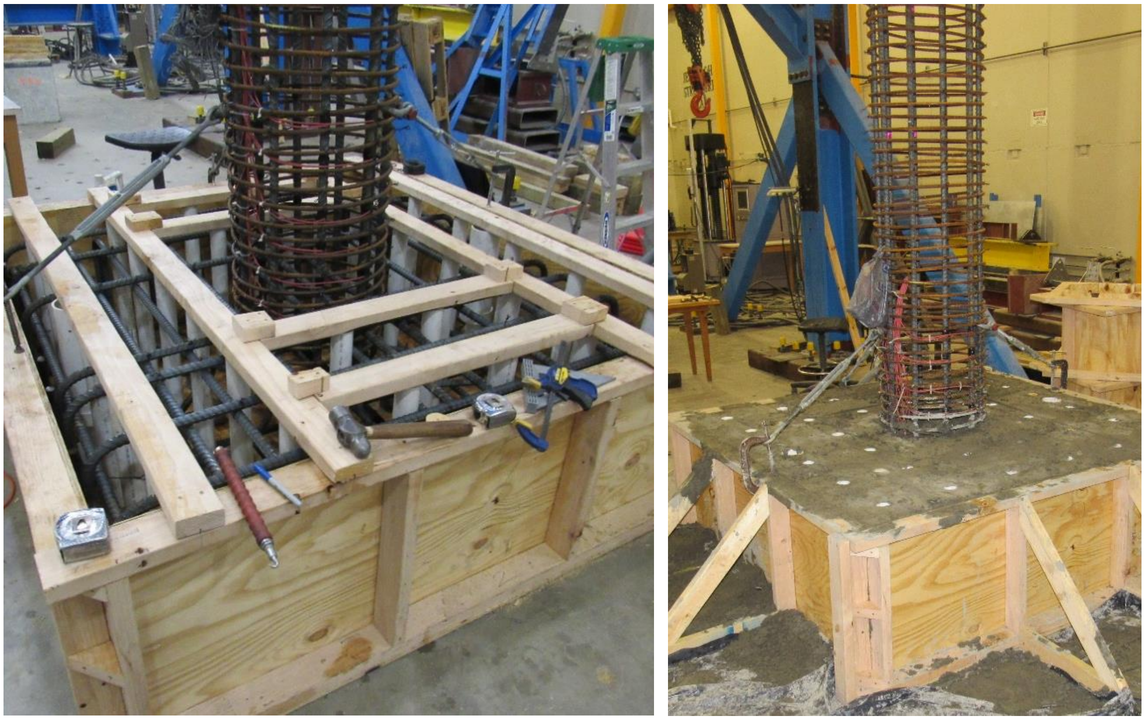

(a) Before Pour (b) After Pour

Figure 3.3. Construction of CIP Footing

(a) During Pour (b) After Pour

Figure 3.4. Construction of CIP Column

3.3.2. PGD Column Model

Following the CIP column model detailing, The PGD column model was detailed (Fig. 3.5) to incorporate the Dayton Superior “D410 Sleeve-Lock Grout Sleeve” grouted coupler. The reinforcement for this column was the same as the CIP except larger diameter hoops were used at the section with couplers. The clear cover at the section with the coupler was 1.06 in. (27 mm) and the clear cover away from the coupler was 2 in. (50.8 mm). The coupler was filled with the company specified “D490 Sleeve-Lock” grout, which can achieve a compressive strength of 12,000 psi (82.7 MPa) at 28 days when mixed at a flowable consistency.

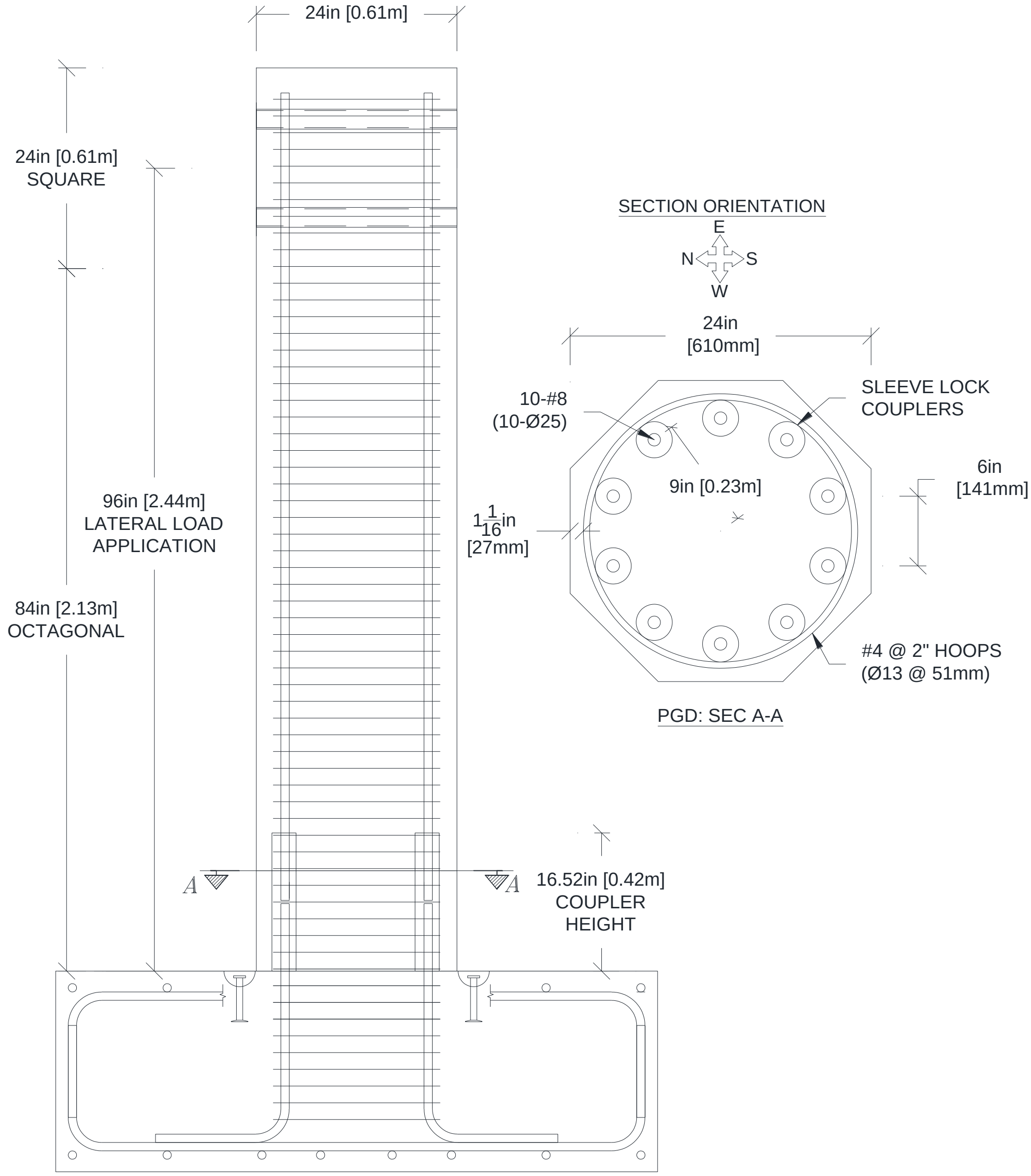

Figure 3.5. Reinforcement Detailing of PGD Column with Dayton Grouted Coupler

As mentioned earlier, all precast columns, but not the footing, were built by Gage Brothers in Sioux Falls. The construction sequence for PGD was as follows:

- Cast footing at SDSU with dowel bars extended (Fig. 3.6)
- Cast the column at precast plant with couplers embedded (Fig. 3.7)
- Erecting and installing the column at SDSU (Fig. 3.8)

- Fill the gap between the column and footing at SDSU

- Inject Sleeve-Lock grout into the couplers at SUSU (Fig. 3.9)

(a) Footing Cage (b) Concrete Pouring

Figure 3.6. Construction of PGD Footing

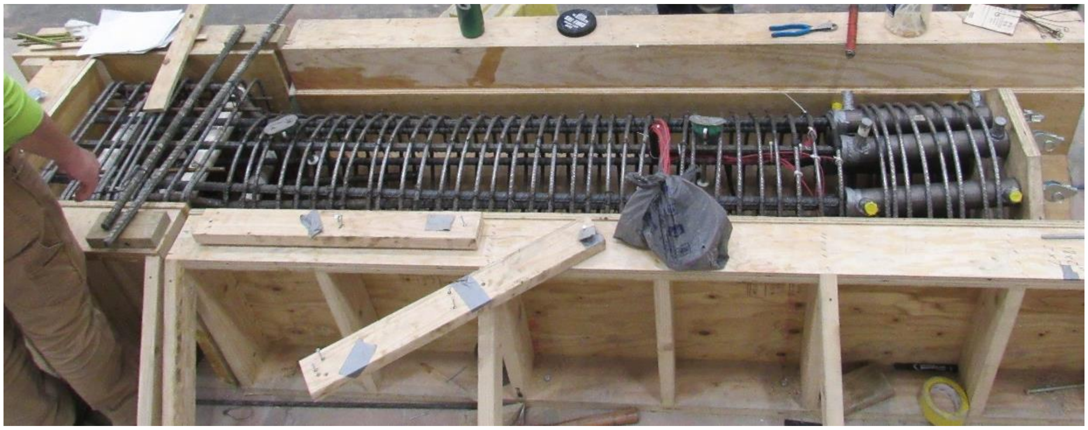

a) Column Cage

b) Column Pouring

Figure 3.7. Casting PGD Column

(a) Matching Couplers and Dowel Bars

(b) Column Secured

Figure 3.8. Erecting PGD Column

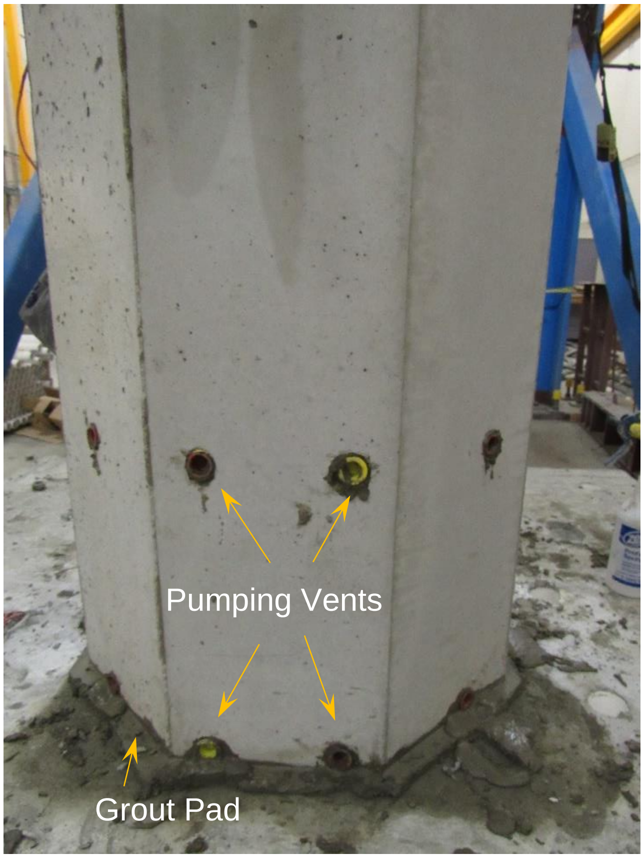

Figure 3.9. PGD Column Base After Coupler Grout Injection

Dowels extending from the footing were cut so that they protruded the coupler maximum embedment depth of 8.07 in. (205 mm). Once the column was secured, the minimal gap at the column-footing interface were filled using a high-strength, non-shrink grout (1428HP). The maximum gap observed in PGD was approximately 0.375in. (9.5 mm). Finally, the couplers were then injected with the "Sleeve-Lock" grout from bottom vents letting grout to push the air from the bottom-to-top vent, and the specimen was left undisturbed until the grout reached a sufficient strength (e.g. 7,500 psi).

3.3.3. PGS Column Model

Following the CIP column model detailing, The PGS column model was detailed (Fig. 3.10) to incorporate the NMB "Splice-Sleeve" grouted coupler. The reinforcement for this column was the same as the CIP except larger diameter hoops were used at the section with couplers. The clear cover at the section with the coupler was 1.24 in. (31 mm) and the clear cover away from the coupler was 2 in. (50.8 mm). The coupler was filled with the company specified "SS Mortar" grout; a non-shrink high-early-strength grout with a minimum 28-day compressive strength of 11000 psi (75.8 MPa).

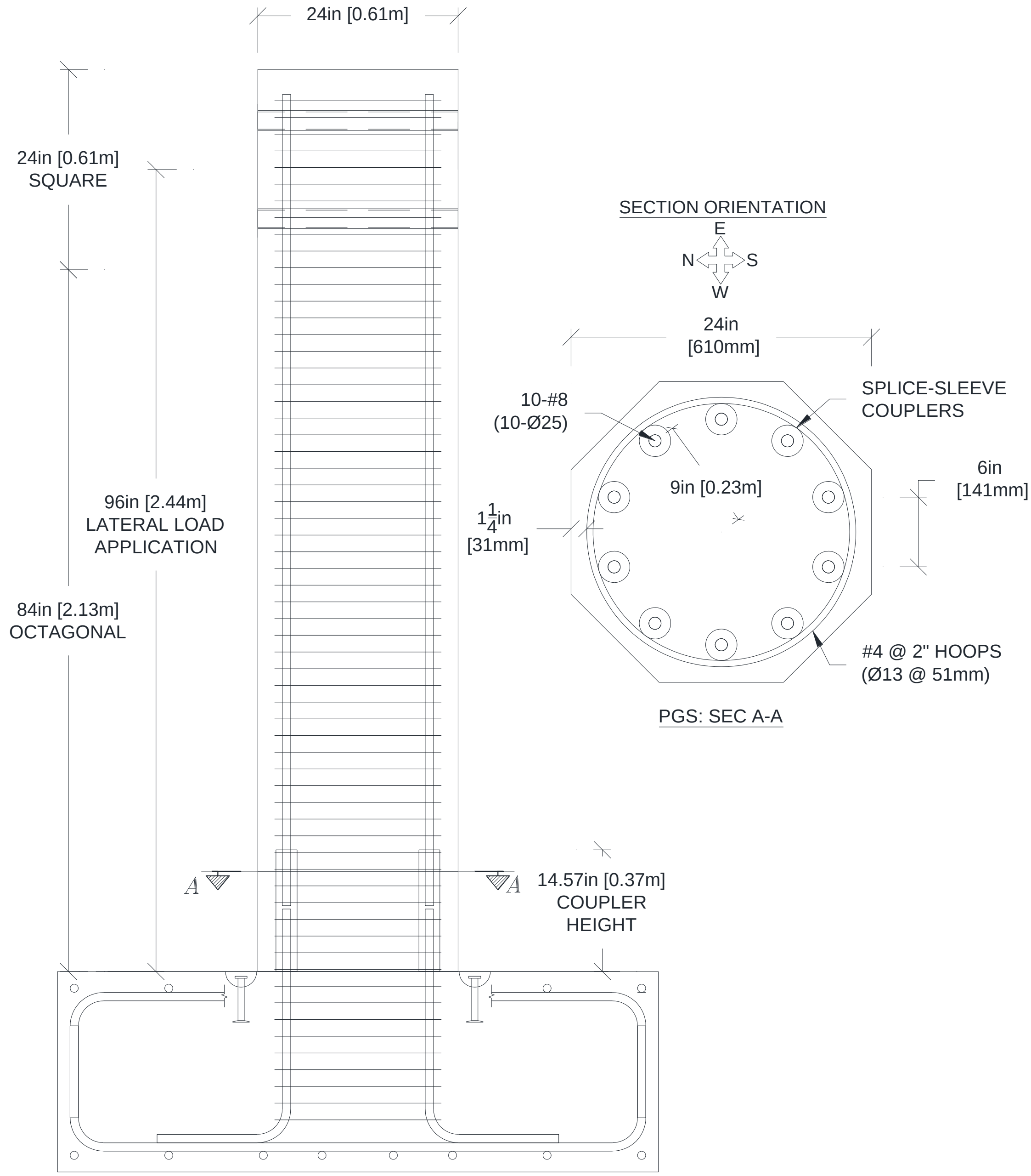

Figure 3.10. Reinforcement Detailing of PGS Column

As mentioned earlier, all precast columns, but not the footing, were built by Gage Brothers in Sioux Falls. The construction sequence for PGS was as follows:

- Cast footing at SDSU with dowel bars extended
- Cast the column at precast plant with couplers embedded (Fig. 3.11)

- Erecting and installing the column at SDSU (Fig. 3.12)

- Fill the gap between the column and footing at SDSU

- Inject Sleeve-Lock grout into the couplers at SUSU (Fig. 3.13)

a) Column Cage b) Column Pouring

Figure 3.11. Casting PGS Column

(a) (b)

Figure 3.12. Erecting PGS Column

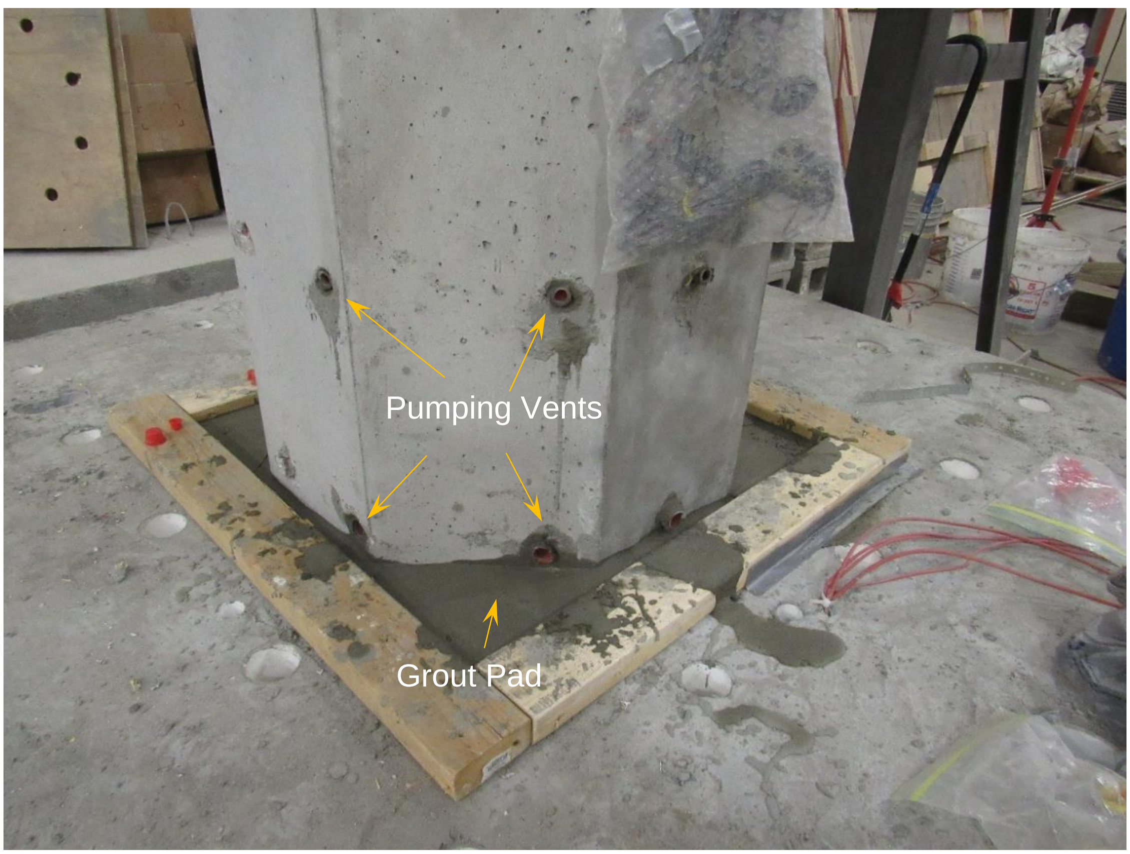

Figure 3.13. PGS Column Base After Coupler Grout Injection

Dowels extending from the footing were cut so that they protruded the coupler maximum embedment depth of 7.48 in. (190 mm). Once the column was secured, the minimal gap at the column-footing interface were filled using a high-strength, non-shrink grout (1428HP). The maximum gap observed in PGS was approximately 0.375in. (9.5 mm). Finally, the couplers were then injected with the “SS Mortar” grout from bottom vents letting grout to push the air from the bottom-to-top vent, and the specimen was left undisturbed until the grout reached a sufficient strength (e.g., 7,500 psi).

3.3.4. PHD Column Model

Following the CIP column model detailing, The PGS column model was detailed (Fig. 3.14) to incorporate the Dextra “Groutec”- threaded-grouted coupler. The reinforcement for this column was the same as the CIP except larger diameter hoops were used at the section with couplers. The clear cover at the section with the coupler was 1.42 in. (36 mm) and the clear cover away from the coupler was 2 in. (50.8 mm). The coupler was filled with the company specified “Quikrete 15800-00 Precision Grout” grout which can achieve a compressive strength of 12,500 psi (86.2 MPa) at 28 days when mixed at a flowable consistency.

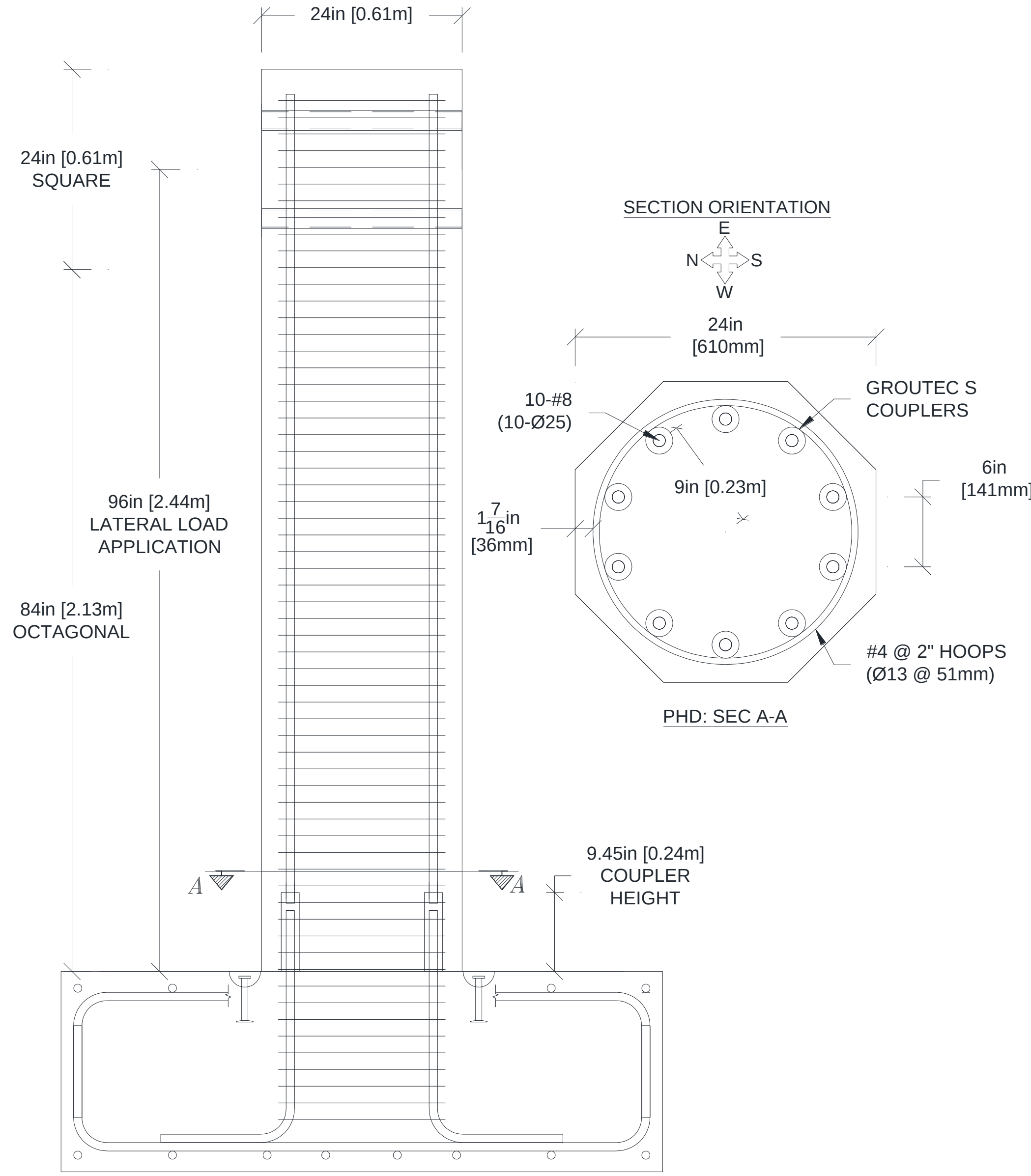

Figure 3.14. Reinforcement Detailing of PHD Column

As mentioned earlier, all precast columns, but not the footing, were built by Gage Brothers in Sioux Falls. The construction sequence for PHD was as follows:

- Cast footing at SDSU with dowel bars extended
- Cast the column at precast plant with couplers embedded (Fig. 3.15)
- Erecting and installing the column at SDSU (Fig. 3.16)

- Fill the gap between the column and footing at SDSU

- Inject Sleeve-Lock grout into the couplers at SUSU (Fig. 3.17)

a) Column Cage b) Column Pouring

Figure 3.15. Casting PHD Column

(a) (b)

Figure 3.16. Erecting PHD Column

(a) (b)

Figure 3.17. Injecting Grout into PHD Couplers

Dowels extending from the footing were cut so that they protruded the coupler maximum embedment depth of 7.87 in. (200 mm). Once the column was secured, the minimal gap at the column-footing interface were filled using a high-strength, non-shrink grout (1428HP). The maximum gap observed in PHD was approximately 0.375in. (9.5 mm). Finally, the couplers were then injected with the "Quikrete 15800-00 Precision Grout" grout from bottom vents letting grout to push the air from the bottom-to-top vent, and the specimen was left undisturbed until the grout reached a sufficient strength (e.g., 7,500 psi).

3.4 Test Setup, Instrumentation, and Loading Protocol

The test setup, instrumentation, and loading protocol were carefully designed and selected to simulate seismic loading and to collect data. This section discusses these topics in detail.

3.4.1 Test Setup

The modular lateral test setup, which was designed and constructed as part of this project, provides a cantilever configuration to laterally test a column specimen (Fig. 3.18). The actuator was mounted to a series of 3 x 5 x 8-ft (0.91 x 1.52 x 2.44-m) concrete reaction blocks that were post-tensioned to the lab strong floor. A 328-kip (1460-kN) hydraulic actuator was used to apply lateral loads at the column head. The column axial load was applied to using a self-reacting system with two hollow core jacks installed on a spreader beam perpendicular to the loading direction with high-strength threaded rods transferring the load from the jacks to the column footing.

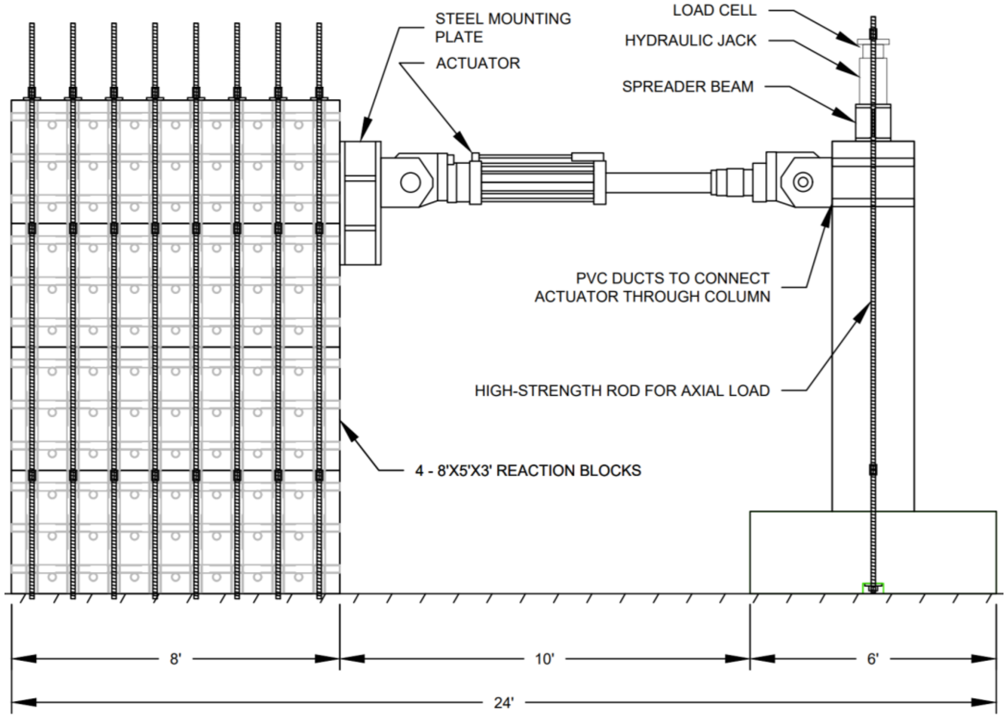

(a) Column Test Setup Elevation View

(b) Photograph of Column Test Setup

Figure 3.18. Column Test Setup

3.4.2 Instrumentation

Local and global responses were measured using a multitude of instruments. Reinforcement strain was measured by strain gages installed at different levels. Figure 3.19 shows the typical strain gage sections, elevation, and numbering. Strain gages were not placed in the sections where a coupler was present. Table 3.2 shows strain gage schedule for the column models. Rotation and curvature were measured within the plastic hinge of the columns using LVDTs placed on opposite faces of the column in the direction of loading at different levels (Fig. 3.20). The lateral displacement of the column tip and its rotations were measured using three string potentiometers as shown in Fig. 3.20. The lateral load on the column was measured using the actuator load-cell. Furthermore, two 100-kip (445 kN) load cells were placed above the hollow core jacks, one per jack, to measure the column axial loads during testing. In all tests, the target axial load was 155 kip (689 kN), which was slightly different in different columns and was adjusted during testing to achieve the target load at large displacements. Note that the applied axial load was equivalent to approximately 5% axial load index for a design concrete strength of 6000 psi (41.4 MPa). However, the index varied based on the actual concrete strength at the column test day. A 128-channel data acquisition system was used to record data with a sampling rate of 10 Hz.

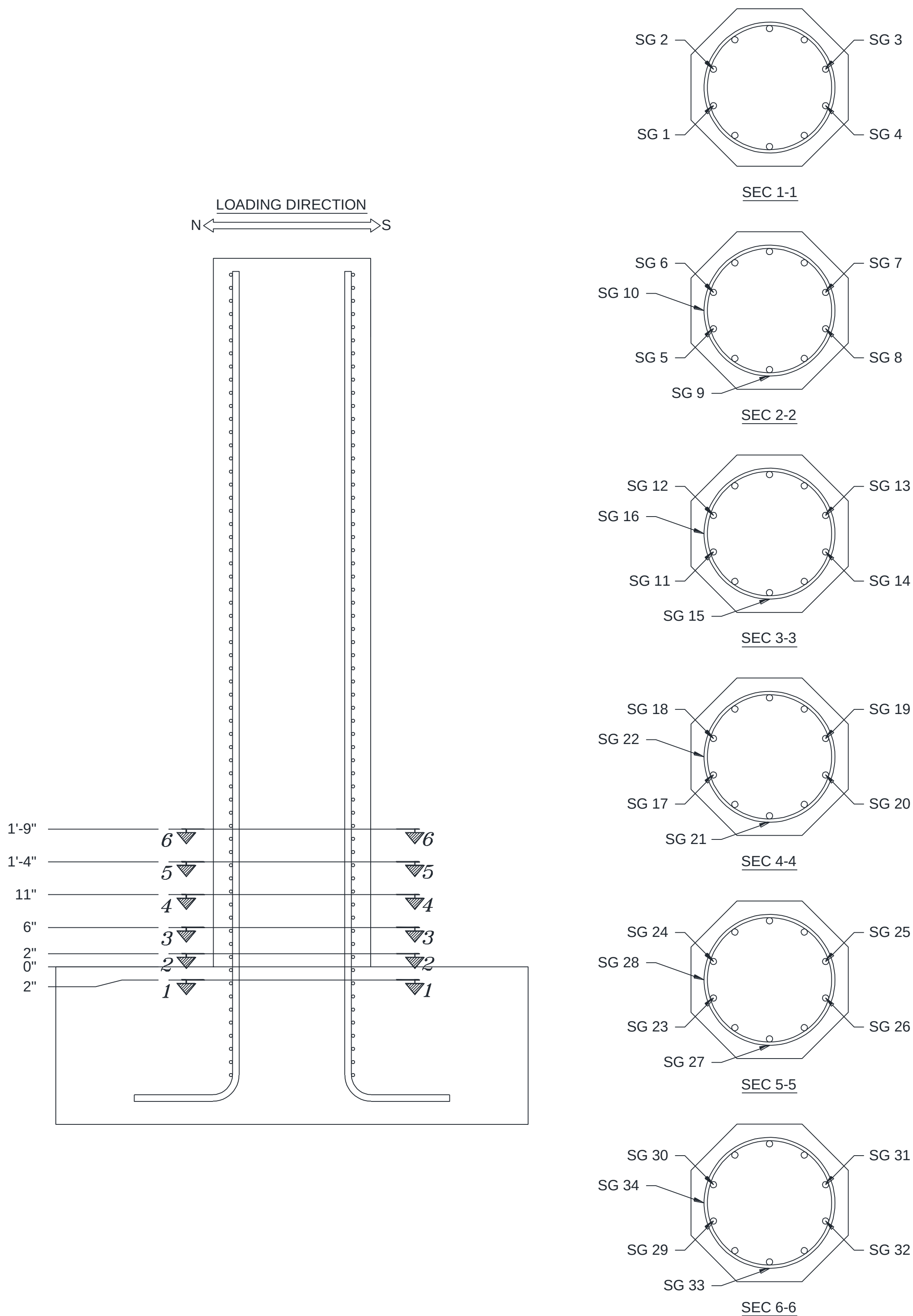

Figure 3.19. Typical Strain Gage Sections and Elevations Used in Column Models

Table 3.2. Column Model Strain Gage Placement Schedule

Column	Sections Where Strain Gages Were Placed					
	SEC 1-1	SEC 2-2	SEC 3-3	SEC 4-4	SEC 5-5	SEC 6-6
CIP	X	X	X	X	X	X
PGD	X	No SG	No SG	No SG	X	X
PGS	X	No SG	No SG	No SG	X	X
PHD	X	No SG	No SG	X	X	X

Note: "X" indicates that strain gauges were placed in column cross sections shown in Fig. 3.19

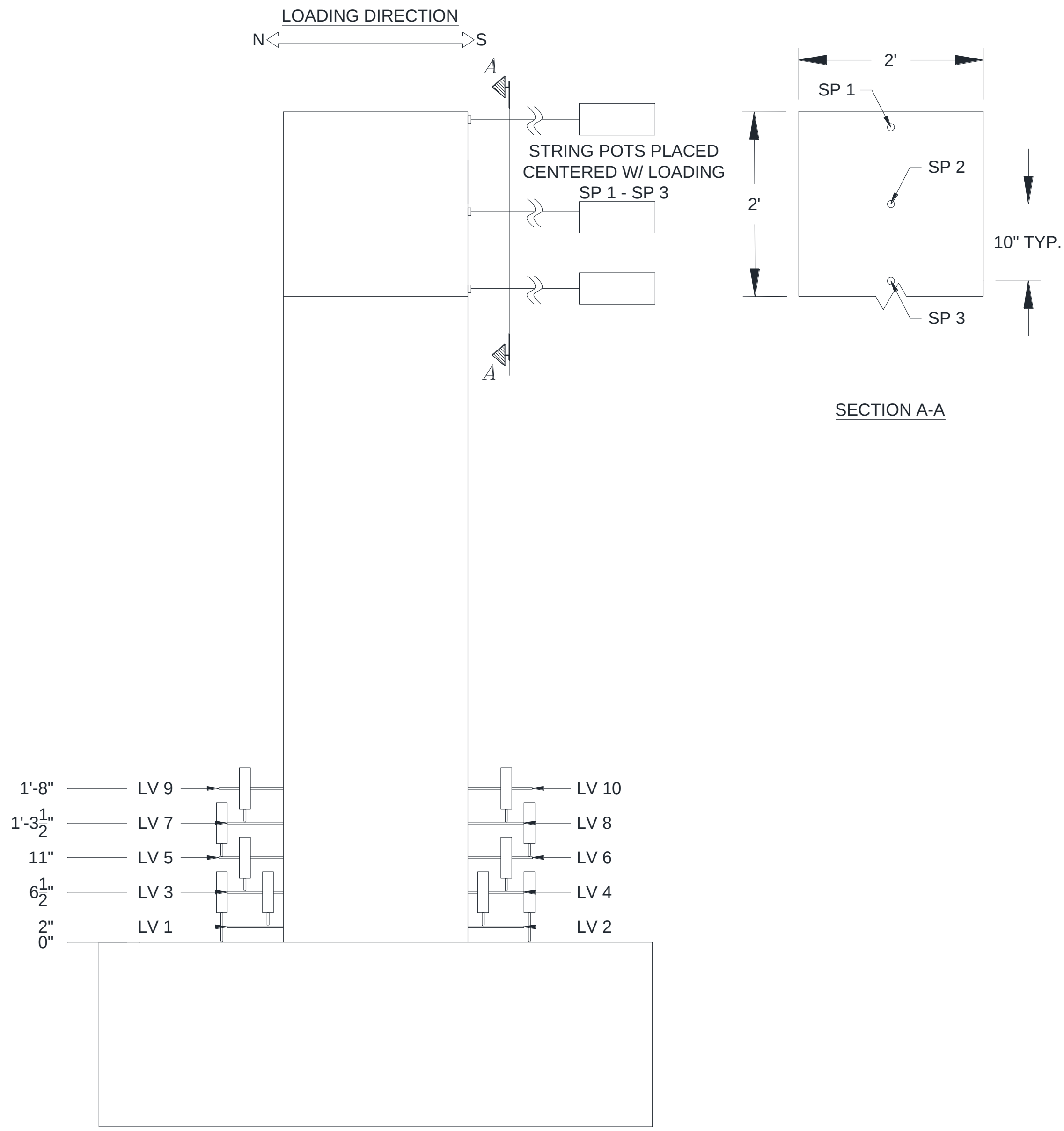

Figure 3.20. Typical LVDT & String Potentiometer Locations Used in Column Models

3.4.3 Loading Protocol

The column models were tested using a slow lateral cyclic drift-based loading following ACI 374.2R-13 (2013). Drift ratio is the ratio of column lateral displacement to the height of the column. Figure 3.21 shows the loading protocol for each test. Two full cycles were completed at each drift level. A displacement rate of 3.0 in./min was used for drift ratios from 0.25% to 2% to capture the yield point. A faster displacement rate of 30 in./min was used for drift ratios including 3% to failure. The displacement rates estimated based on ASTM E8 strain rate limits for rebar testing.

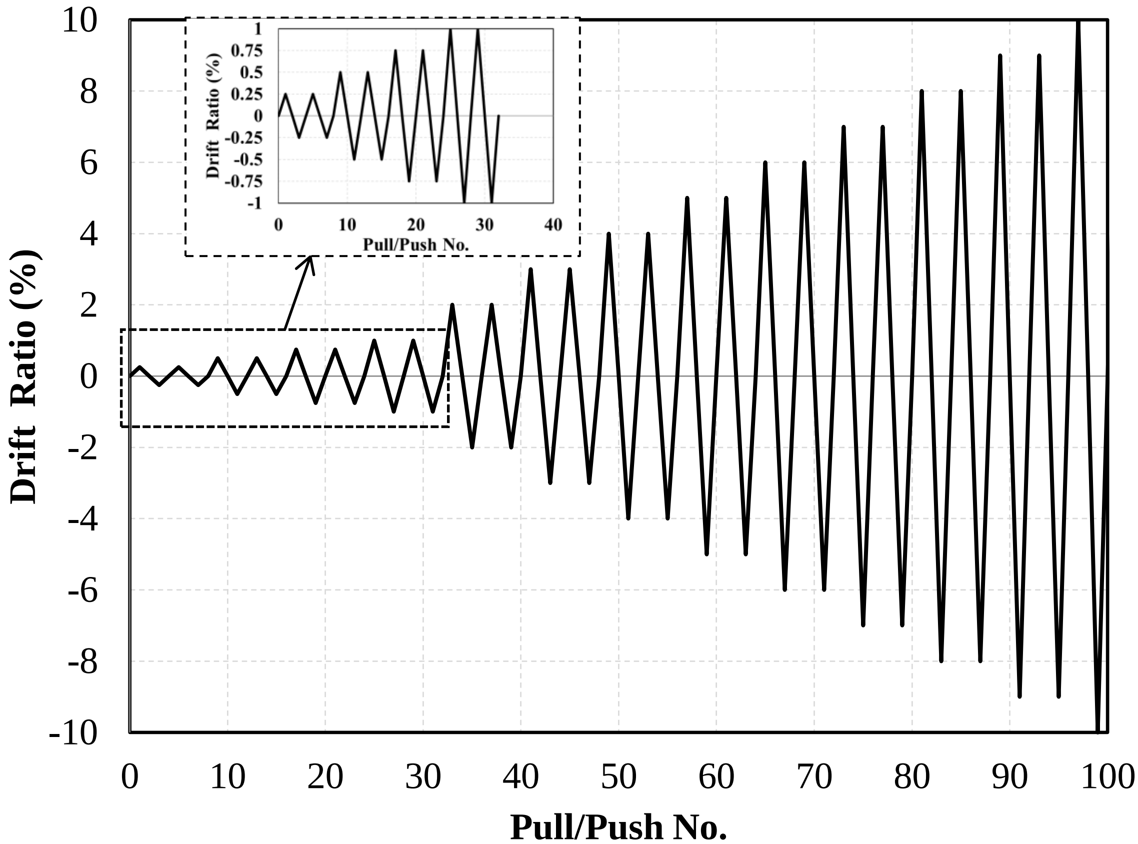

Figure 3.21. Typical Loading Protocol Used for Column Testing

3.5 Test Results

Testing of one cast in place reference column and three precast columns was conducted in the Lohr Structures laboratory at South Dakota State University. Each of the precast columns used a different model of mechanical bar splice embedded at the base of the column. Columns were tested using displacement controlled slow cyclic loading. The constituent materials of each column model were also tested to determine material properties for accurate modeling. The results of material testing and column testing are presented in this section.

3.5.1 Material Properties

Several materials were used in the construction of the columns including conventional concrete, self-consolidating concrete (SCC), different non-shrink grout types, reinforcing steel bars, and three products of mechanical bar splices. The measured properties of each material are presented herein, following standard ASTM procedures where applicable.

3.5.1.1 Conventional Concrete

Conventional concrete was used in the footing for all models and in the CIP column. The concrete compressive strength testing was conducted according to ASTM C39/C39M. Standard concrete samples with a diameter of 6-in. (152-mm) and a height of 12-in. (305-mm) were used. Table 3.3 presents the measured compressive strength of cementitious materials used in each column model. The average concrete compressive strength of three samples was reported in the table at 7-day, 28-day, and the test day of each column model.

3.5.1.2 SCC

All precast columns were made with SCC. The sample sizes and testing procedure were the same as conventional concrete. The SCC measured compressive strength at 7-day, 28-day, and column test day is reported in Table 3.3.

3.5.1.3 Non-Shrink Grout

Non-shrink grout was injected into the coupler for each precast column per the coupler manufacturer's requirements. "D410 Sleeve Lock", "SS Mortar", and "Quikrete 1580-00" grouts were used for the PGD, PGS, and PHD column models, respectively. Two-inch (51-mm) cube sampled collected according to ASTM C109/C109M and the cube samples were tested according to ASTCM C109/C109M. Table 3.3 presents the measured grout compressive strength at 7-day and the column test day. Note may more samples were tested prior to the column testing to decide when to test the column, but those are not reported herein.

Table 3.3. Measured Compressive Strength of Cementitious Materials Used in Column Models

			Column Models, psi (MPa)			
Material	Element	Measured at	CIP	PGD	PGS	PHD
Conventional and SCC Concrete*	Footing	7-Day	3670 (25.3)	4365 (30.1)	3275 (22.6)	5435 (37.5)
		28-Day	4620 (31.9)	N/A	3900 (26.9)	6335 (43.7)
		Col. Test Day	4920 (33.9)	4830 (33.3)	3980 (27.4)	6770 (46.7)
	Column	7-Day	3360 (23.2)	6980 (48.1)	7890 (54.4)	8380 (57.8)
		28-Day	4010 (27.6)	7950 (54.8)	8880 (61.2)	8875 (61.2)
		Col. Test Day	4300 (29.6)	7950 (54.8)	8590 (59.2)	9640 (66.5)
Grout	Coupler	7-Day	N/A	11160 (76.9)	13130 (90.5)	7140 (49.2)
		28-Day	N/A	N/A	N/A	N/A
		Col. Test Day	N/A	12680 (87.4)	14680 (101.2)	15480 (106.7)

* Conventional concrete was used in the CIP column and all footings. SCC was used in the precast columns. "D410 Sleeve Lock", "SS Mortar", and "Quikrete 1580-00" grouts were used for the PGD, PGS, and PHD column models, respectively.

3.5.1.4 Reinforcing Steel

All reinforcing steel used in this project conformed to ASTM A706 Grade 60. The columns were longitudinally reinforced with #8 (Ø25 mm) bars and transversely reinforced with #4 (Ø13 mm) hoops. All longitudinal bars used in this project were from the same heat number (batch) and therefore they had the same properties. This was done to minimize the column response variations. The transverse reinforcement used in the CIP model was from one heat number, while all transverse reinforcement used in the precast models came from another separate heat number. Tensile testing of all rebars was conducted according to ASTM E8. Table 3.4 presents the measured average tensile properties of the samples tested. A sample of the longitudinal bar stress-strain behavior is presented in the following section with the coupler data.

Table 3.4. Measured Strength of Reinforcing Steel Used in Column Models

Bar	Column Model	Bar Size	ASTM Type	Yield Strength, f_y ksi (MPa)	Ultimate Strength, f_u ksi (MPa)	Post-Yield Stiffness, E_{sh} ksi (MPa)	Ultimate Stain, ε_u (%)*
Longitudinal	All Models	#8 (Ø25)	A706 Gr. 60	69.3 (478)	97.4 (672)	853 (5880)	12.0
Hoops	CIP	#4 (Ø13)	A706 Gr. 60	66.6 (459)	102.1 (704)	1873 (12910)	9.9
	Precast	#4 (Ø13)	A706 Gr. 60	65.3 (450)	100.7 (694)	2567 (17700)	9.8

* Strain at the peak stress

3.5.1.5 Couplers

Monotonic tensile loading was conducted on five samples of each of the coupler types used in the precast column models. The test protocol followed the recommendations by Dahal and Tazarv (2020). The displacement-based loading was conducted at a rate of 0.021 in/in/min. Figure 3.22 shows the mechanical bar splice testing setup, and Fig. 3.23 shows the coupler sample geometry convention used. The

total specimen length (L_{tot}) depends on bar diameter and the physical length of the splice (L_{sp}). The coupler region length (L_{cr}) is the coupler length plus α (Alpha) times the bar diameter ($\alpha.d_b$) from each end of the coupler. An Alpha of 1.25 in. (31.8 mm) was used for all coupler samples tested in this study. The length of bar outside of the coupler was always at least 6 in. (152.4 mm) to avoid stress concentration.

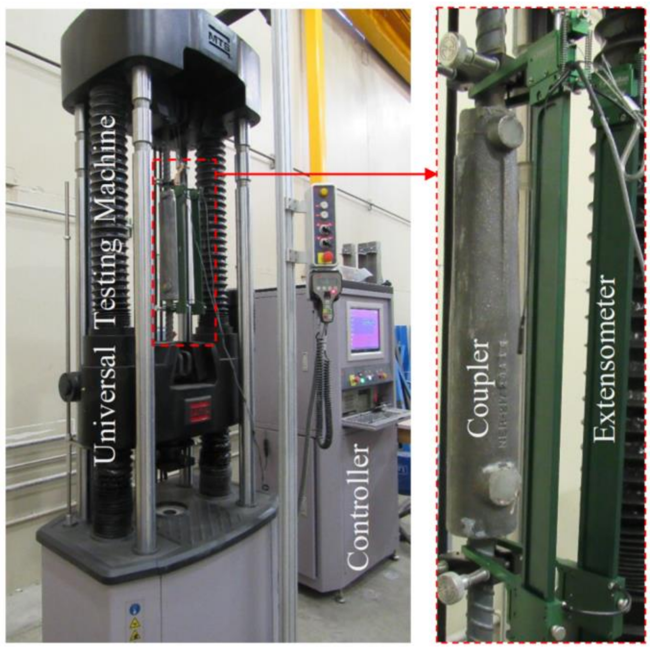

Figure 3.22. Test Setup for Mechanical Bar Splices

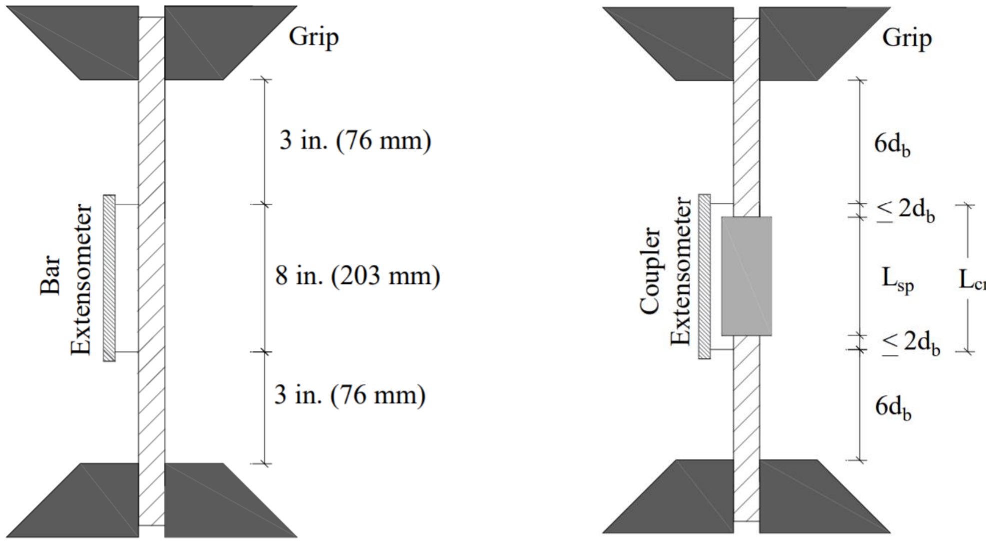

a) Unspliced Specimen b) Spliced Specimen

Figure 3.23. Geometry of Tensile Testing on Bar and Coupler Specimens

Figure 3.24 shows the tensile test results for the No. 8 (25-mm) Dayton Superior Sleeve-Lock coupler. The couplers -respectively showed a reduction in the ultimate strain compared with the reference bar of 63%, 56%, 58%, 63%, and 64% in Runs 1 through 5. The average reduction in the ultimate strain compared with the unspliced reference bar was 61%. Out of five samples, bar fractured in four couplers and a bar pulled out from one sample (the first sample tested that had the lowest grout strength) at 4.4% strain. Overall, this coupler was rated as a “seismic coupler”.

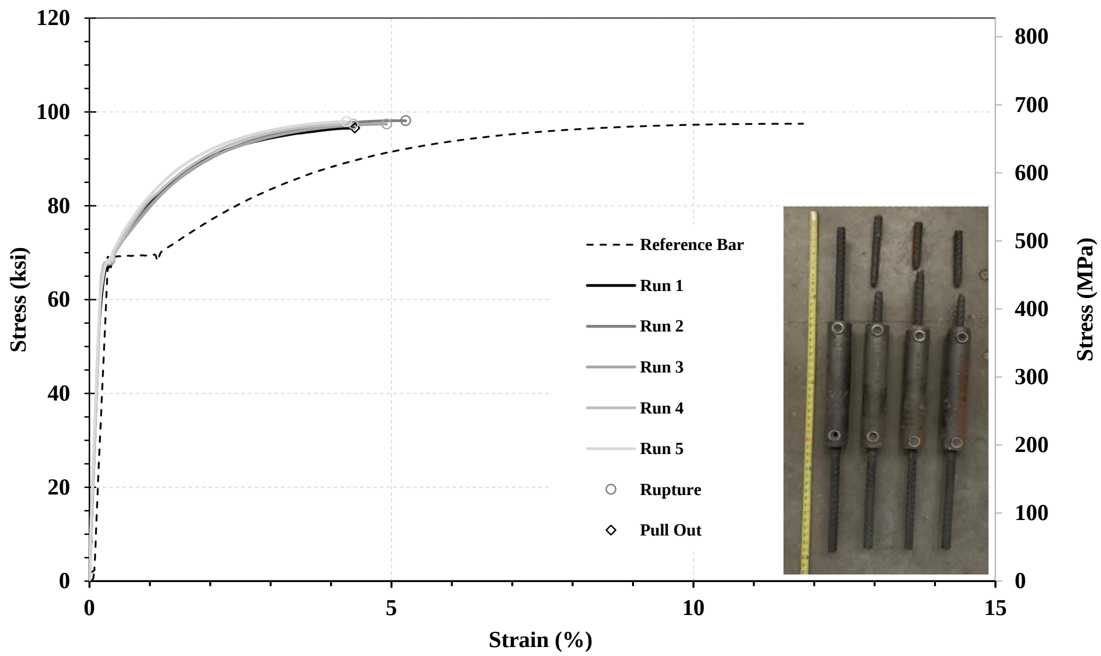

Figure 3.24. Tensile Test Results for No. 8 (25-mm) Dayton Superior Sleeve-Lock Couplers

Figure 3.25 shows the tensile test results for the No. 8 (25-mm) NMB Splice Sleeve coupler. Bar fractured in all five specimens, and the reduction in the ultimate strain compared with the reference bar was respectively 58%, 61%, 60%, 60%, and 65% for Runs 1 through 5. The average reduction in strain compared to the unspliced reference bar was 61%. Overall, this coupler was rated as a “seismic coupler”.

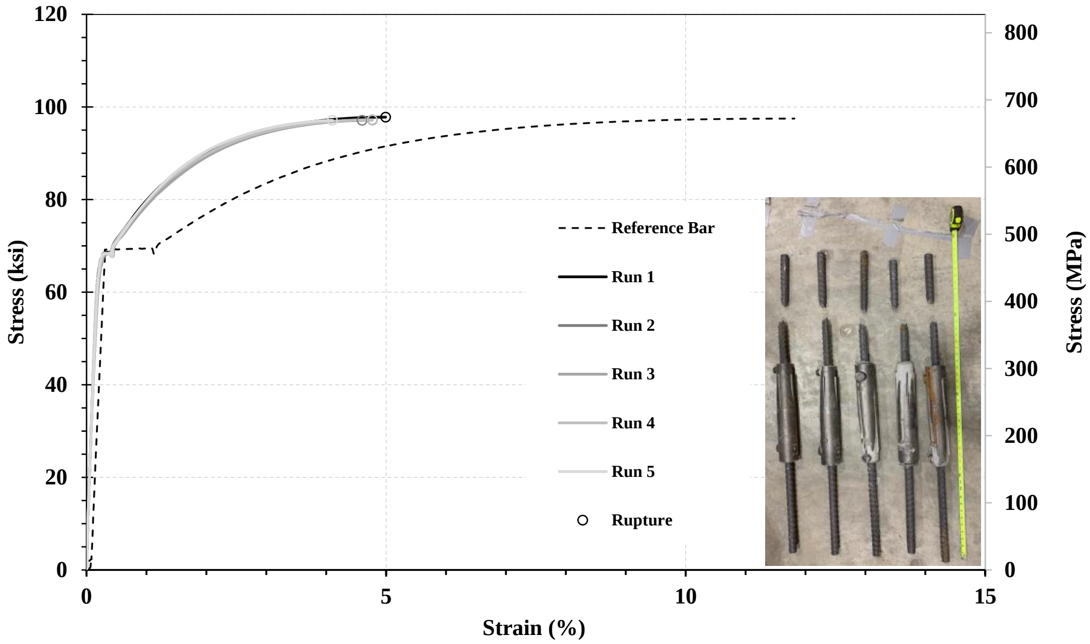

Figure 3.25. Tensile Test Results for No. 8 (25-mm) NMB Splice Sleeve Couplers

Figure 3.26 shows the tensile test results for the No. 8 (25-mm) Dextra Groutec S couplers. The couplers showed a reduction in the ultimate strain compared with the reference bar of 80%, 75%, 47%, 38%, and 74% respectively for Runs 1 through 5. The average reduction in strain compared with the unspliced reference bar was 63%. Bar pulled out from four couplers and bar fractured in one specimen but inside the coupler. Overall, this coupler type is not “a seismic coupler” and should not be used in a bridge column with this performance. It should be noted that the failure mode observed in our testing was not consistent with the previous coupler testing reported by the manufacturer. After communicating the issue with the manufacturer, the reason for bar pullout could not be determined. The actual grout strength in our tests were higher than the required strength. The research team recommends that the manufacturer provides a specific grout type for field use not commercial off-the-self products, which was used in this project per

their recommendations. In summary, a better grout product that is compatible with this coupler should be specified/provided by the manufacturer.

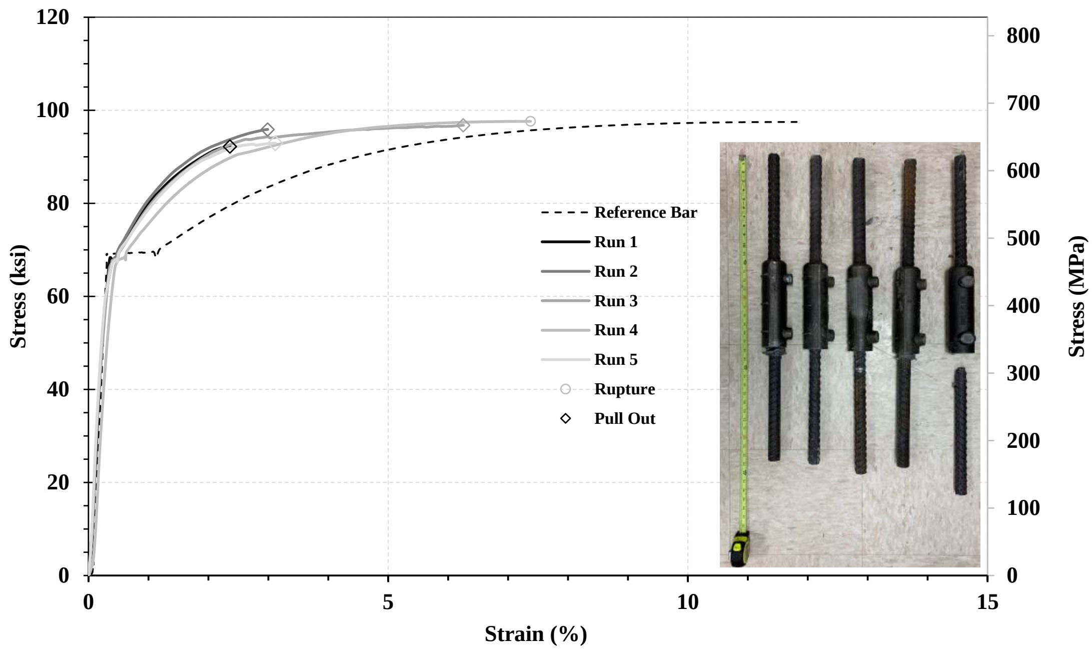

Figure 3.26. Tensile Test Results for No. 8 (25-mm) Dextra Groutec S Couplers

The coupler rigid length factor based on the coupler ultimate strain (β_u) was calculated for each coupler following to the method discussed in Dahal and Tazarv (2020). Table 3.5 presents the measured coupler rigid length factors for the spliced used in the columns. The average rigid length factor of the Dayton Superior Sleeve-Lock, NMB Splice Sleeve, and Dextra Groutec S couplers was 0.70, 0.70, and 0.79, respectively. Note that the coupler rigid length factor should only be reported for the seismic couplers. However, Beta for all tests were reported for completeness and use in future studies.

Table 3.5. Measured Coupler Rigid Length Factors

No. 8 (25-mm) Bar	Sample	L_{sp}	α	L_{cr}	Model of Failure	Coupler Strain Capacity, ε_u	β_u
Dayton Superior Sleeve-Lock	1	16.50	1.25	19.00	Bar Pullout	4.39	0.72
	2				Bar Fracture	5.24	0.64
	3				Bar Fracture	4.92	0.67
	4				Bar Fracture	4.37	0.73
	5				Bar Fracture	4.26	0.74
	Average					4.63	0.70
NMB Splice Sleeve	1	14.57	1.25	17.07	Bar Fracture	5.00	0.68
	2				Bar Fracture	4.60	0.72
	3				Bar Fracture	4.77	0.70
	4				Bar Fracture	4.77	0.70
	5				Bar Fracture	4.11	0.76
	Average					4.65	0.70
Dextra Groutec S	1	9.45	1.25	11.95	Bar Pullout	2.36	1.01
	2				Bar Pullout	2.99	0.95
	3				Bar Pullout	6.26	0.60
	4				Bar Fracture	7.37	0.48
	5				Bar Pullout	3.12	0.93
	Average					4.42	0.79

Beta should be calculated only for the seismic couplers. However, they are reported herein to be used in analytical studies.

3.5.2 CIP Column Results

The CIP column is a cast in place column that serves a reference for the rest of the columns tested. The column was tested using the slow reversed cyclic loading protocol presented in Sec. 34. The performance of the CIP column is discussed in this section.

3.5.2.1 Observed Damage

The CIP cross-section orientation and the numbering of the column longitudinal bars were shown in Fig. 3.2. The column was loaded in the North-South direction. The load was defined as pushing when the column was displaced from North to South and pulling was defined in the opposite direction (Fig. 3.18). Table 3.6 presents a summary

of the damage observed for each push or pull load for the CIP column. Figures 3.27 to 3.52 show the CIP plastic hinge damage in the second cycle at different drift levels.

Flexural cracks were occurred in the first cycle of 0.25% drift ratio. Shear cracks were first observed in the first cycle of 0.5% drift ratio (Fig. 3.29 & 3.30). The first tensile yielding occurred in Bar B7 (Fig. 3.2) at 0.47% drift ratio in the first push run of the 0.75% drift cycle under a lateral load of 37.53 kips (166.9 kN) (Fig. 3.31). Concrete spalling began to occur on both the North and South faces of the column during the 2% drift cycle (Fig. 3.35 & 3.36). Bars B1 and B2 were exposed during the 7% drift cycle (Fig. 3.45 & 3.46). During the first 9% drift cycle, Bars B6 and B7 were exposed and Bar B2 buckled. Bars B6 and B7 buckled during the second 9% drift cycle (Fig. 3.49 & 3.50). Finally, Bar B2 ruptured during the first 10% drift cycle leading to a major strength reduction and the ending the test (Fig. 3.51 & 3.52).

The CIP Column mode of failure was the longitudinal bar buckling followed by bar fracture above the column-footing interface during 10% drift cycles.

Table 3.6. Summary of Damage in CIP

Drift Ratio, %	Observed Damage
+0.25	• Minor flexural cracks
-0.25	• Minor flexural cracks
+0.50	• Flexural and inclined cracks
-0.50	• Flexural and inclined cracks • Cracking at column base
+0.75	• Flexural Cracks • Bar Yielding
-0.75	• Flexural Cracks • Bar Yielding
+1.00	• Vertical, flexural, and inclined cracks
-1.00	• Vertical, flexural, and inclined cracks
+2.00	• Vertical, flexural, and inclined cracks • Initiation of spalling on South face of column
-2.00	• Vertical, flexural, and inclined cracks • Initiation of spalling on North face of column
+3.00	• Widening of cracks
-3.00	• Widening of cracks
+4.00	• Extensive concrete spalling
-4.00	• Extensive concrete spalling
+5.00	• Widening of cracks
-5.00	• Transverse bars exposed on South face of column
+6.00	• Transverse bars exposed on North face of column
-6.00	• Several transverse bars exposed on South face of column
+7.00	• Several transverse bars exposed on North face of column • Longitudinal bar exposed on North face of column
-7.00	• Longitudinal bar exposed on South face of column
+8.00	• No further damage
-8.00	• No further damage
+9.00	• Longitudinal bar buckled on South face of column
-9.00	• Longitudinal bar buckled on North face of column
+10.00	• Longitudinal bar rupture on North face of column
-10.00	• No further damage

Note: Positive drifts were based on displacements away from the reaction blocks (North to South)

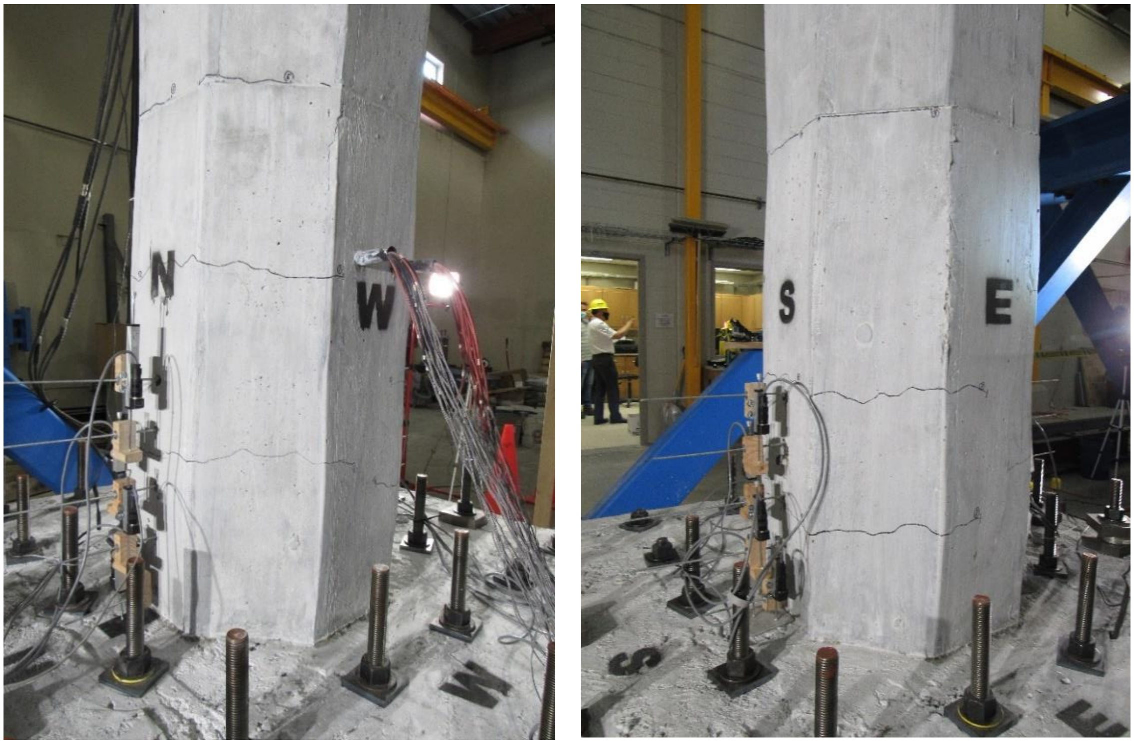

a) North-West Side b) South-East Side

Figure 3.27. CIP Column Plastic Hinge Damage, Second Push of 0.25% Drift Cycle

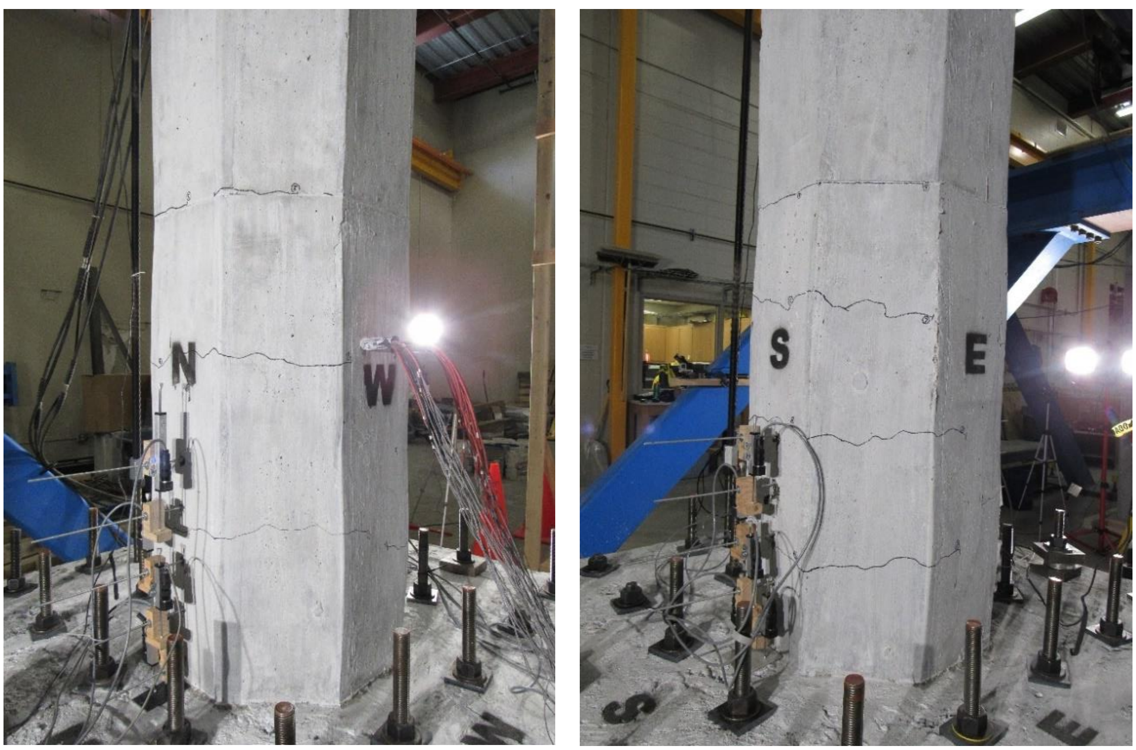

a) North-West Side b) South-East Side

Figure 3.28. CIP Column Plastic Hinge Damage, Second Pull of 0.25% Drift Cycle

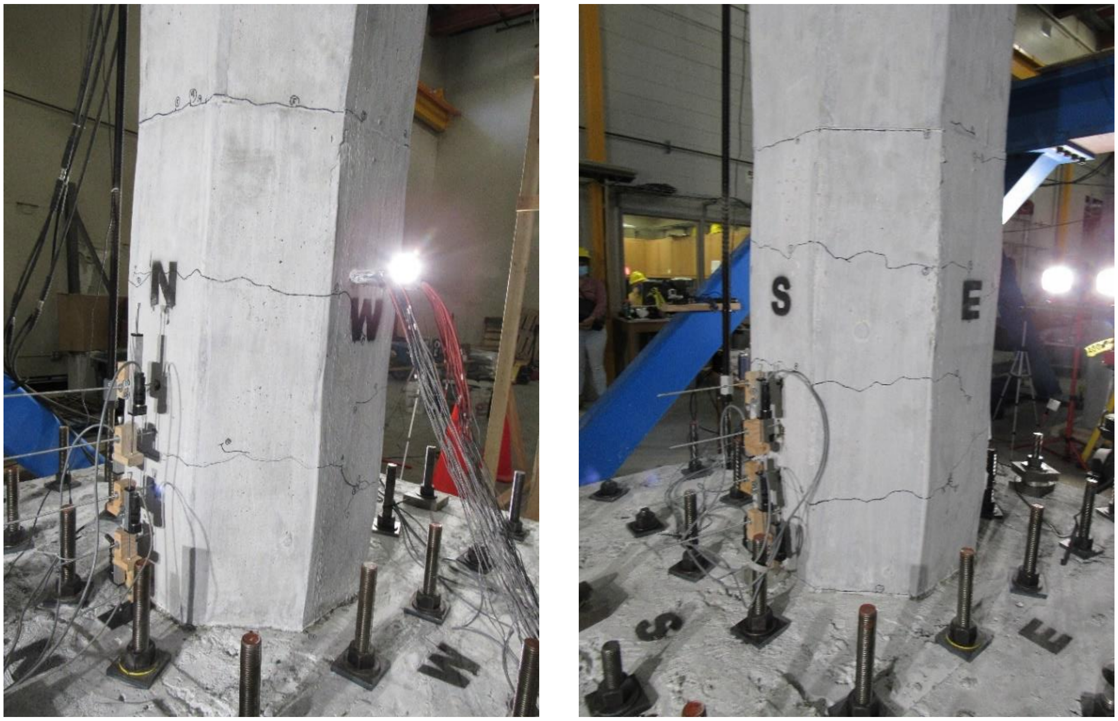

a) North-West Side b) South-East Side

Figure 3.29. CIP Column Plastic Hinge Damage, Second Push of 0.5% Drift Cycle

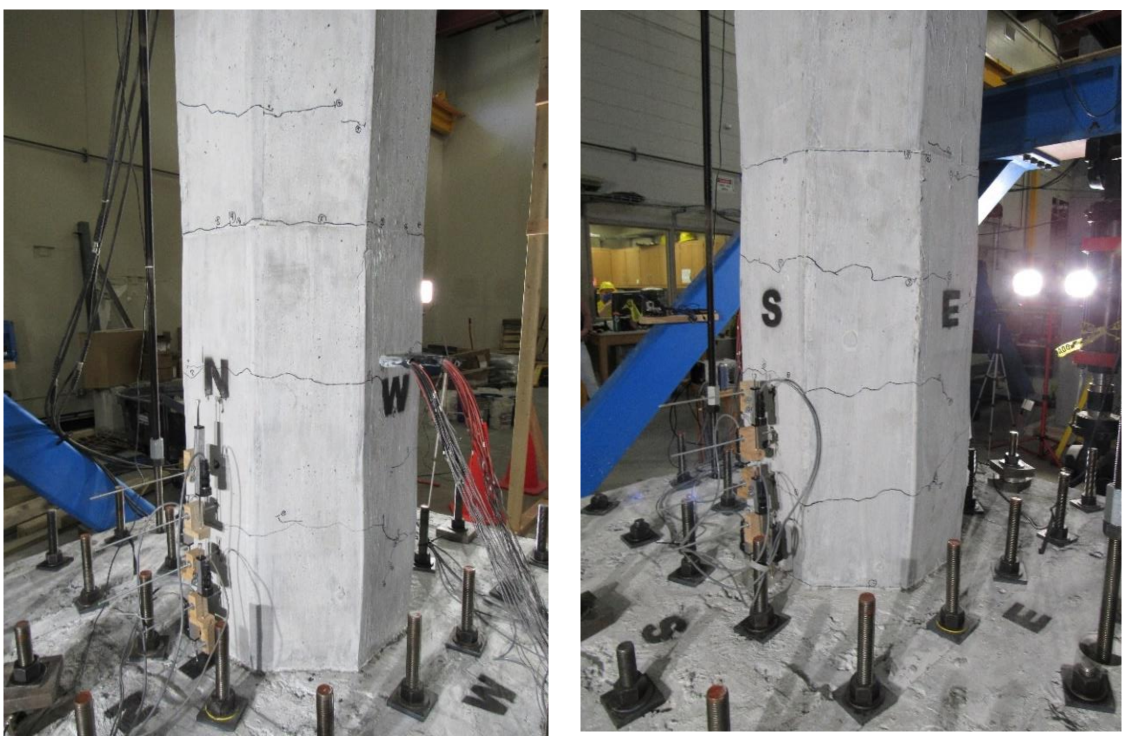

a) North-West Side b) South-East Side

Figure 3.30. CIP Column Plastic Hinge Damage, Second Pull of 0.5% Drift Cycle

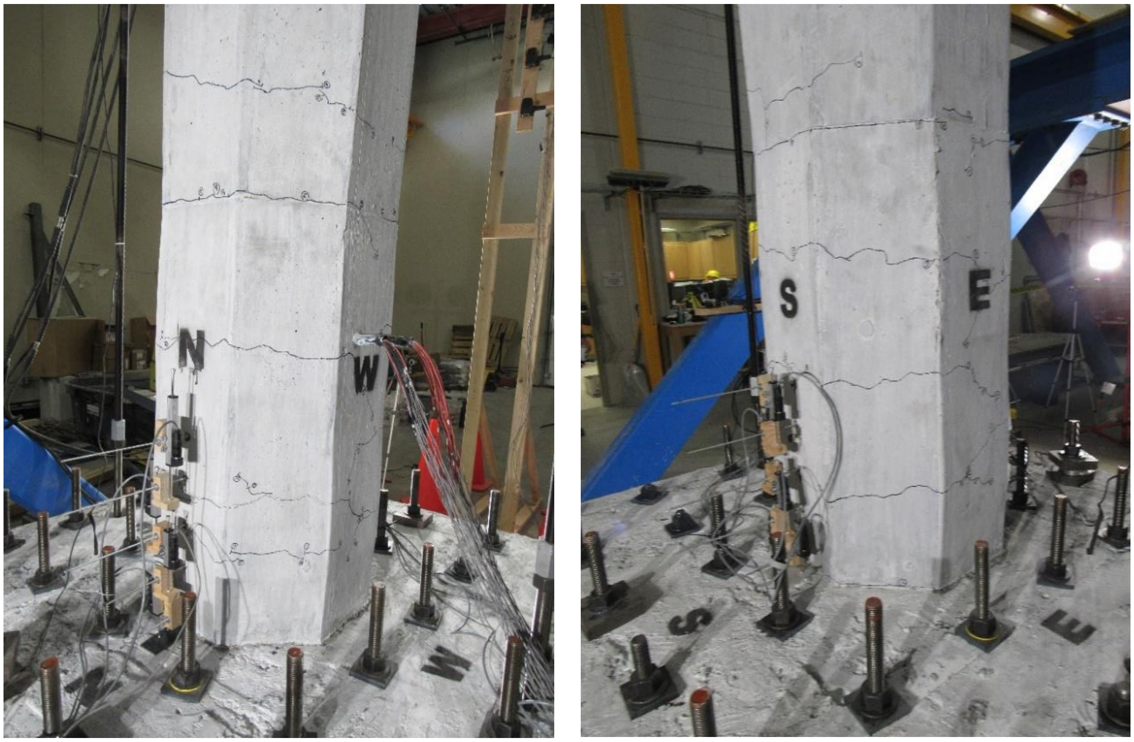

a) North-West Side b) South-East Side

Figure 3.31. CIP Column Plastic Hinge Damage, Second Push of 0.75% Drift Cycle

a) North-West Side b) South-East Side

Figure 3.32. CIP Column Plastic Hinge Damage, Second Pull of 0.75% Drift Cycle

a) North-West Side b) South-East Side

Figure 3.33. CIP Column Plastic Hinge Damage, Second Push of 1.00% Drift Cycle

a) North-West Side b) South-East Side

Figure 3.34. CIP Column Plastic Hinge Damage, Second Pull of 1.00% Drift Cycle

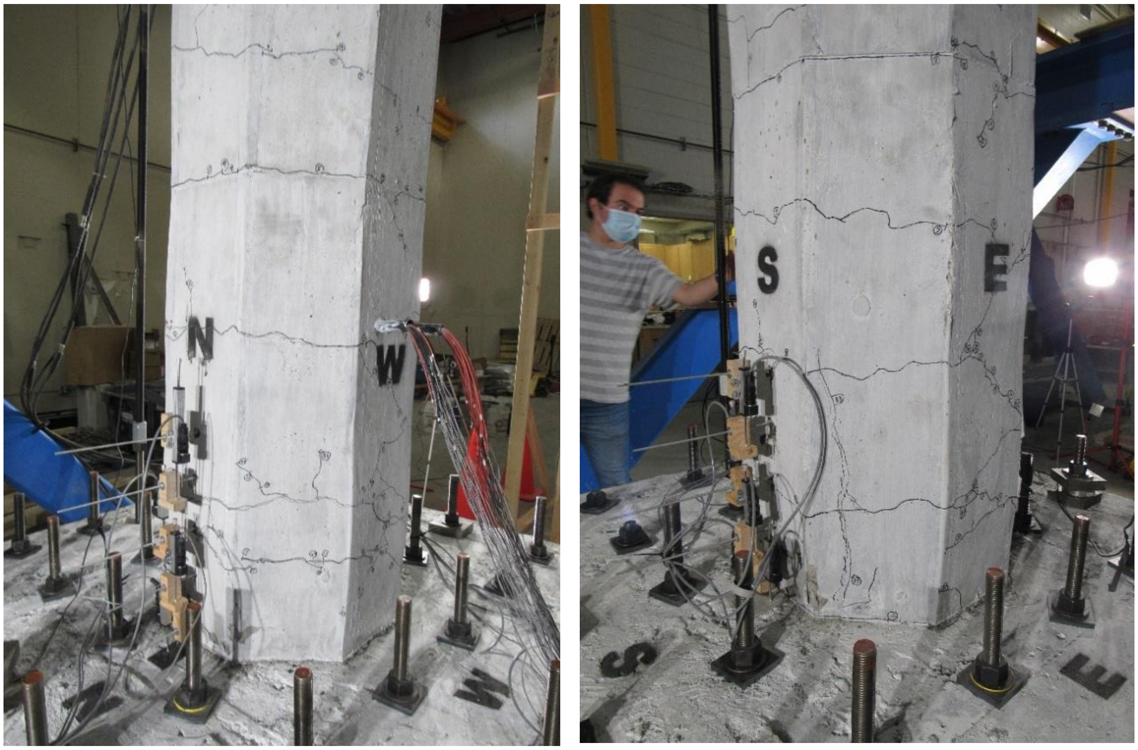

a) North-West Side b) South-East Side

Figure 3.35. CIP Column Plastic Hinge Damage, Second Push of 2.00% Drift Cycle

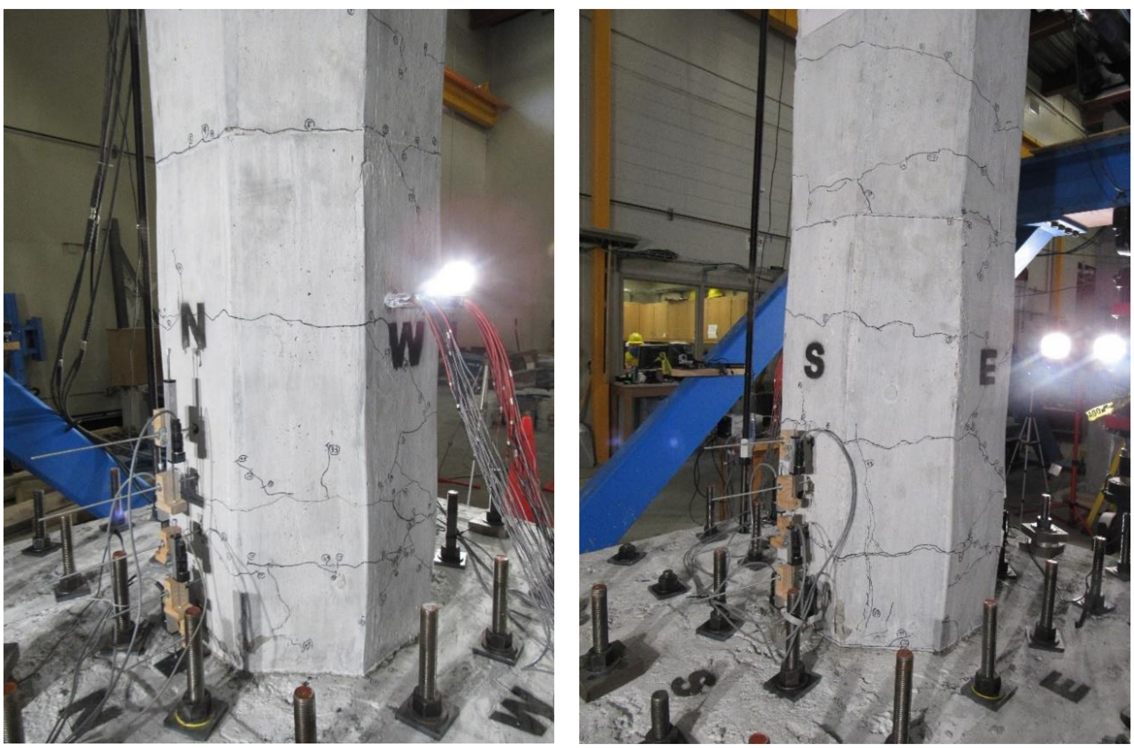

a) North-West Side b) South-East Side

Figure 3.36. CIP Column Plastic Hinge Damage, Second Pull of 2.00% Drift Cycle

a) North-West Side b) South-East Side

Figure 3.37. CIP Column Plastic Hinge Damage, Second Push of 3.00% Drift Cycle

a) North-West Side b) South-East Side

Figure 3.38. CIP Column Plastic Hinge Damage, Second Pull of 3.00% Drift Cycle

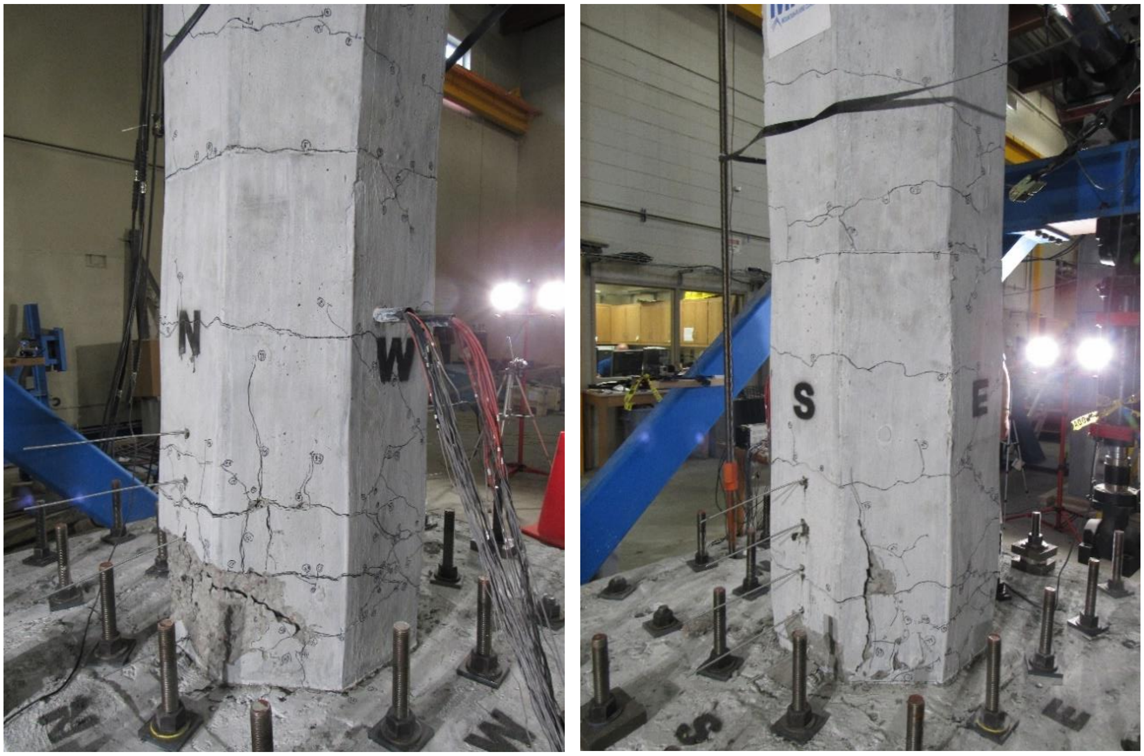

a) North-West Side b) South-East Side

Figure 3.39. CIP Column Plastic Hinge Damage, Second Push of 4.00% Drift Cycle

a) North-West Side b) South-East Side

Figure 3.40. CIP Column Plastic Hinge Damage, Second Pull of 4.00% Drift Cycle

a) North-West Side b) South-East Side

Figure 3.41. CIP Column Plastic Hinge Damage, Second Push of 5.00% Drift Cycle

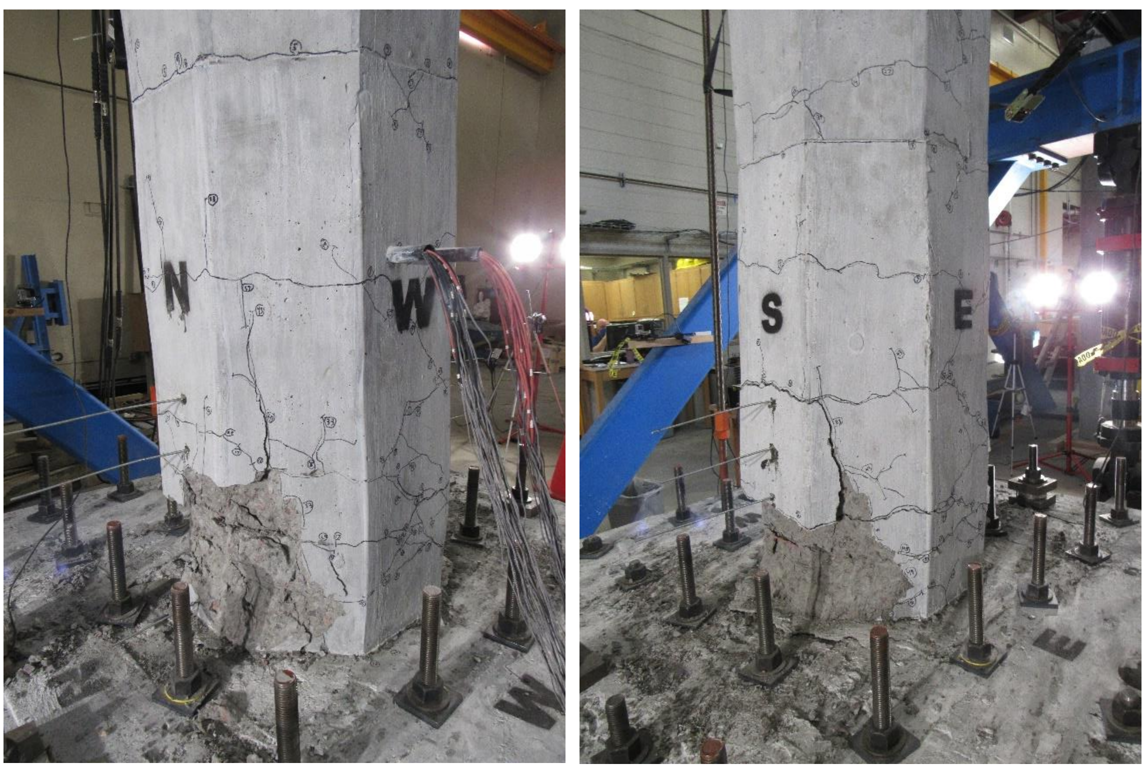

a) North-West Side b) South-East Side

Figure 3.42. CIP Column Plastic Hinge Damage, Second Pull of 5.00% Drift Cycle

a) North-West Side b) South-East Side

Figure 3.43. CIP Column Plastic Hinge Damage, Second Push of 6.00% Drift Cycle

a) North-West Side b) South-East Side

Figure 3.44. CIP Column Plastic Hinge Damage, Second Pull of 6.00% Drift Cycle

a) North-West Side b) South-East Side

Figure 3.45. CIP Column Plastic Hinge Damage, Second Push of 7.00% Drift Cycle

a) North-West Side b) South-East Side

Figure 3.46. CIP Column Plastic Hinge Damage, Second Pull of 7.00% Drift Cycle

a) North-West Side b) South-East Side

Figure 3.47. CIP Column Plastic Hinge Damage, Second Push of 8.00% Drift Cycle

a) North-West Side b) South-East Side

Figure 3.48. CIP Column Plastic Hinge Damage, Second Pull of 8.00% Drift Cycle

a) North-West Side b) South-East Side

Figure 3.49. CIP Column Plastic Hinge Damage, Second Push of 9.00% Drift Cycle

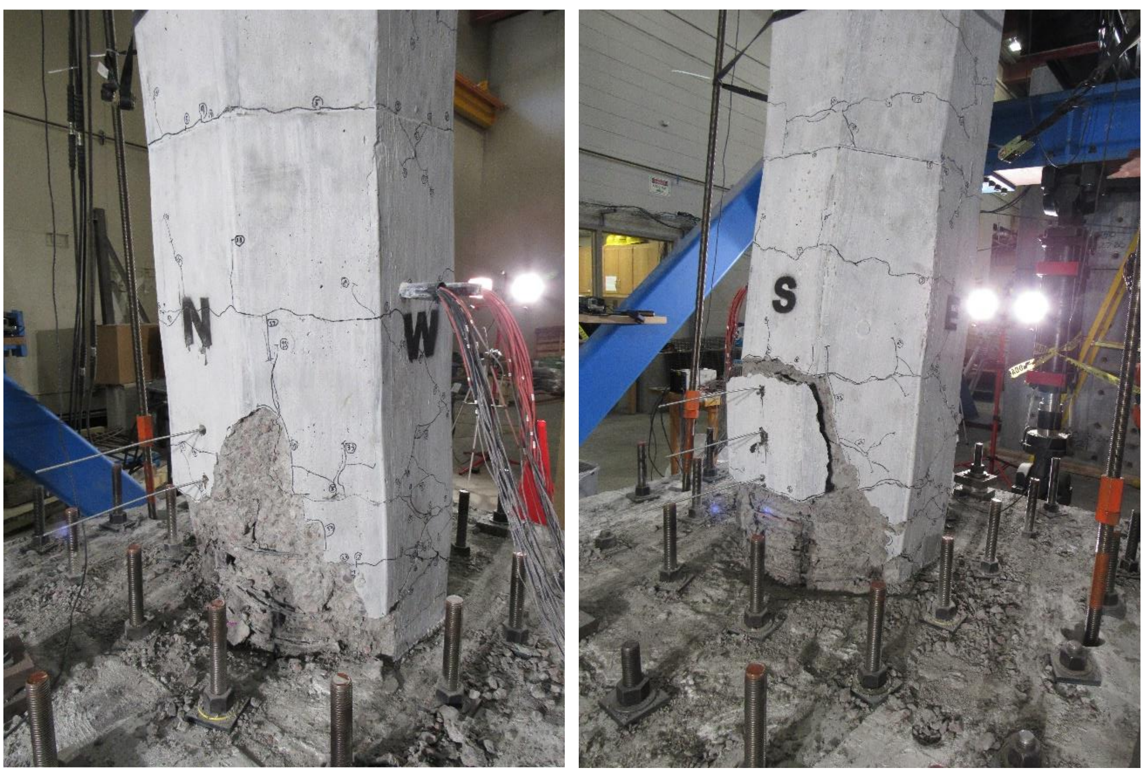

a) North-West Side b) South-East Side

Figure 3.50. CIP Column Plastic Hinge Damage, Second Pull of 9.00% Drift Cycle

a) North-West Side b) South-East Side

Figure 3.51. CIP Column Plastic Hinge Damage, Second Push of 10.00% Drift Cycle

a) North-West Side b) South-East Side

Figure 3.52. CIP Column Plastic Hinge Damage, Second Pull of 10.00% Drift Cycle

3.5.2.2 Force-Displacement Relationship

Figure 3.53 shows the measured lateral force-drift hysteretic and envelope responses of CIP. The envelope is shown until 85% of the base shear capacity. The CIP column had exhibited maximum shear capacity at 2% drift ratio and exhibited minor strength degradation from 2% to 9% drift. Significant strength and stiffness reduction was observed after 9% drift ratio due to reinforcement fracture. The column was slightly stronger in the pull direction. The CIP longitudinal bars yielded at 0.47% drift ratio in the push under a lateral load of 37.5 kips (166.9 kN), and at -0.44% drift ratio in the pull direction at a lateral load of -38.8 kips (172.6 kN).

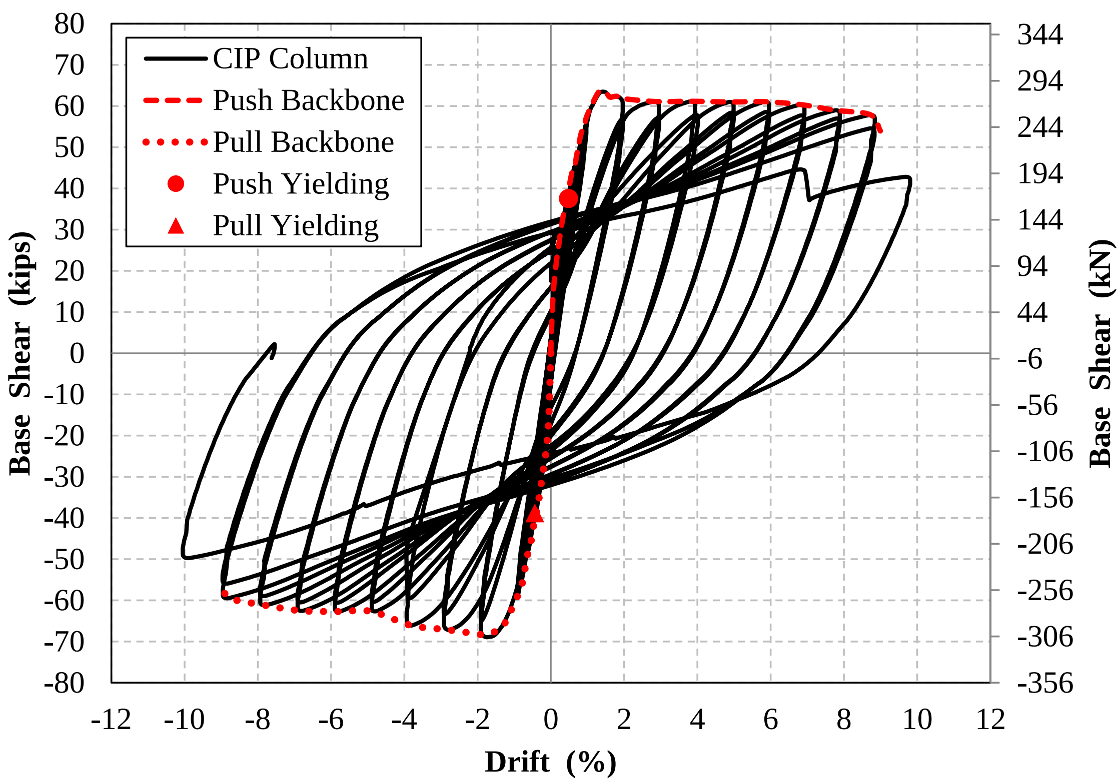

Figure 3.53. Measured CIP Column Force-Drift Hysteretic and Envelope Responses

Figure 3.54 shows the average envelope for the push and pull directions. The average yield drift ratio was 0.45% occurred at a lateral force of 38.2 kips (169.9 kN).

The column failure was the point at which the lateral resistance drops below 85% of the peak resistance due to either bar rupture or core concrete crushing. The ultimate drift capacity of the CIP column was 8.96% under this consideration. The displacement ductility is defined as the ratio of the ultimate displacement to the effective yield displacement per AASHTO SGS (2011). The effective yield displacement is found using an idealized bilinear force-displacement curve for the column. The bilinear curve is idealized by making the area under idealized and measured curve equal from the effective yield point to ultimate drift. Figure 3.54 shows the idealized curve for the average CIP envelope. The effective yield drift ratio was 0.72% at the effective yield lateral force of 61.9 kips (275.3 kN). Therefore, the displacement ductility capacity (μ) for the CIP column was 12.37.

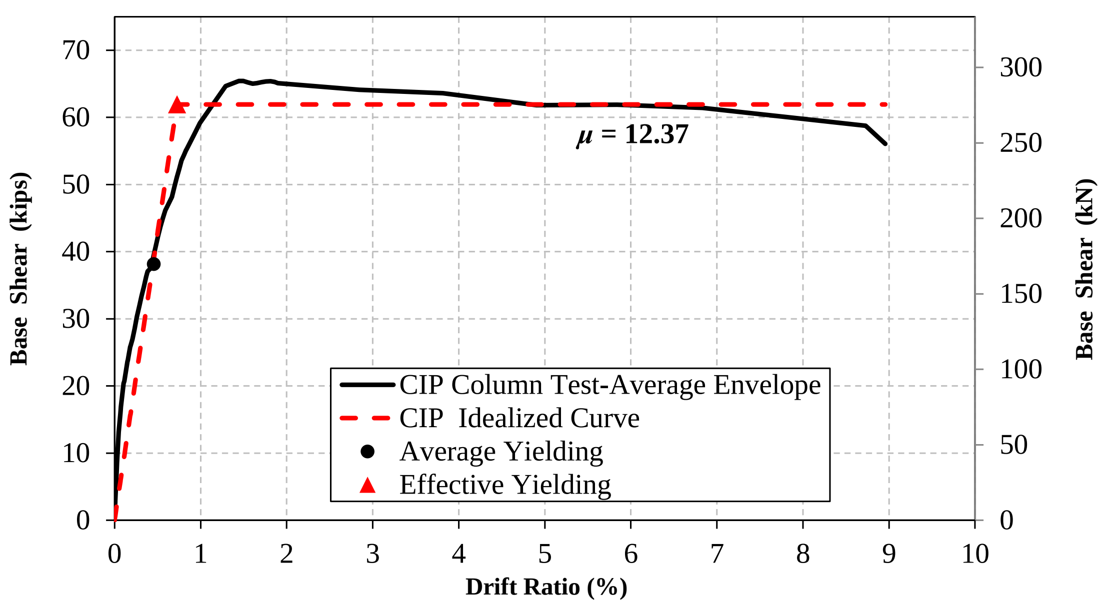

Figure 3.54. Measured CIP Column Average Push/Pull Force-Drift Envelope and Idealized Curve

3.5.2.3 Strain Profiles

Thirty-four strain gages were installed on the CIP reinforcing steel bars at six levels on the height of the column. Figure 3.55 to 3.58 show the maximum measured tensile strain versus the column height for Bars B1, B2, B6, and B7.

The strain profile was uniform until the bars began to yield. The strain was generally higher closer to the column-footing interface and decreased along the height of the column. The bar strains decreased significantly along the height of the column as the height exceeded the column analytical plastic hinge length (approximately 20 in. or 500 mm). Overall, strain was well distributed representing a well-designed modern RC bridge column performance.

The strain on the reinforcing hoops was also monitored. The yield strain for the hoops in CIP was 2.3%. The maximum measured strain in the hoops was 3.8% and occurred in a hoop near the column-footing interface.

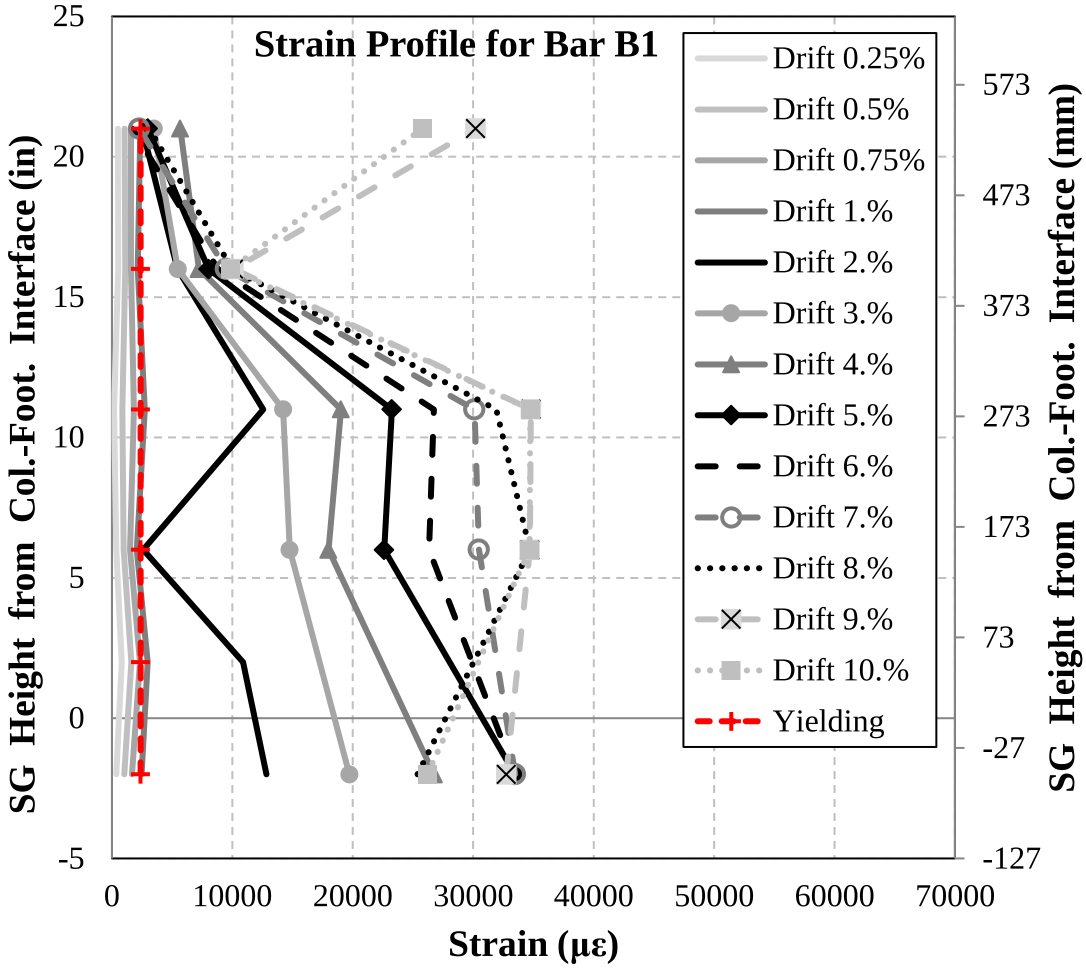

Figure 3.55. Measured Strain Profile for CIP Column Bar B1

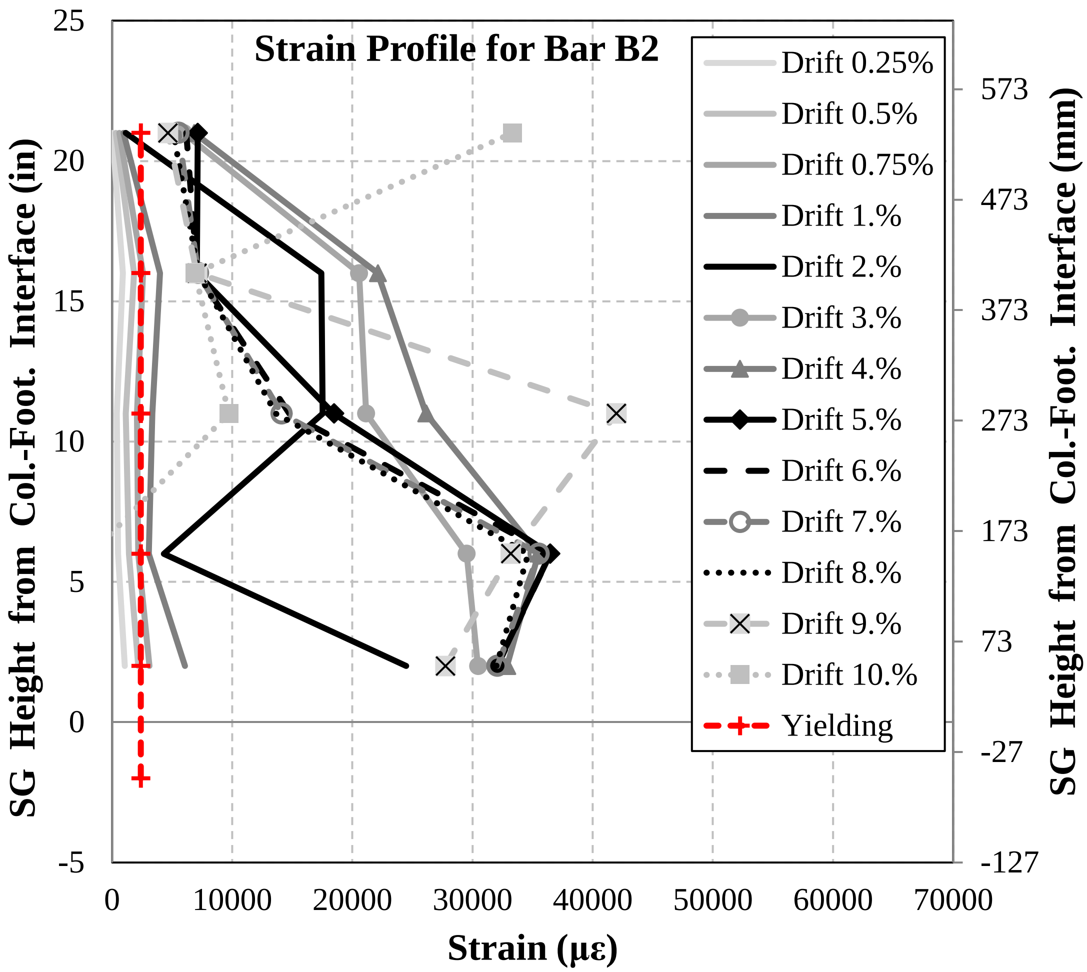

Figure 3.56. Measured Strain Profile for CIP Column Bar B2

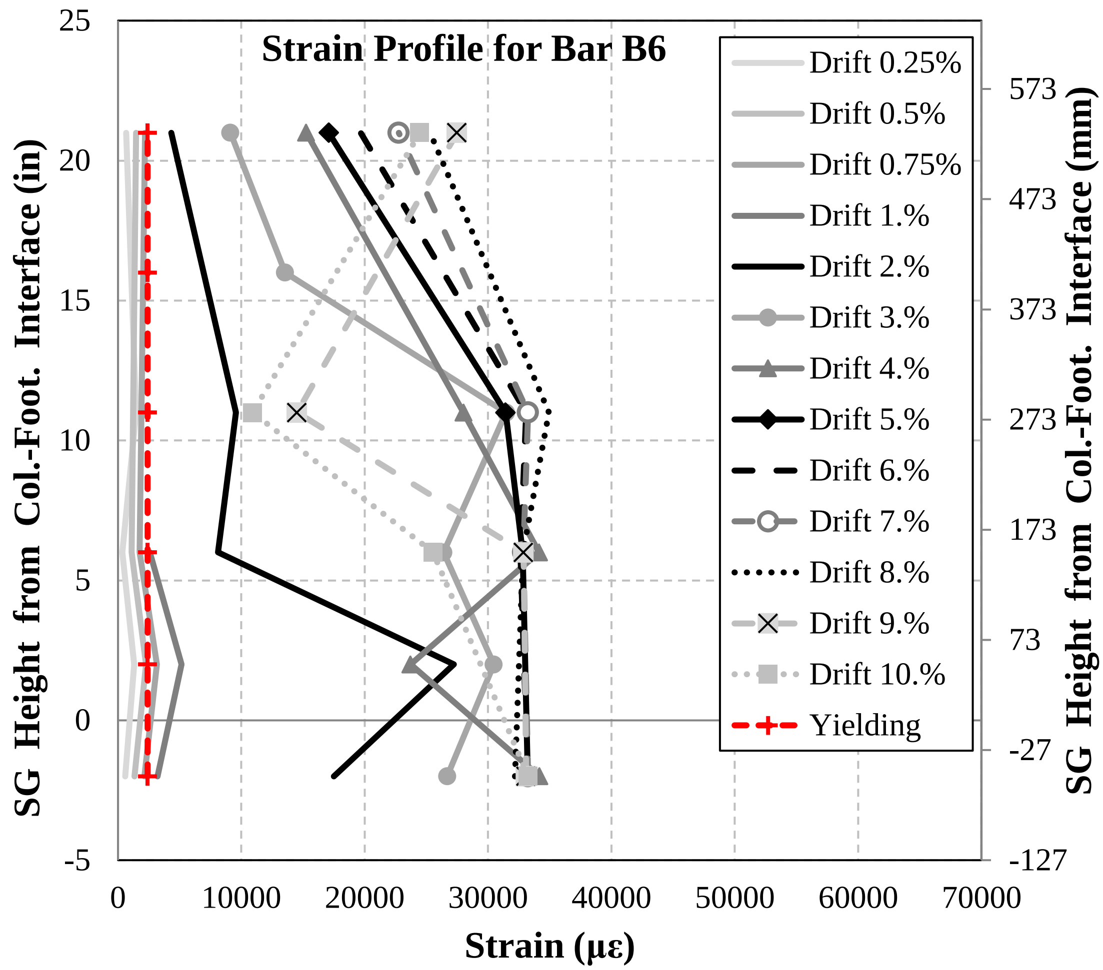

Figure 3.57. Measured Strain Profile for CIP Column Bar B6

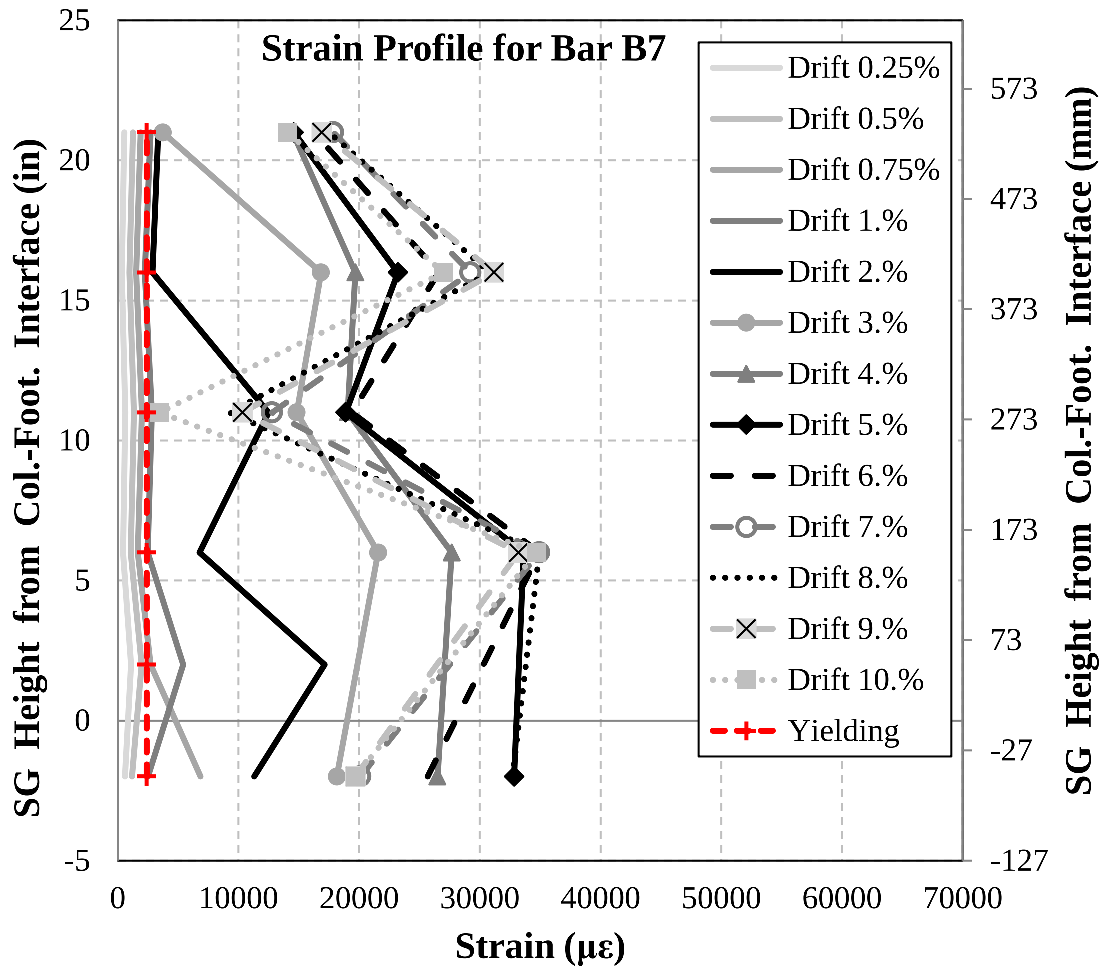

Figure 3.58. Measured Strain Profile for CIP Column Bar B7

3.5.2.4 Measured Rotation and Curvature

Linear variable displacement transducers (LVDT) were installed in the loading plane on the North and South faces of the column. The measured displacements were used to calculate rotations and curvatures in the plastic hinge region. Figure 3.20 shows the displacement instrumentation schedule for the CIP column. Rotation (θ) and curvature (φ)were calculated as follows:

$$\theta = \frac{\Delta L_L - \Delta L_R}{D + d_L + d_R} \tag{4-1}$$

$$\varphi = \frac{\theta}{h} \tag{4-2}$$

where ΔL_L and ΔL_R (in. or mm) are respectively the measured relative displacements at the left and right sides of the column in the loading direction, D (in. or mm) is the diameter of the column, d_L and d_R (in. or mm) are the distances of the left and right LVDTs from the column faces, respectively, and h is the height above the footing that the pair of LVDTs was placed. The rotations and curvatures were measured at five levels in the plastic hinge region.

Figure 3.59 shows the measured curvature profile along the height of the CIP column for drift ratios 0.25% to 4.0%. The highest curvature always occurred at the base due to concentrated concrete cracking and bar slip near the column-footing interface.

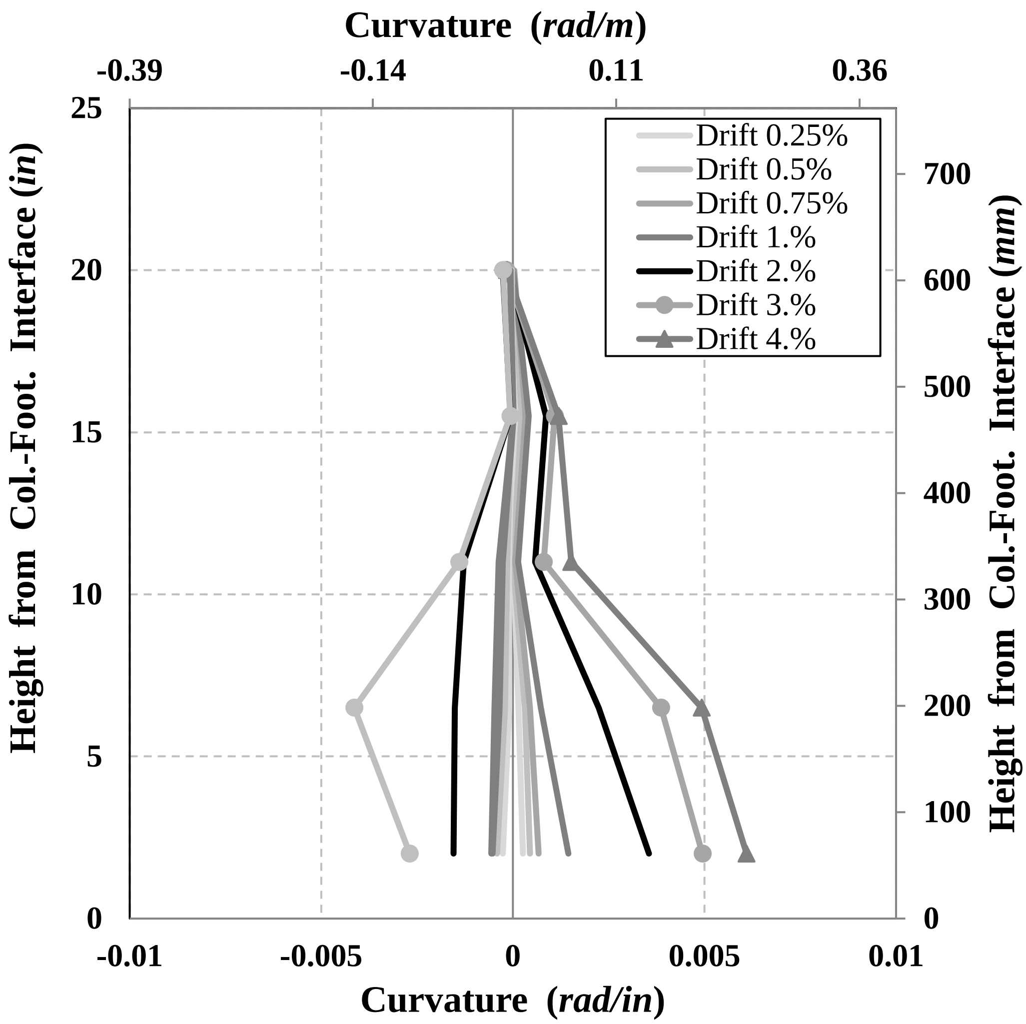

Figure 3.59. Measured Curvature Profile for CIP Column

3.5.2.5 Energy Dissipation

The dissipated energy is defined as the cumulative area under the force-displacement hysteretic loops. Figure 3.60 shows the measured cumulative energy dissipation of the CIP column at different drift ratios. The dissipated energy is negligible until 1% drift ratio, where bar yielding was minimal. At higher drift ratios, the hysteretic loops began to widen which led to a higher dissipated energy. CIP dissipated 8,041 kip-in. (2038 kN-m) of energy prior to the failure.

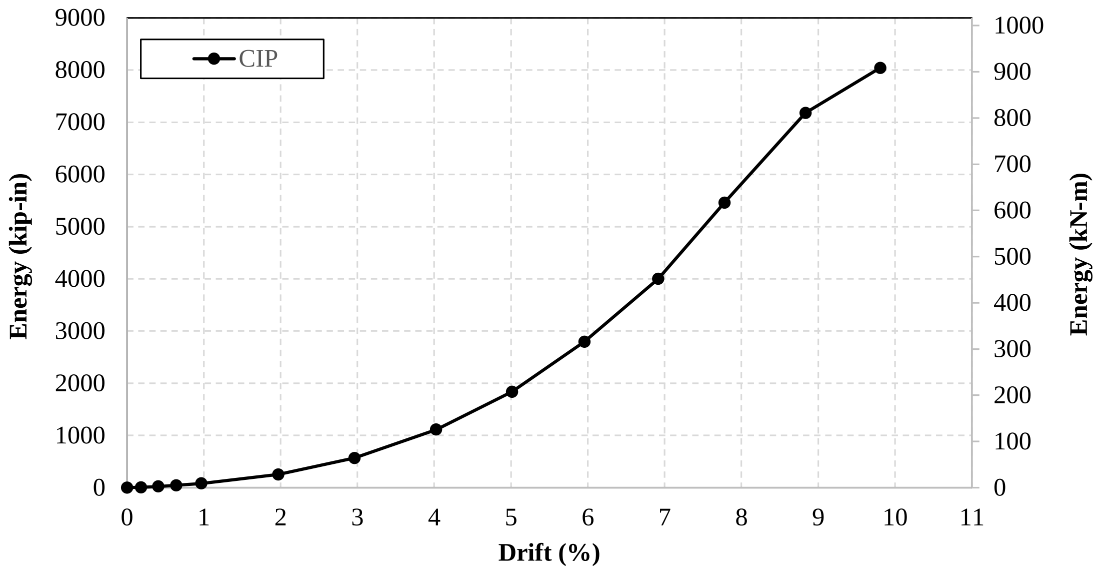

Figure 3.60. Measured Energy Dissipation for CIP Column

3.5.3 PGD Column Results

The seismic performance of the precast column incorporating the Dayton Superior Sleeve-Lock couplers, PGD, is discussed in this section.

3.5.3.1 Observed Damage

The PGD column followed the same testing procedure as the CIP column. Table 3.7 presents a summary of the damage observed for each push or pull load for the PGD column. Figures 3.61 to 3.78 show the PGD plastic hinge damage in the second cycle of push or push for each drift level.

Flexural cracks were occurred in the first cycle of 0.25% drift ratio (Fig. 3.61 & 3.62). Shear cracks were first observed in the first cycle of 0.5% drift ratio (Fig. 3.63 & 3.64). The first yielding occurred in Bar B1 at 0.58% drift in the first push run of the 0.75% drift cycle under a lateral load of 45.9 kips (204.3 kN) (Fig. 3.65). Concrete spalled on both the North and South faces of the column during the 3% drift cycles (Fig. 3.71 to 3.72). Cracks near the top of coupler and the base of the column began to spread

during the 4% drift cycle. The lateral strength also began to degrade during the 4% drift cycle (Fig. 3.73 & 3.74). Finally, the PGD longitudinal bars pulled out from the couplers at 6% drift cycle leading to a major strength reduction and ending the test (Fig. 3.77 & Fig. 3.78). A significant gap was observed at high displacements indicating bar pullout from the coupler base (e.g., 1.5-in. or 38-mm gap at 6% drift ratio).

The PGD Column mode of failure was longitudinal bar pullout during the 6% drift cycles.

Table 3.7. Summary of Damage in PGD

Drift Ratio, %	Observed Damage
+0.25	• Minor flexural cracks • Flexural cracks at top of coupler
-0.25	• Minor flexural cracks • Flexural cracks at top of coupler
+0.50	• Flexural and inclined cracks
-0.50	• Flexural and inclined cracks • Cracking at column base
+0.75	• Flexural Cracks • Bar Yielding
-0.75	• Flexural Cracks • Bar Yielding
+1.00	• No further damage
-1.00	• Vertical crack appears on Southeast column face
+2.00	• Vertical, flexural, and inclined cracks
-2.00	• Vertical, flexural, and inclined cracks
+3.00	• Widening of cracks • Initiation of spalling on South face of column
-3.00	• Widening of cracks • Initiation of spalling on North face of column
+4.00	• Beginning of strength degradation
-4.00	• Beginning of strength degradation
+5.00	• Large strength loss
-5.00	• Large strength loss
+6.00	• Longitudinal bar pulled out from coupler
-6.00	• Longitudinal bar pulled out from coupler

Note: Positive drifts were based on displacements away from the reaction blocks (North to South)

a) North-West Side b) South-East Side

Figure 3.61. PGD Column Plastic Hinge Damage, Second Push of 0.25% Drift Cycle

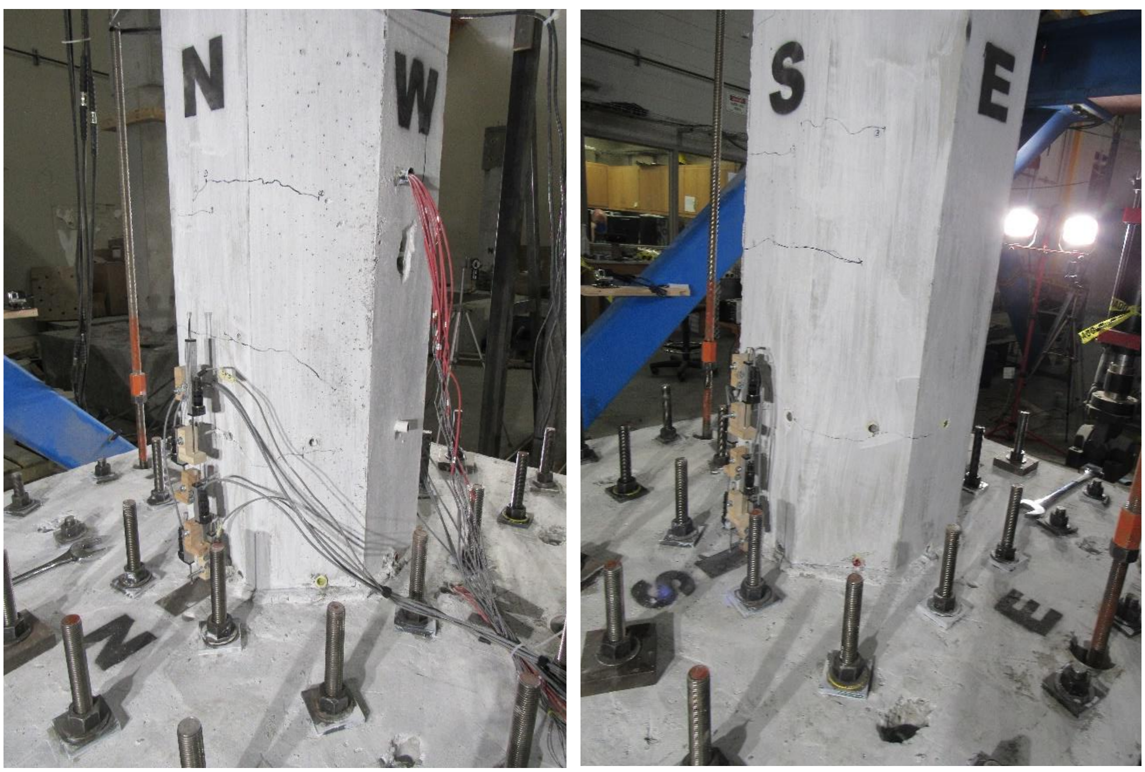

a) North-West Side b) South-East Side

Figure 3.62. PGD Column Plastic Hinge Damage, Second Pull of 0.25% Drift Cycle

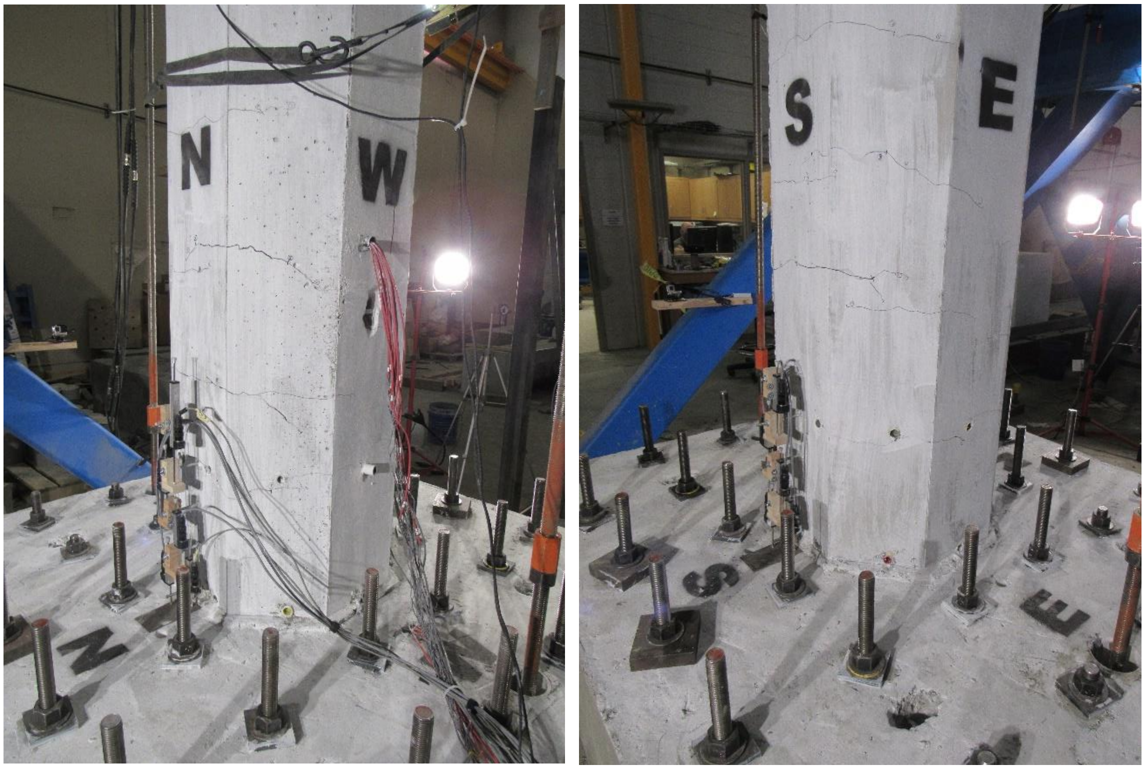

a) North-West Side b) South-East Side

Figure 3.63. PGD Column Plastic Hinge Damage, Second Push of 0.50% Drift Cycle

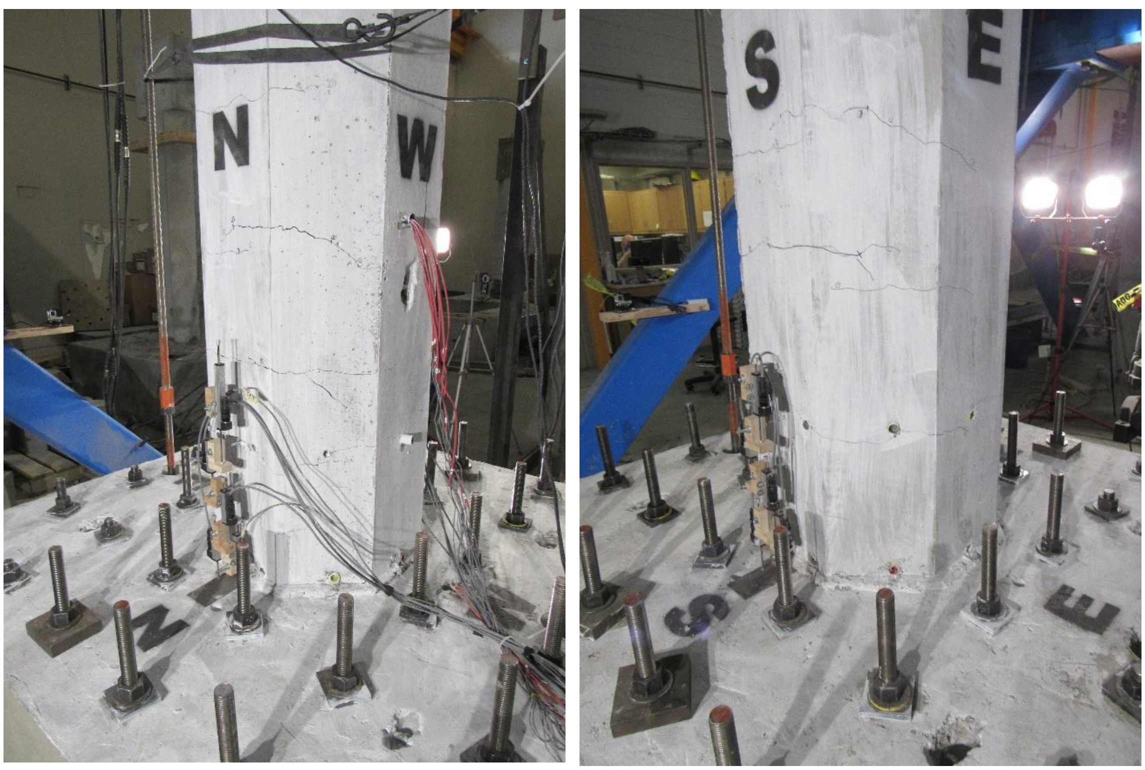

a) North-West Side b) South-East Side

Figure 3.64. PGD Column Plastic Hinge Damage, Second Pull of 0.50% Drift Cycle

a) North-West Side b) South-East Side

Figure 3.65. PGD Column Plastic Hinge Damage, Second Push of 0.75% Drift Cycle

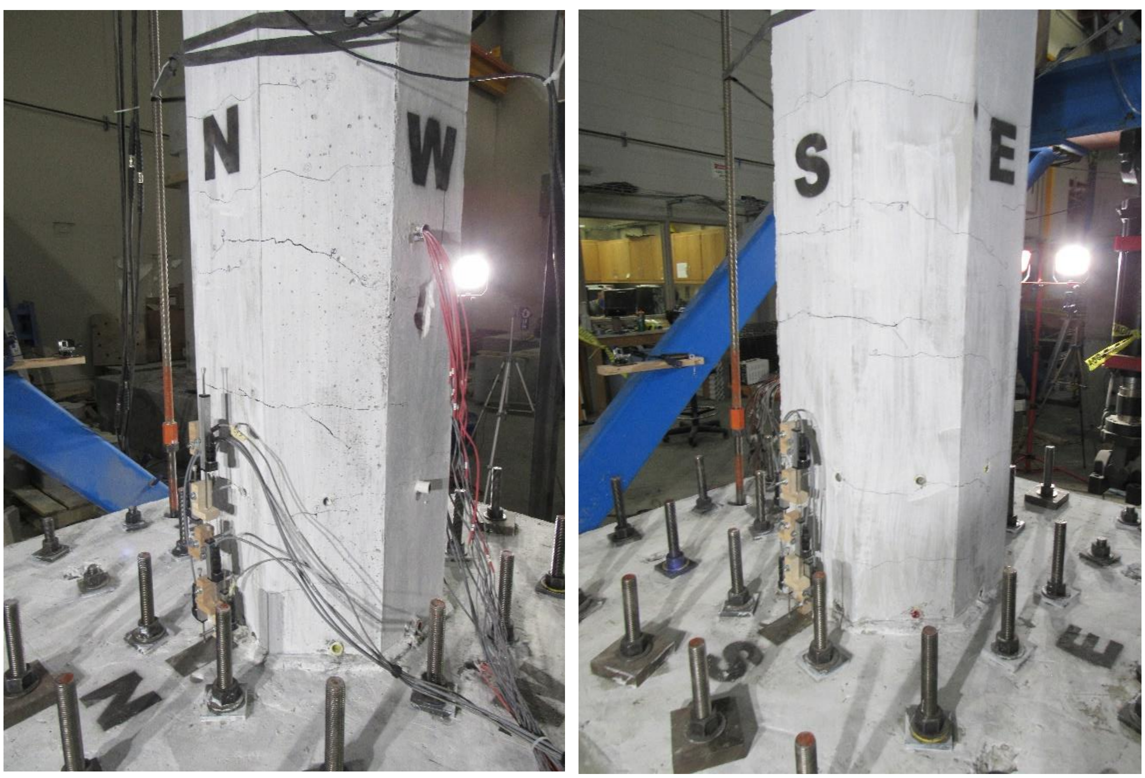

a) North-West Side b) South-East Side

Figure 3.66. PGD Column Plastic Hinge Damage, Second Pull of 0.75% Drift Cycle

a) North-West Side b) South-East Side

Figure 3.67. PGD Column Plastic Hinge Damage, Second Push of 1.00% Drift Cycle

a) North-West Side b) South-East Side

Figure 3.68. PGD Column Plastic Hinge Damage, Second Pull of 1.00% Drift Cycle

a) North-West Side b) South-East Side

Figure 3.69. PGD Column Plastic Hinge Damage, Second Push of 2.00% Drift Cycle

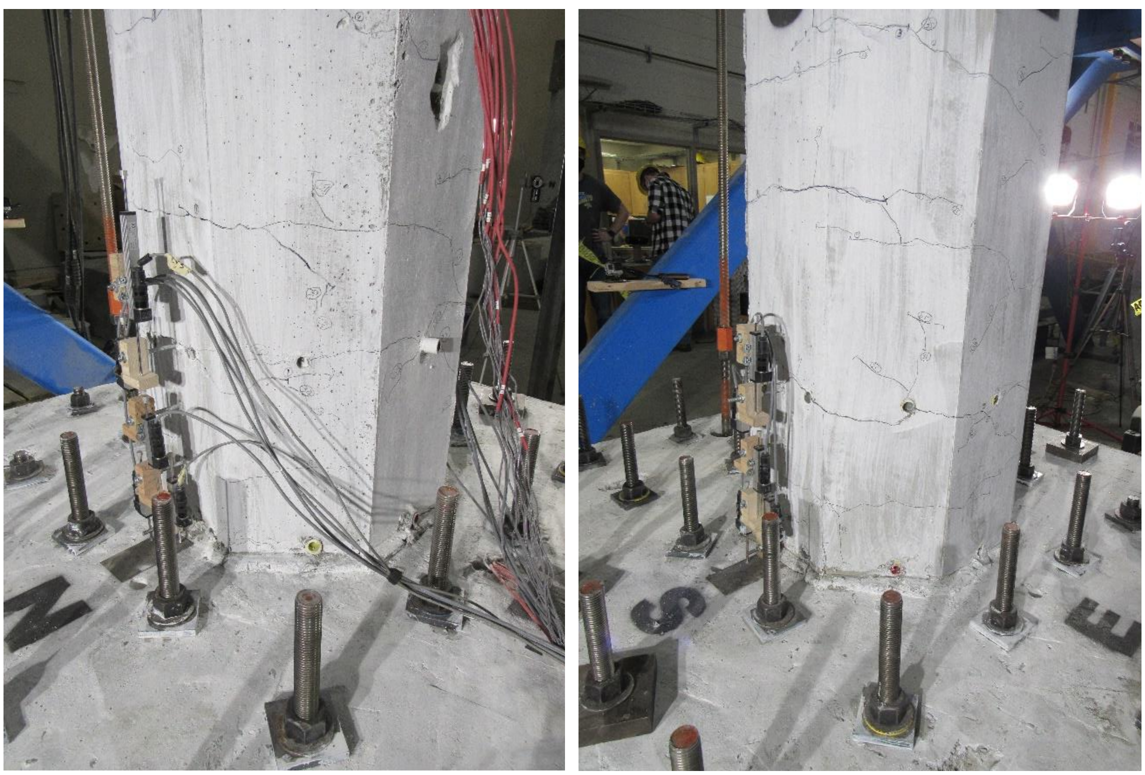

a) North-West Side b) South-East Side

Figure 3.70. PGD Column Plastic Hinge Damage, Second Pull of 2.00% Drift Cycle

a) North-West Side b) South-East Side

Figure 3.71. PGD Column Plastic Hinge Damage, Second Push of 3.00% Drift Cycle

a) North-West Side b) South-East Side

Figure 3.72. PGD Column Plastic Hinge Damage, Second Pull of 3.00% Drift Cycle

a) North-West Side b) South-East Side

Figure 3.73. PGD Column Plastic Hinge Damage, Second Push of 4.00% Drift Cycle

a) North-West Side b) South-East Side

Figure 3.74. PGD Column Plastic Hinge Damage, Second Pull of 4.00% Drift Cycle

a) North-West Side b) South-East Side

Figure 3.75. PGD Column Plastic Hinge Damage, Second Push of 5.00% Drift Cycle

a) North-West Side b) South-East Side

Figure 3.76. PGD Column Plastic Hinge Damage, Second Pull of 5.00% Drift Cycle

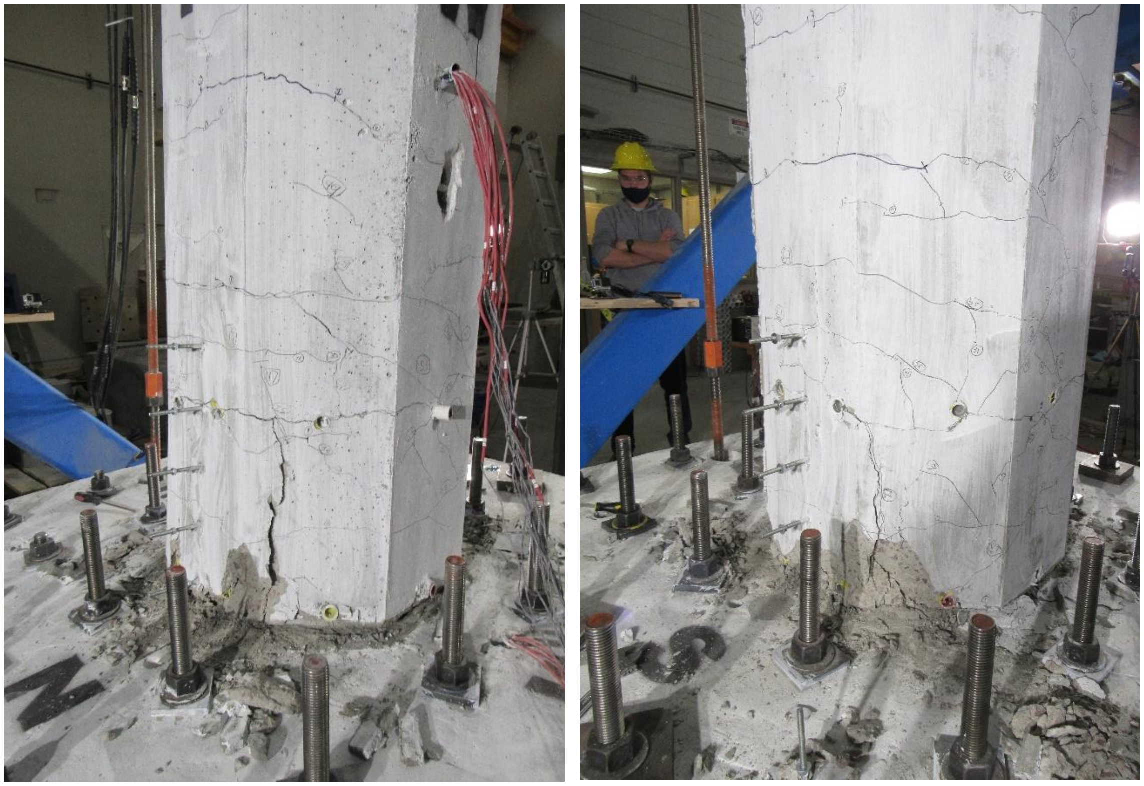

a) North-West Side b) South-East Side

Figure 3.77. PGD Column Plastic Hinge Damage, Second Push of 6.00% Drift Cycle

a) North-West Side b) South-East Side

Figure 3.78. PGD Column Plastic Hinge Damage, Second Pull of 6.00% Drift Cycle

3.5.3.2 Force-Displacement Relationship

Figure 3.79 shows the measured lateral force-drift hysteretic and envelope responses of PGD. The envelope is shown until 85% of the base shear capacity. The PGD column exhibited a maximum lateral load of 74.7 kips (332 kN)- at 3% drift ratio and exhibited a steady strength degradation afterwards. A significant strength and stiffness degradation was observed after 5% drift ratio due to bar pullout from the coupler base. The column was slightly stronger in the push direction. The PGD longitudinal bars yielded at 0.58% drift ratio in the push under a lateral load of 45.9 kips (204.3 kN), and at -0.52% drift ratio in the pull direction at a lateral load of -46.4 kips (206.3 kN).

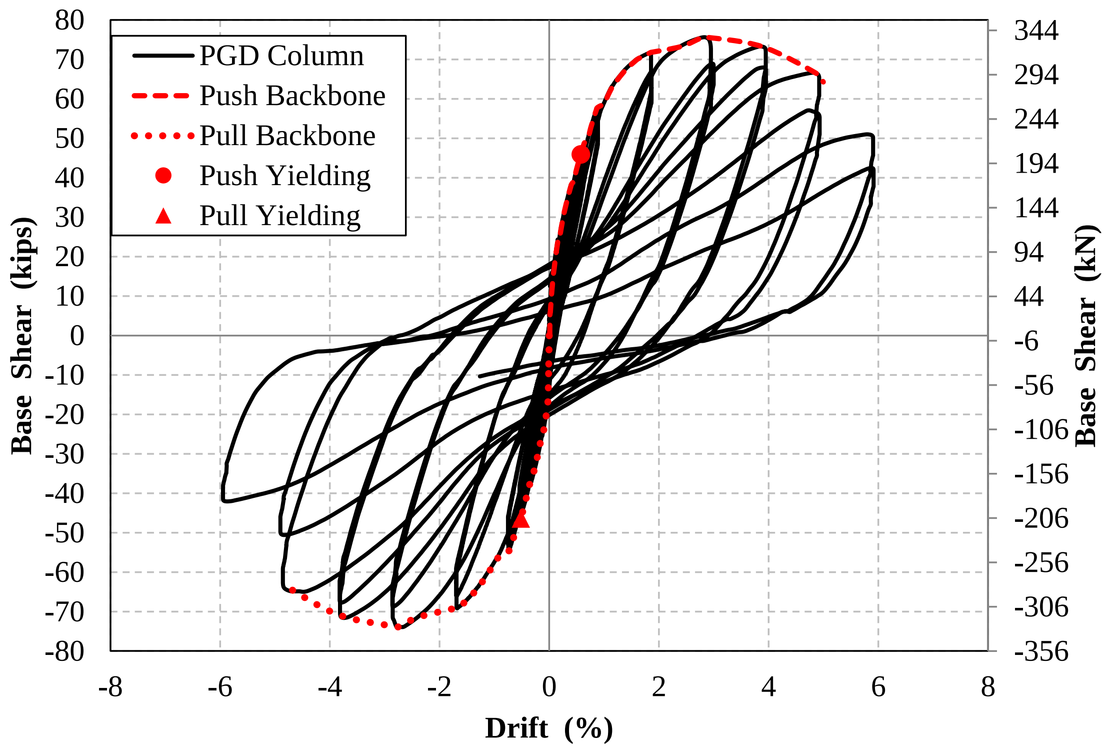

Figure 3.79. Measured PGD Column Force-Drift Hysteretic and Envelope Responses

Figure 3.80 shows the average envelope for the push and pull directions of PGD. The average yield drift ratio was 0.55% occurred at a lateral force of 46.2 kips (205.5

kN). Based on the 15% load drop discussed before as the column failure point, the drift capacity of the PGD column was estimated as 4.93%. Furthermore, Fig. 3.80 shows the idealized curve for the average PGD envelope. The effective yield drift ratio was 0.86% at the effective yield lateral force of 70.4 kips (313.2 kN) resulting in a displacement ductility capacity of 5.76 for the PGD column.

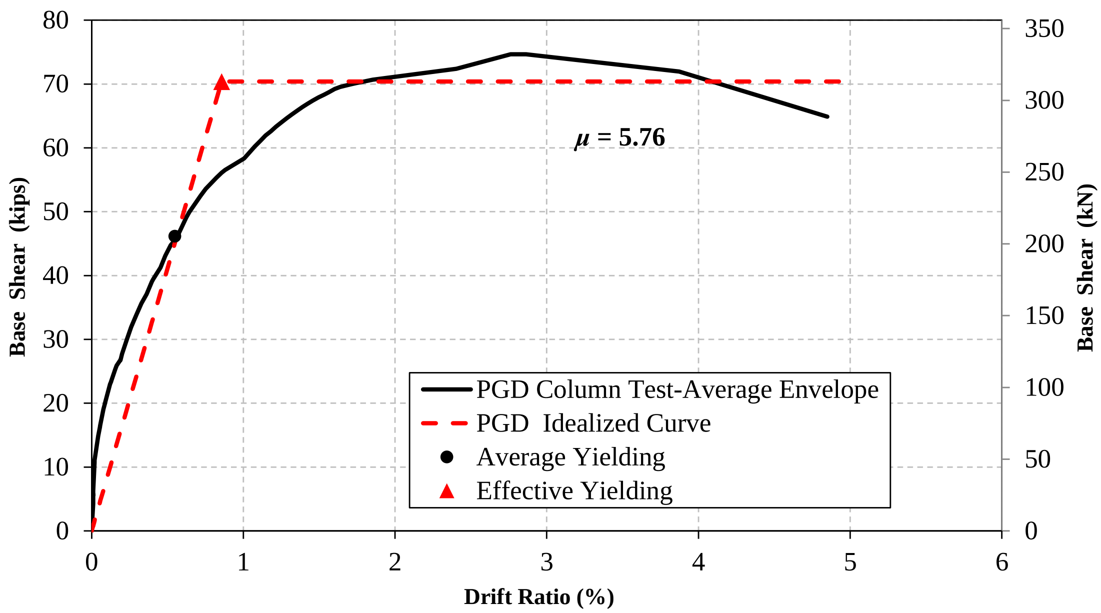

Figure 3.80. Measured PGD Column Average Push/Pull Force-Drift Envelope and Idealized Curve

3.5.3.3 Strain Profiles

Seventeen strain gages were installed on the PGD reinforcing steel bars at three levels on the column height. Figures 3.81 to 3.84 show the measured strain profiles of the column for Bars B1, B2, B6, and B7.

The strain profile was uniform prior to the bar yielding. The strain was generally higher closer to the column-footing-interface and decreased along the height of the column once the bars yielded. The bar strains decreased significantly along the height of the column as the height exceeded the column analytical plastic hinge length

(approximately 20 in. or 500 mm). It should be noted that the strain profiles for a mechanically spliced column do not follow those of CIP because couplers are stiff and strong and shift the nonlinearity away from the coupler regions. Thus, the column longitudinal bar strains are higher at the coupler ends. This observation will be discussed further in Sec. 3.6.

The strain on the reinforcing hoops was also monitored. The yield strain for the hoops in precast columns was 2.3%. The maximum measured strain in the hoops was 0.1% and occurred in a hoop near the column-footing interface.

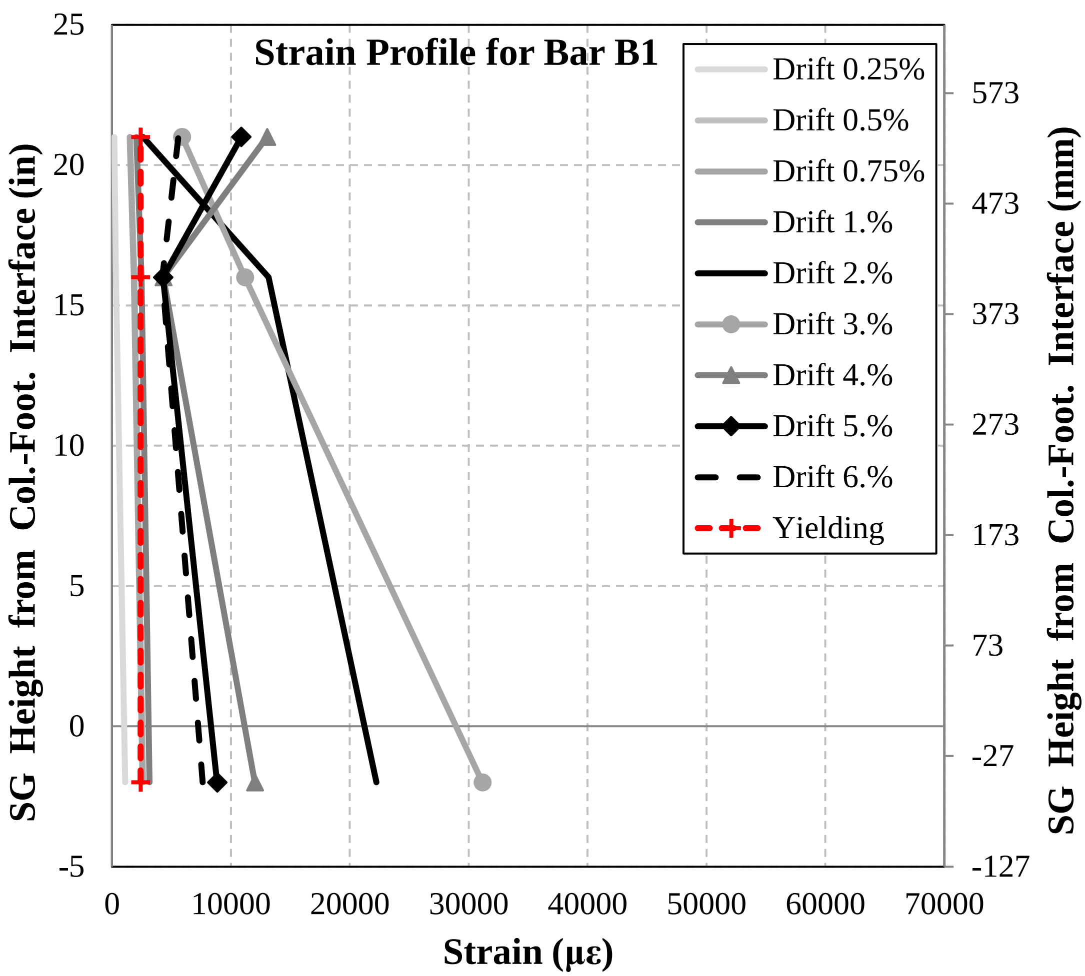

Figure 3.81. Measured Strain Profile for PGD Column Bar B1

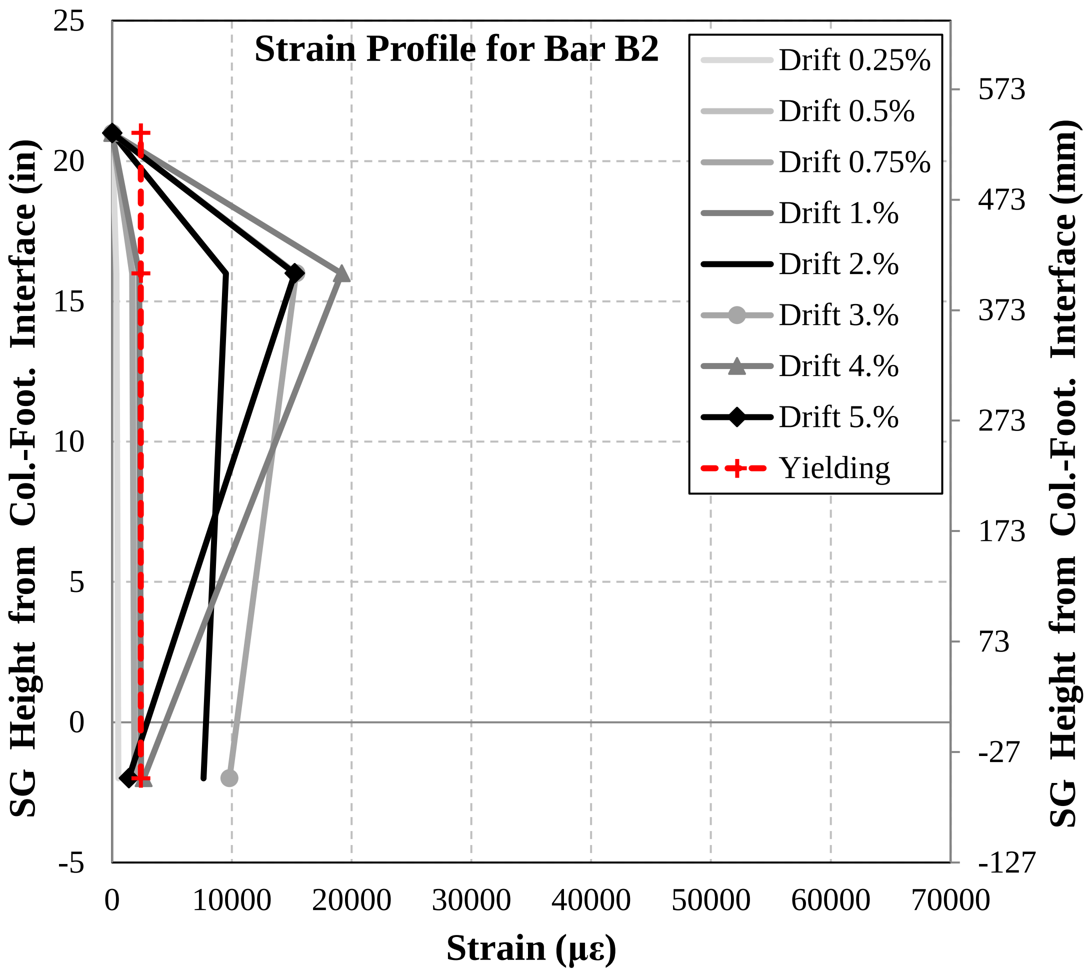

Figure 3.82. Measured Strain Profile for PGD Column Bar B2

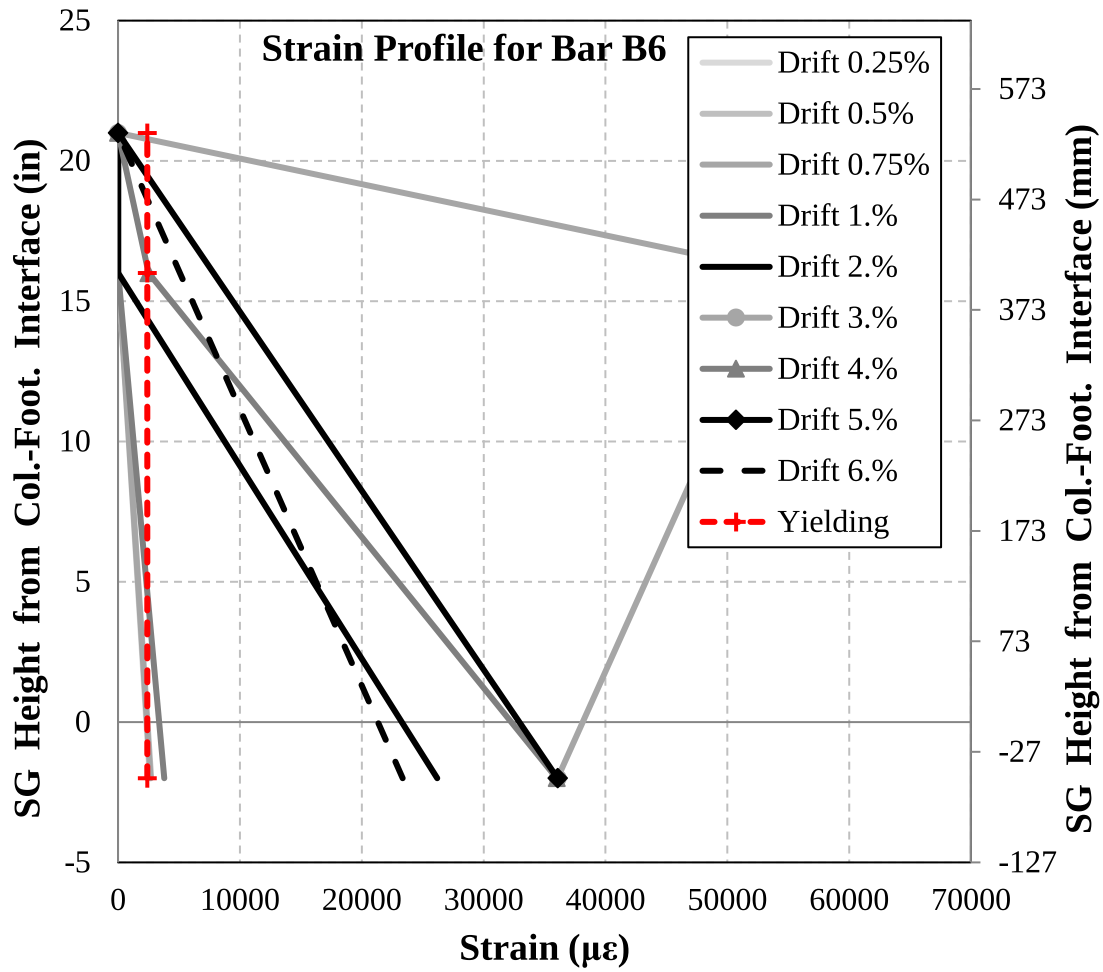

Figure 3.83. Measured Strain Profile for PGD Column Bar B6

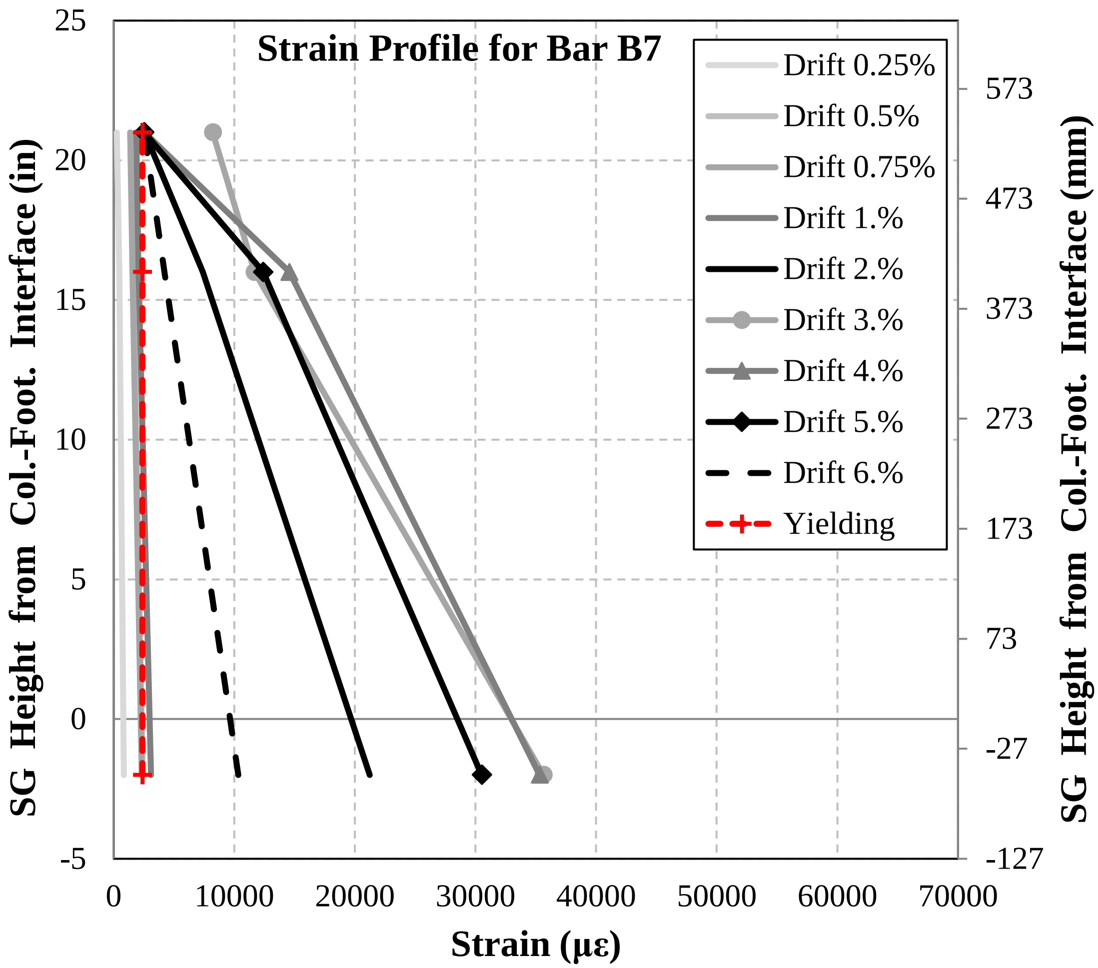

Figure 3.84. Measured Strain Profile for PGD Column Bar B7

3.5.3.4 Measured Rotation and Curvature

Rotations and curvatures were determined in the same manner as CIP. Figure 3.85 shows the measured curvature profile for the PGD column at drift ratios of 0.25% to 4.0%. The highest curvature always occurred at the base due to concentrated concrete cracking and bar-slip near the column-footing interface. The grouted couplers used in PGD increased the column stiffness in the coupler region leading to a shift of nonlinearity outside of the coupler. The figure confirms this observation in which the curvature was

relatively high near the column base, minimal along the coupler region, and high above the coupler levels.

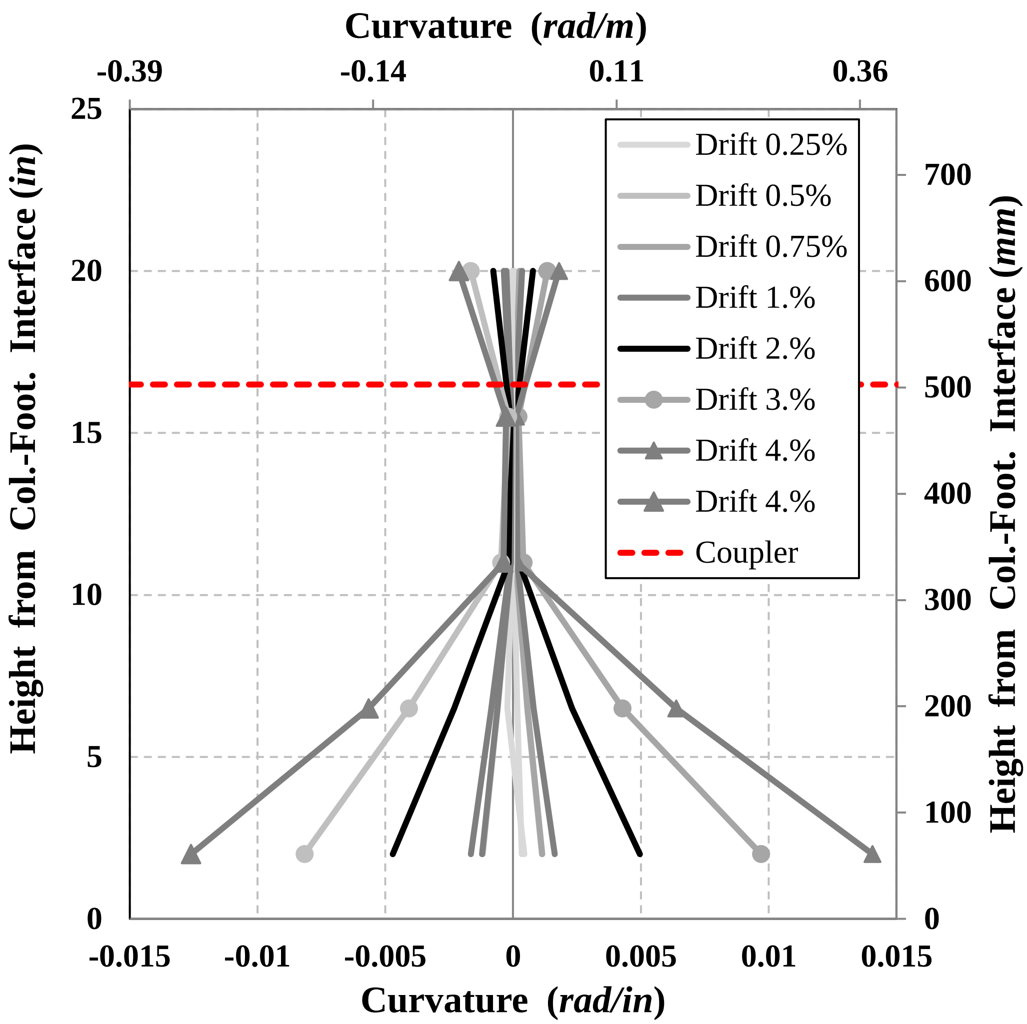

Figure 3.85. Measured Curvature Profile for PGD Column

3.5.3.5 Energy Dissipation

Figure 3.86 shows the measured cumulative energy dissipation of the PGD column at different drift ratios. The dissipated energy is negligible until 1% drift ratio, where bar yielding was minimal. At higher drift ratios, the hysteretic loops began to widen which led to a higher dissipated energy. PGD dissipated 2,036 kip-in. (230 kN-m) of energy prior to the failure.

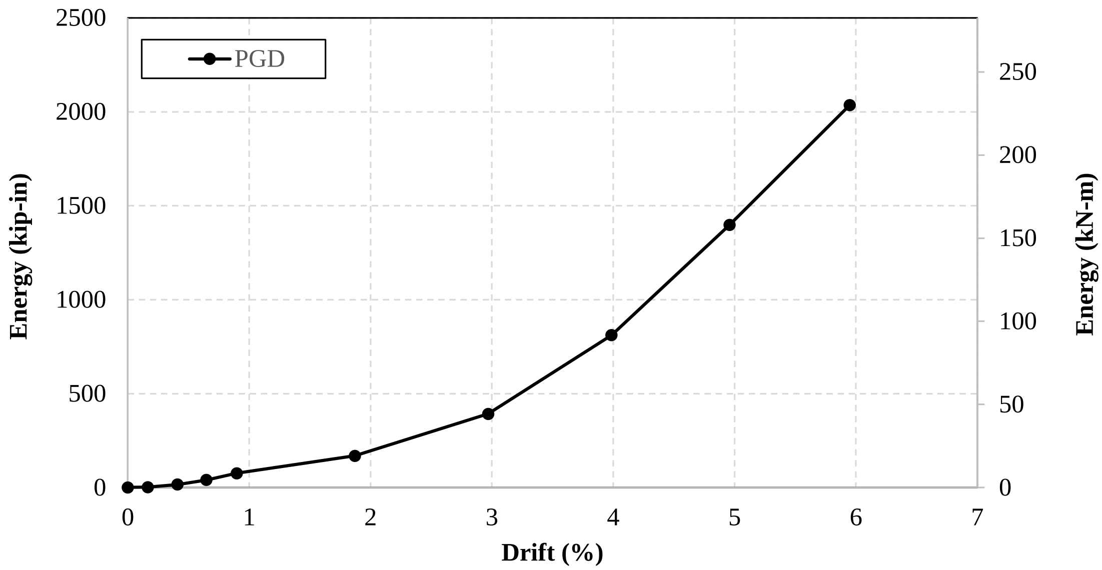

Figure 3.86. Measured Energy Dissipation for PGD Column

3.5.4 PGS Column Results

The seismic performance of the precast column using the NMB Splice Sleeve grouted coupler, PGS, is presented in this section.

3.5.4.1 Observed Damage

The PGS column followed the same testing procedure as the CIP column. Table 3.8 presents a summary of the damage observed for each push or pull load for the PGS column. Figures 3.87 to 3.110 show the PGS plastic hinge damage in the second cycle of push or push for each drift level.

Flexural cracks were occurred in the first cycle of 0.25% drift ratio (Fig. 3.87 & 3.88). Shear cracks were first observed in the first cycle of 0.5% drift ratio (Fig. 3.89 & 3.90). The first yielding in occurred in bar B1 at 0.66% drift in the first push run of the 0.75% drift cycle under a lateral load of 48.4 kips (215.9 kN) (Fig. 3.91). Concrete spalling began to occur on both the North and South faces of the column during the 3%

drift cycles (Fig. 3.97 & 3.98). Transverse bars became exposed on the North face of the column during the 4% drifty cycle (Fig. 3.99 & 3.100). Transverse bars first became exposed on the South face of the column while all transverse bars on the North face of the column became exposed during the 7% drift cycle (Fig. 3.105 & 3.106). Portions of the coupler and longitudinal bar became exposed on the North face of the column during the 8% drift cycle (Fig. 3.107 & 3.108). Finally, longitudinal bars pulled out of the couplers on the North face of the column and ruptured on the South face of the column during the 9% drift cycle leading to a major strength reduction and the end of the test (Fig. 3.109 & 3.110).

The PGS Column mode of failure was longitudinal bar rupture during the 9% drift cycles.

Table 3.8. Summary of Damage in PGS

Drift Ratio, %	Observed Damage
+0.25	• Minor flexural cracks
-0.25	• Minor flexural cracks
+0.50	• Flexural and inclined cracks
-0.50	• Flexural and inclined cracks • Cracking at column base
+0.75	• Flexural Cracks • Bar Yielding
-0.75	• Flexural Cracks • Bar Yielding
+1.00	• Widening of cracks
-1.00	• Widening of cracks
+2.00	• Vertical, flexural, and inclined cracks
-2.00	• Vertical, flexural, and inclined cracks
+3.00	• Widening of cracks • Initiation of spalling on South face of column
-3.00	• Widening of cracks • Initiation of spalling on North face of column
+4.00	• Widening of cracks
-4.00	• Widening of cracks • Transverse bars exposed on the North Face of column
+5.00	• Increased spalling
-5.00	• Increased spalling
+6.00	• Several transverse bars exposed on North Face of column
-6.00	• Increased spalling
+7.00	• All plastic hinge transverse bars exposed on North face of column • Longitudinal bar exposed on North face of column
-7.00	• Transverse bars exposed on South face of column
+8.00	• Coupler and longitudinal bar exposed on North face of column
-8.00	• No further damage
+9.00	• Strength reduction due to longitudinal bar pull out on North face of column
-9.00	• Longitudinal bar rupture on South face of column

Note: Positive drifts were based on displacements away from the reaction blocks (North to South)

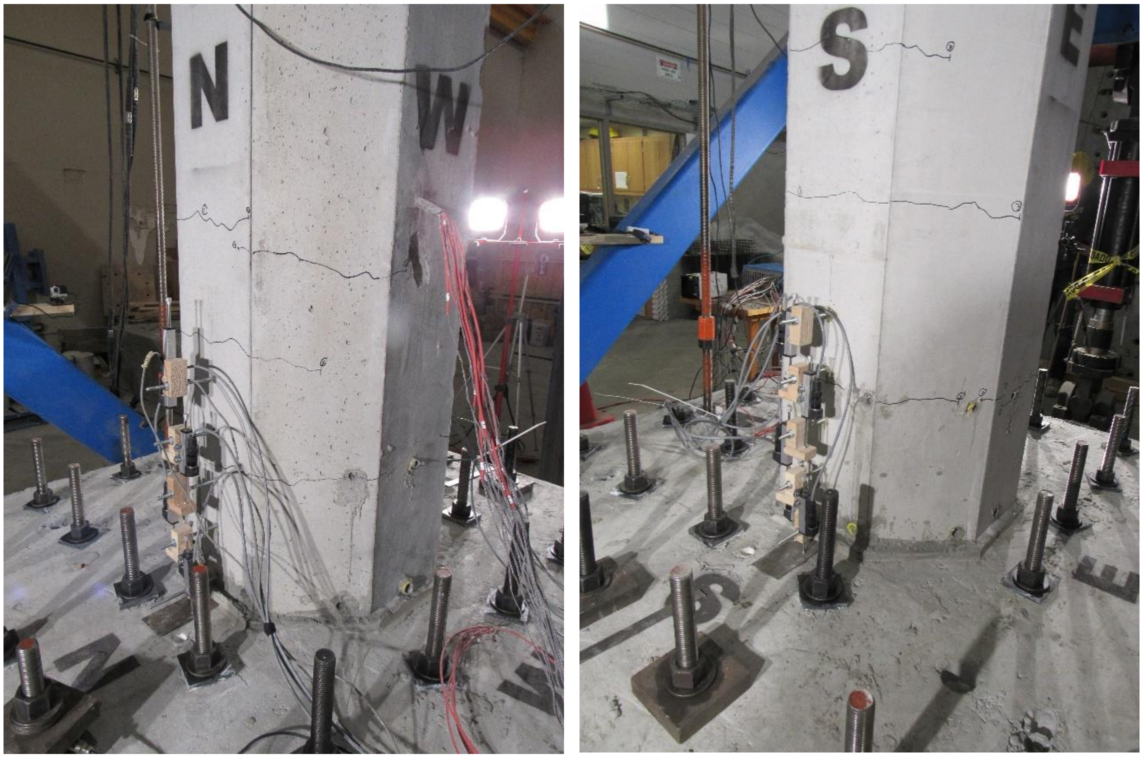

a) North-West Side b) South-East Side

Figure 3.87. PGS Column Plastic Hinge Damage, Second Push of 0.25% Drift Cycle

a) North-West Side b) South-East Side

Figure 3.88. PGS Column Plastic Hinge Damage, Second Pull of 0.25% Drift Cycle

a) North-West Side b) South-East Side

Figure 3.89. PGS Column Plastic Hinge Damage, Second Push of 0.50% Drift Cycle

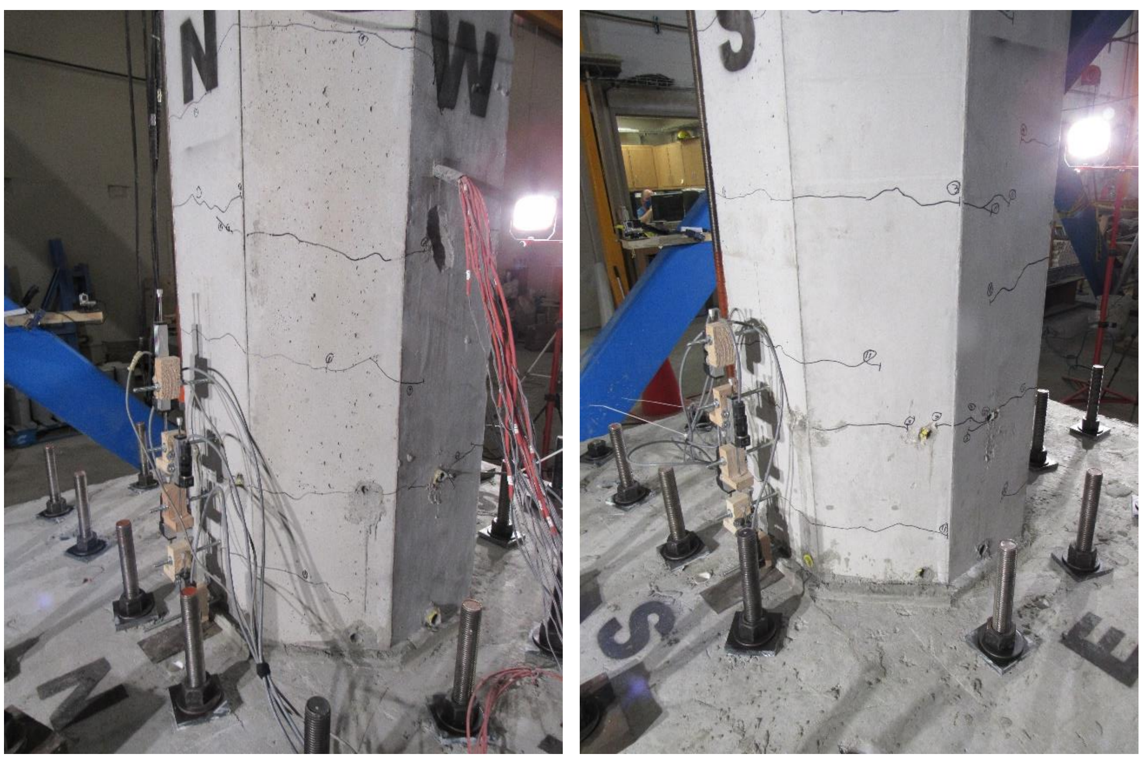

a) North-West Side b) South-East Side

Figure 3.90. PGS Column Plastic Hinge Damage, Second Pull of 0.50% Drift Cycle

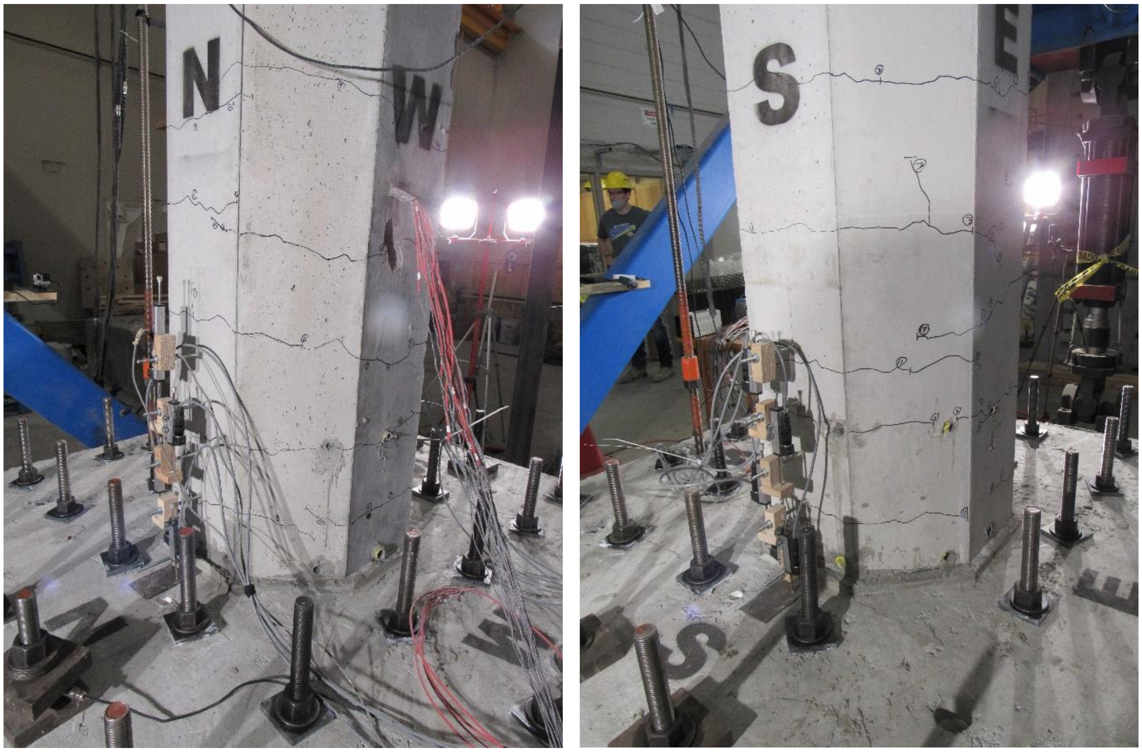

a) North-West Side b) South-East Side

Figure 3.91. PGS Column Plastic Hinge Damage, Second Push of 0.75% Drift Cycle

a) North-West Side b) South-East Side

Figure 3.92. PGS Column Plastic Hinge Damage, Second Pull of 0.75% Drift Cycle

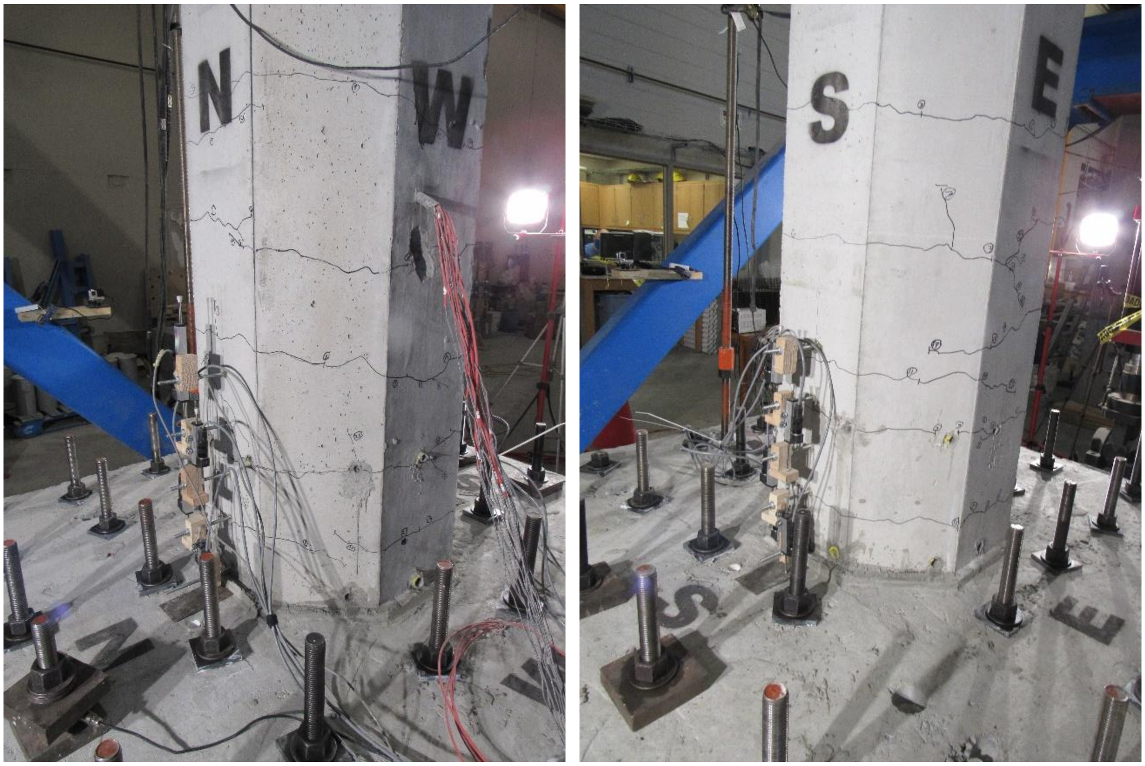

a) North-West Side b) South-East Side

Figure 3.93. PGS Column Plastic Hinge Damage, Second Push of 1.00% Drift Cycle

a) North-West Side b) South-East Side

Figure 3.94. PGS Column Plastic Hinge Damage, Second Pull of 1.00% Drift Cycle

a) North-West Side b) South-East Side

Figure 3.95. PGS Column Plastic Hinge Damage, Second Push of 2.00% Drift Cycle

a) North-West Side b) South-East Side

Figure 3.96. PGS Column Plastic Hinge Damage, Second Pull of 2.00% Drift Cycle

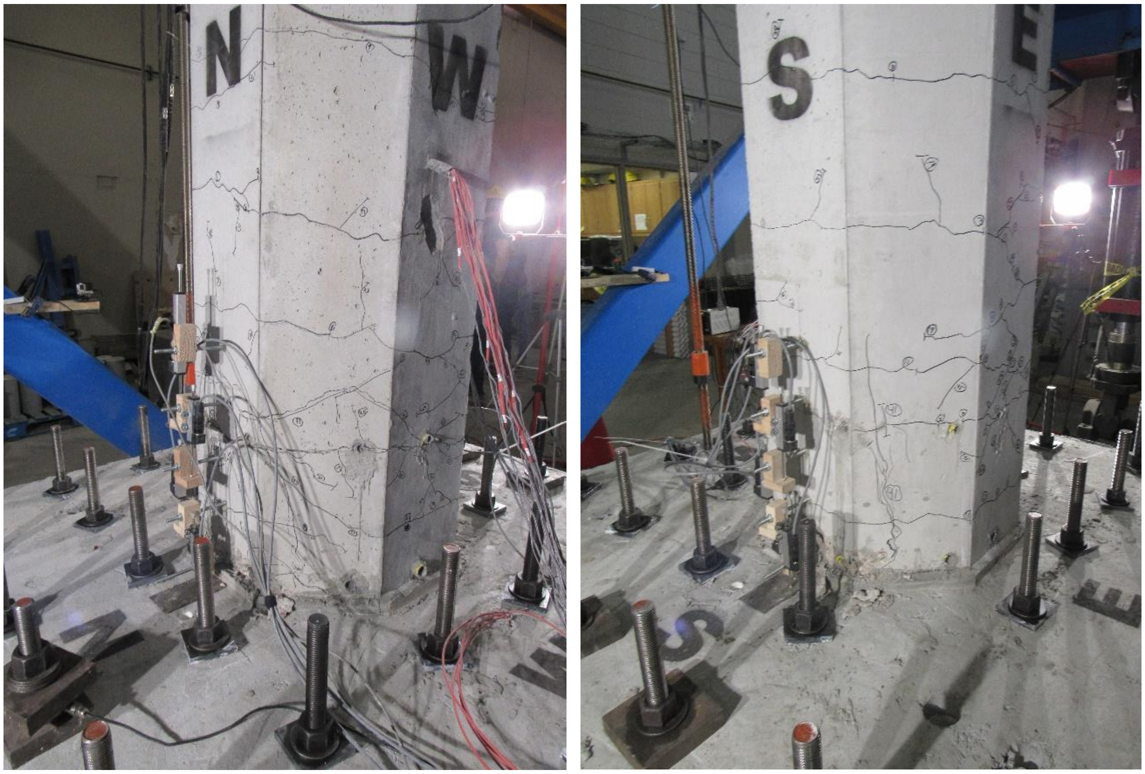

a) North-West Side b) South-East Side

Figure 3.97. PGS Column Plastic Hinge Damage, Second Push of 3.00% Drift Cycle

a) North-West Side b) South-East Side

Figure 3.98. PGS Column Plastic Hinge Damage, Second Pull of 3.00% Drift Cycle

a) North-West Side b) South-East Side

Figure 3.99. PGS Column Plastic Hinge Damage, Second Push of 4.00% Drift Cycle

a) North-West Side b) South-East Side

Figure 3.100. PGS Column Plastic Hinge Damage, Second Pull of 4.00% Drift Cycle

a) North-West Side b) South-East Side

Figure 3.101. PGS Column Plastic Hinge Damage, Second Push of 5.00% Drift Cycle

a) North-West Side b) South-East Side

Figure 3.102. PGS Column Plastic Hinge Damage, Second Pull of 5.00% Drift Cycle

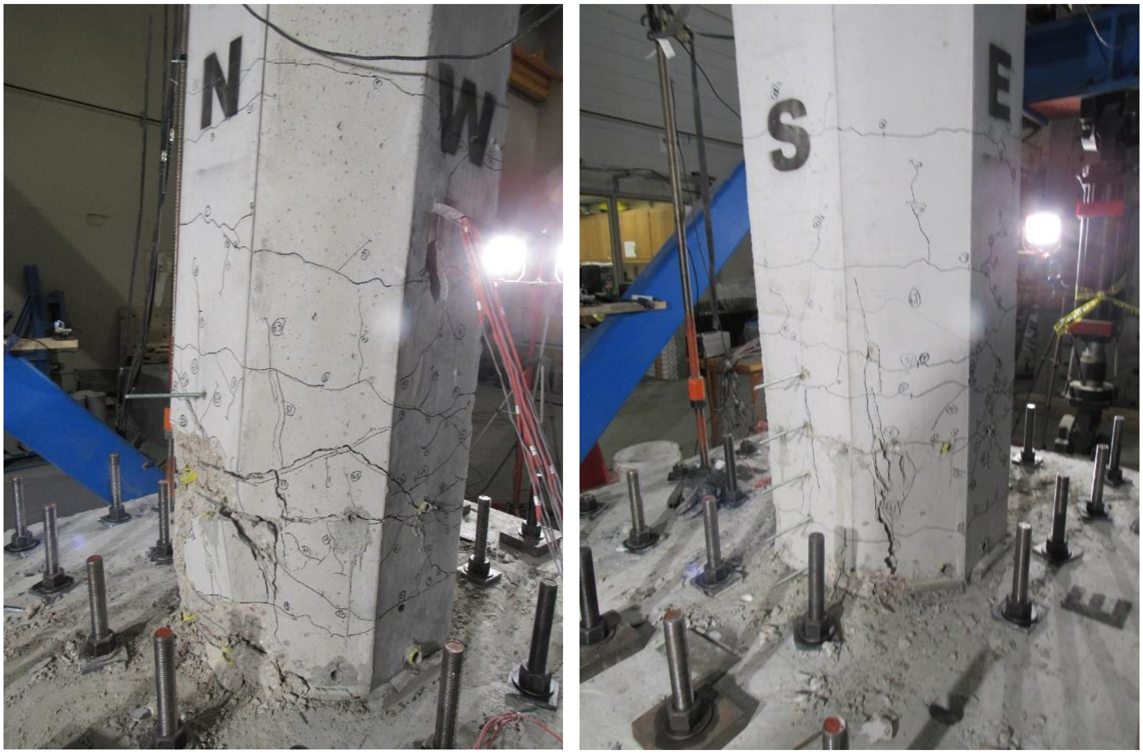

a) North-West Side b) South-East Side

Figure 3.103. PGS Column Plastic Hinge Damage, Second Push of 6.00% Drift Cycle

a) North-West Side b) South-East Side

Figure 3.104. PGS Column Plastic Hinge Damage, Second Pull of 6.00% Drift Cycle

a) North-West Side b) South-East Side

Figure 3.105. PGS Column Plastic Hinge Damage, Second Push of 7.00% Drift Cycle

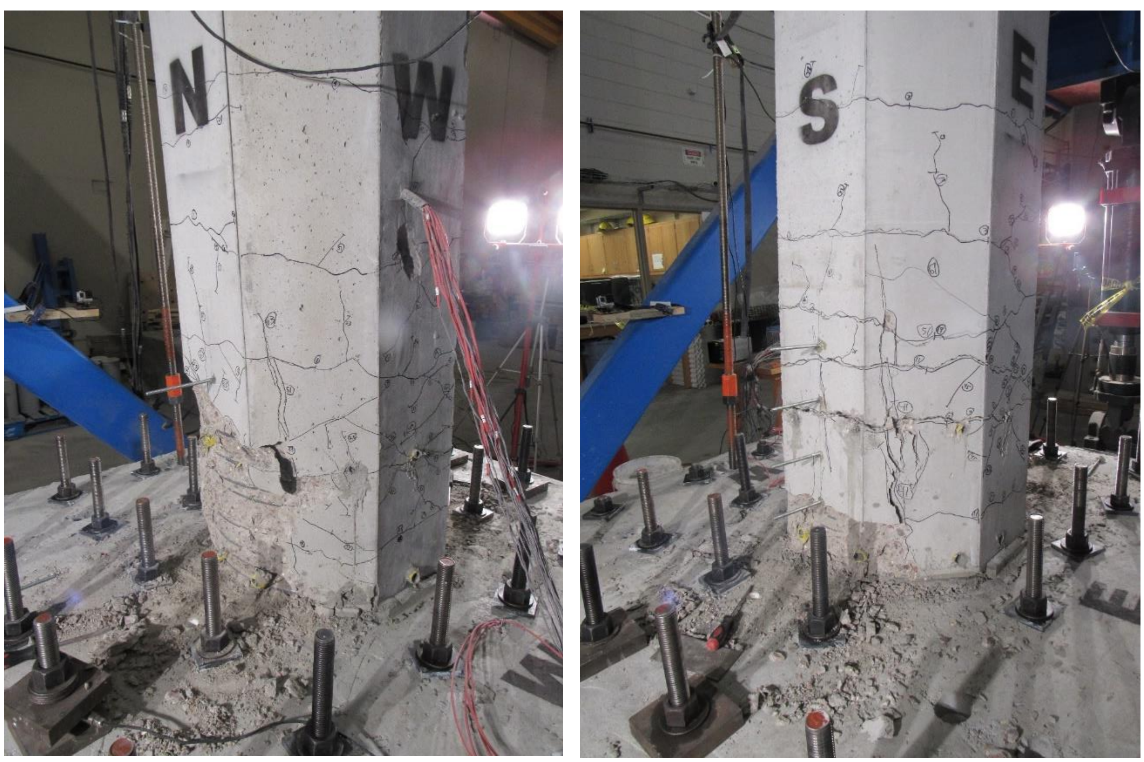

a) North-West Side b) South-East Side

Figure 3.106. PGS Column Plastic Hinge Damage, Second Pull of 7.00% Drift Cycle

a) North-West Side b) South-East Side

Figure 3.107. PGS Column Plastic Hinge Damage, Second Push of 8.00% Drift Cycle

a) North-West Side b) South-East Side

Figure 3.108. PGS Column Plastic Hinge Damage, Second Pull of 8.00% Drift Cycle

a) North-West Side b) South-East Side

Figure 3.109. PGS Column Plastic Hinge Damage, First Push of 9.00% Drift Cycle

a) North-West Side b) South-East Side

Figure 3.110. PGS Column Plastic Hinge Damage, First Pull of 9.00% Drift Cycle

3.5.4.2 Force-Displacement Relationship

Figure 3.111 shows the measured lateral force-drift hysteretic and envelope responses of PGS. The envelope is shown until 85% of the base shear capacity. The PGS column exhibited a maximum lateral load of 69.6 kips (310 kN) at 2% drift ratio and exhibited a steady strength degradation afterwards. A significant strength and stiffness degradation was observed after 9% drift ratio due to longitudinal bar rupture at the column base. The column was slightly stronger in the pull direction. The PGS longitudinal bars yielded at 0.66% drift ratio in the push under a lateral load of 48.4 kip (215.3 kN), and at -0.66% drift ratio in the pull direction at a lateral load of -54.0 kip (240.2 kN).

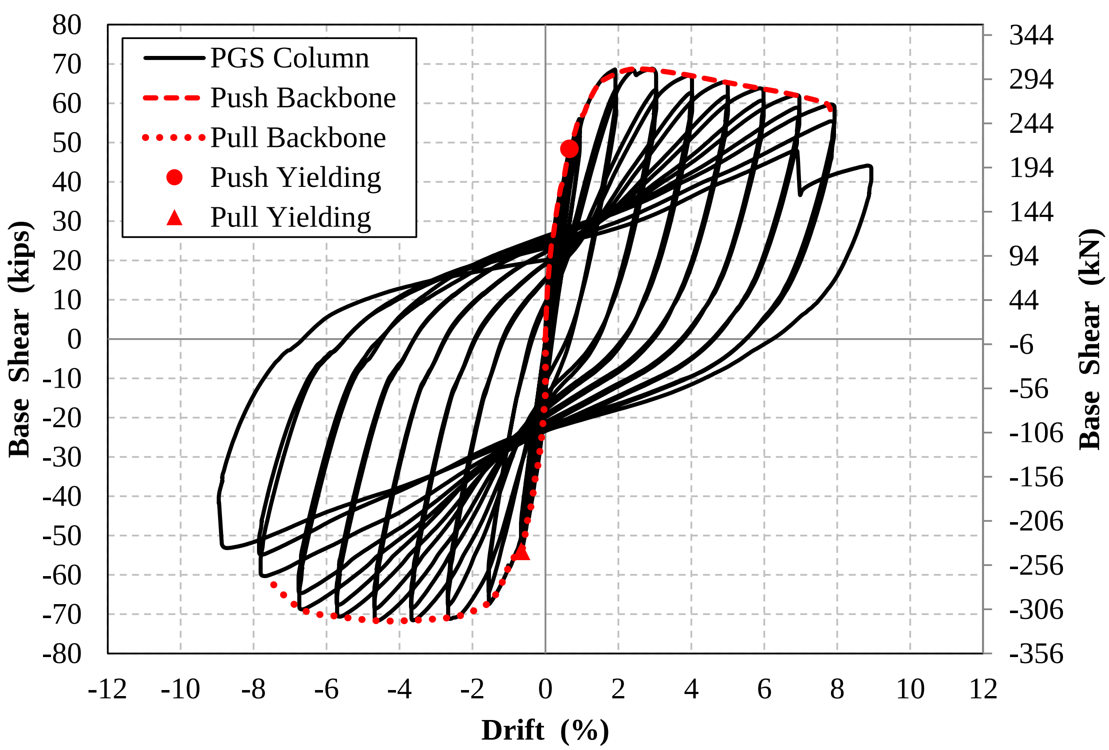

Figure 3.111. PGS Column Force-Drift Hysteretic and Envelope Responses

Figure 3.112 shows the average envelope for the push and pull directions of PGS. The average yield drift ratio was 0.66% occurred at a lateral force of 51.2 kips (227.8 kN). Based on the 15% load drop discussed before as the column failure point, the drift capacity of the PGS column was estimated as 7.71%. Furthermore, Fig. 3.112 shows the idealized curve for the average PGS envelope. The effective yield drift ratio was 0.85% at the effective yield lateral force of 66.1 kip (294.0 kN) resulting in a displacement ductility capacity of 9.08 for the PGS column.

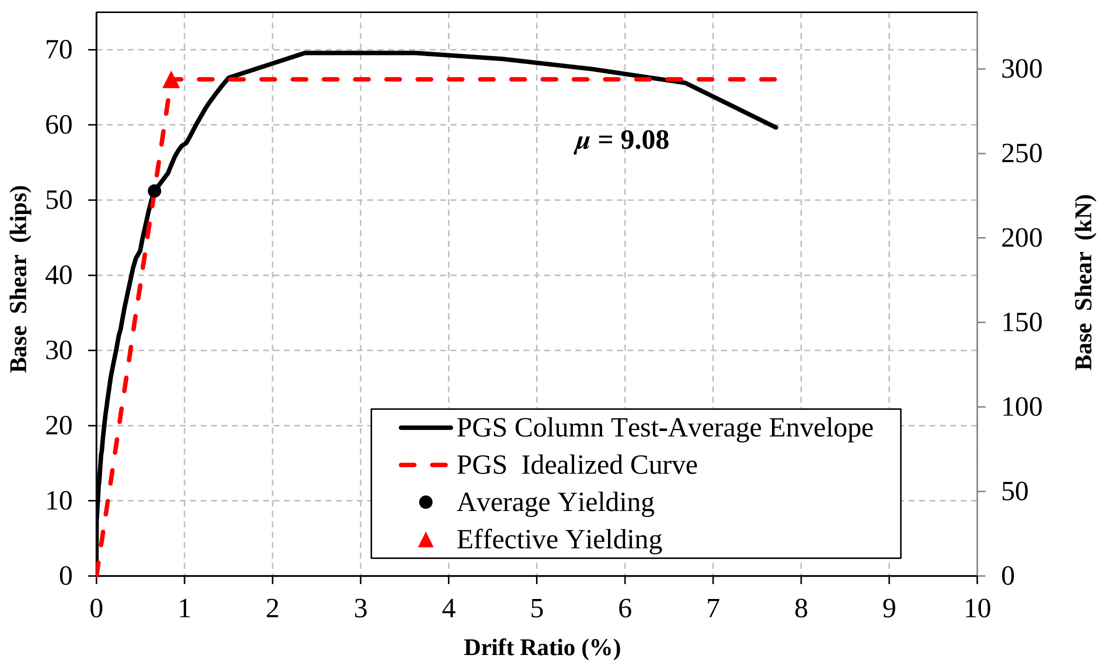

Figure 3.112. PGS Column Average Push/Pull Force-Drift Envelope and Idealized Curve

3.5.4.3 Strain Profile

Seventeen strain gages were installed on the PGS reinforcing steel bars at three levels on the column height. Figures 3.113 to 3.116 show the measured strain profiles of the column for Bars B1, B2, B6, and B7.

The strain profile was uniform prior to the bar yielding. The strain was generally higher closer to the column-footing-interface and decreased along the height of the column once the bars yielded. The bar strains decreased significantly along the height of the column as the height exceeded the column analytical plastic hinge length (approximately 20 in. or 500 mm). It should be noted that the strain profiles for a mechanically spliced column do not follow those of CIP because couplers are stiff and strong and shift the nonlinearity away from the coupler regions. Thus, the column longitudinal bar strains are higher at the coupler ends. This observation will be discussed further in Sec. 3.6.

The strain on the reinforcing hoops was also monitored. The yield strain for the hoops in precast columns was 2.3%. The maximum measured strain in the hoops was 3.1% and occurred in a hoop immediately above the top of the coupler.

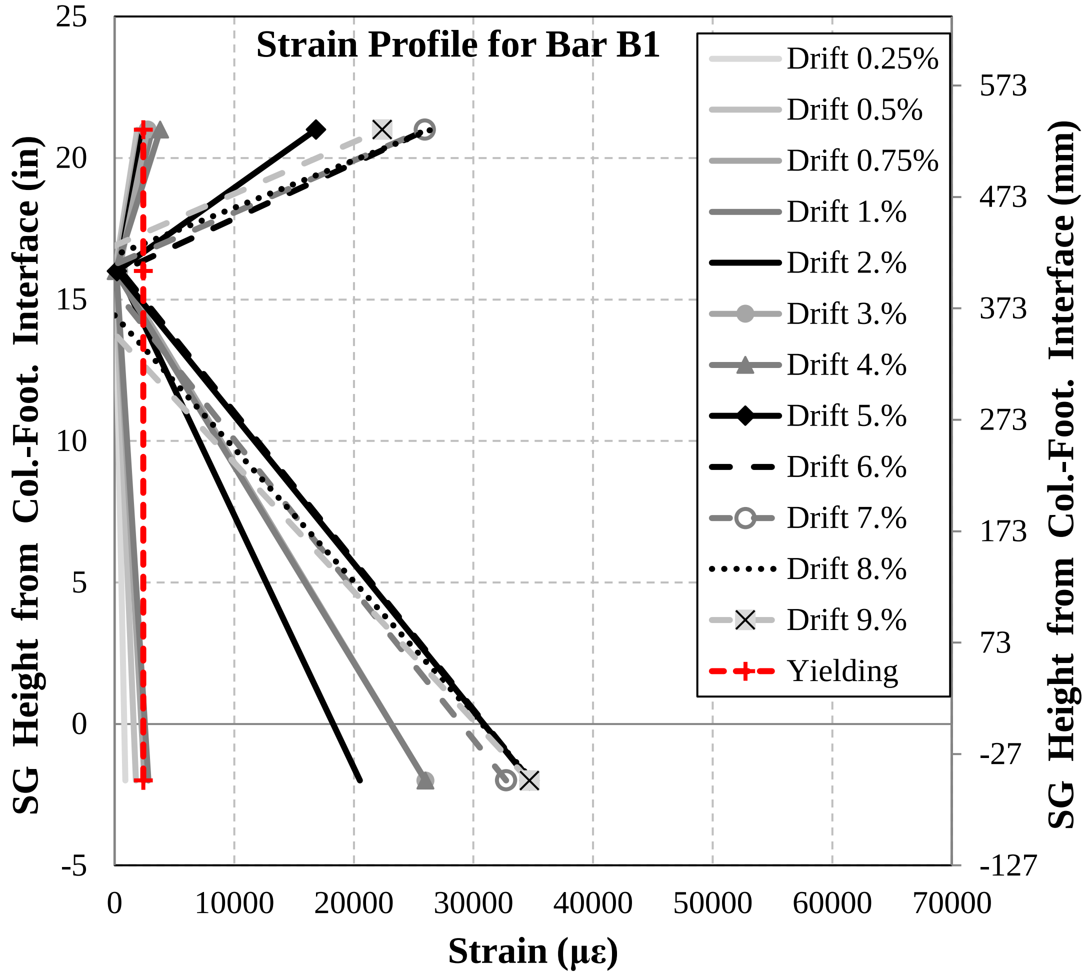

Figure 3.113. Strain Profile for PGS Column Bar B1

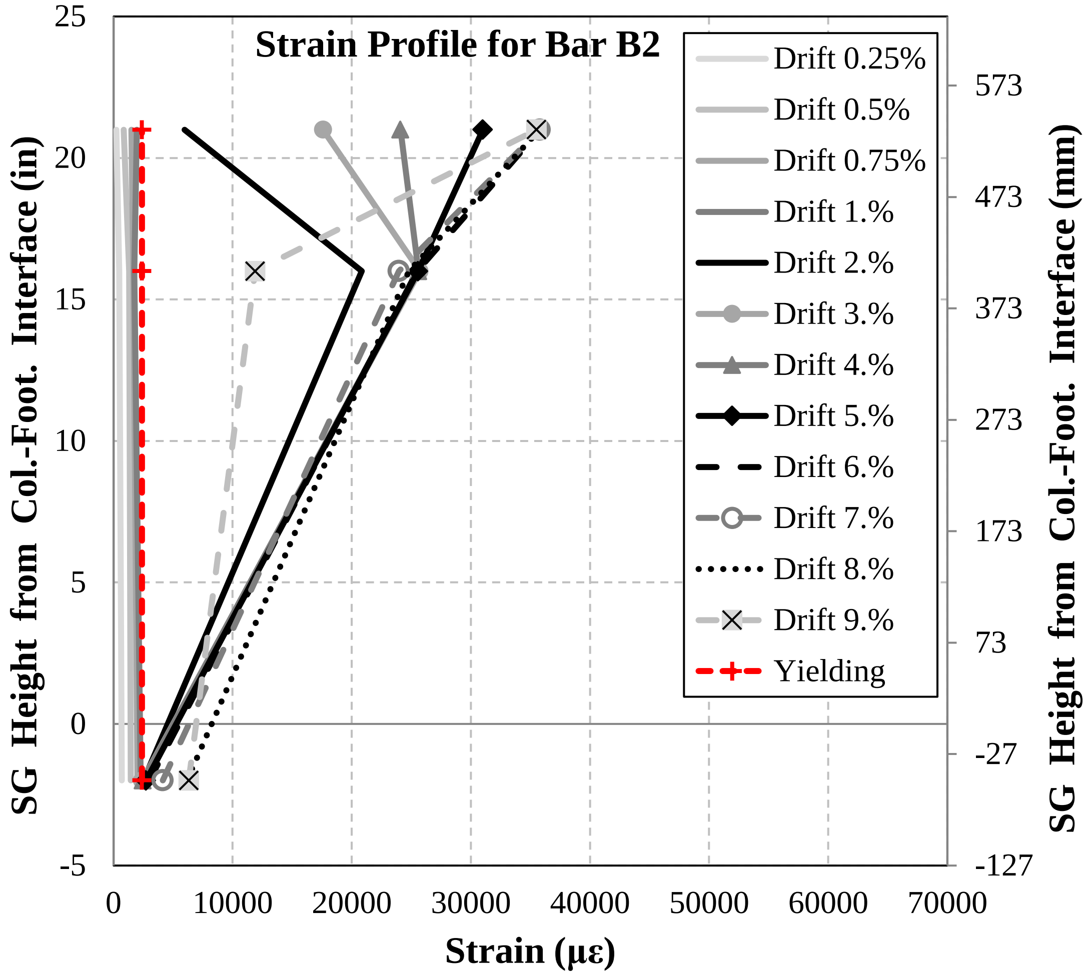

Figure 3.114. Strain Profile for PGS Column Bar B2

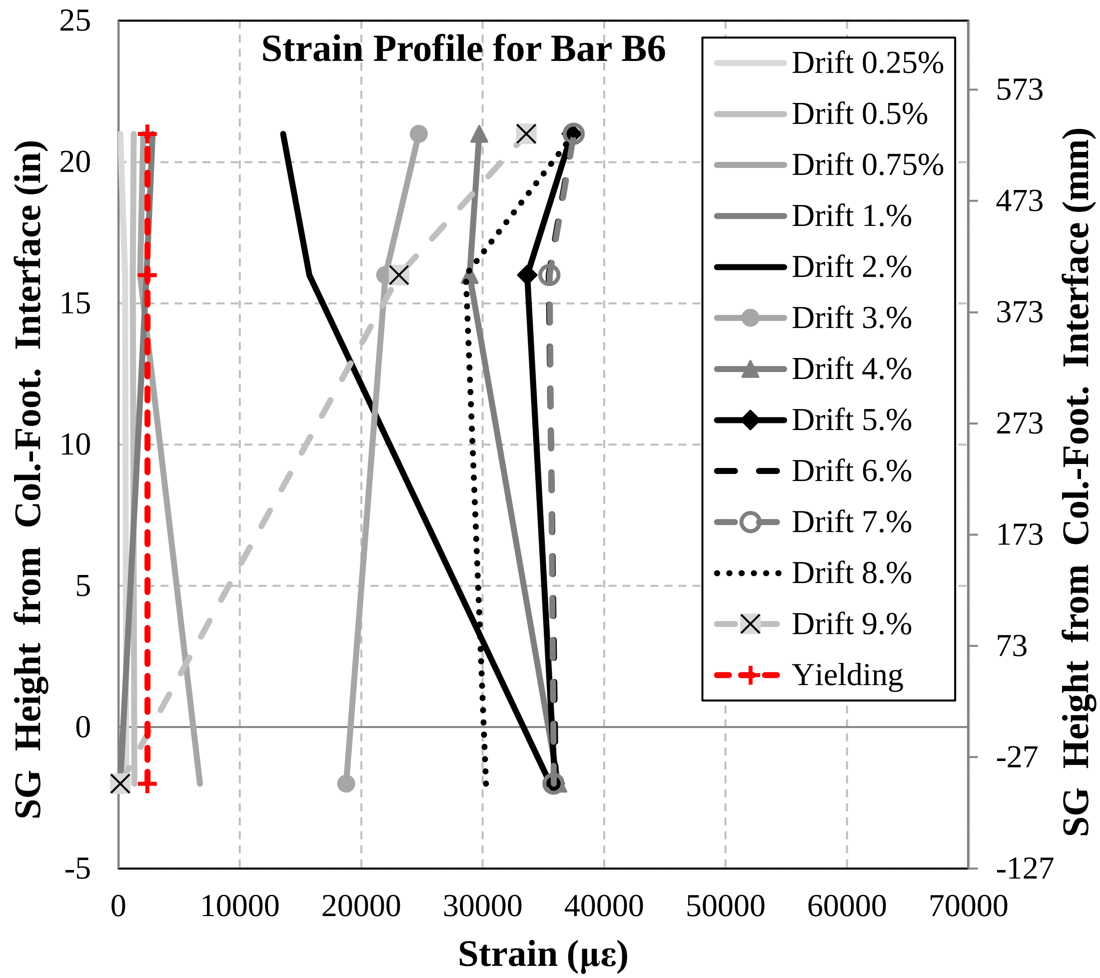

Figure 3.115. Strain Profile for PGS Column Bar B6

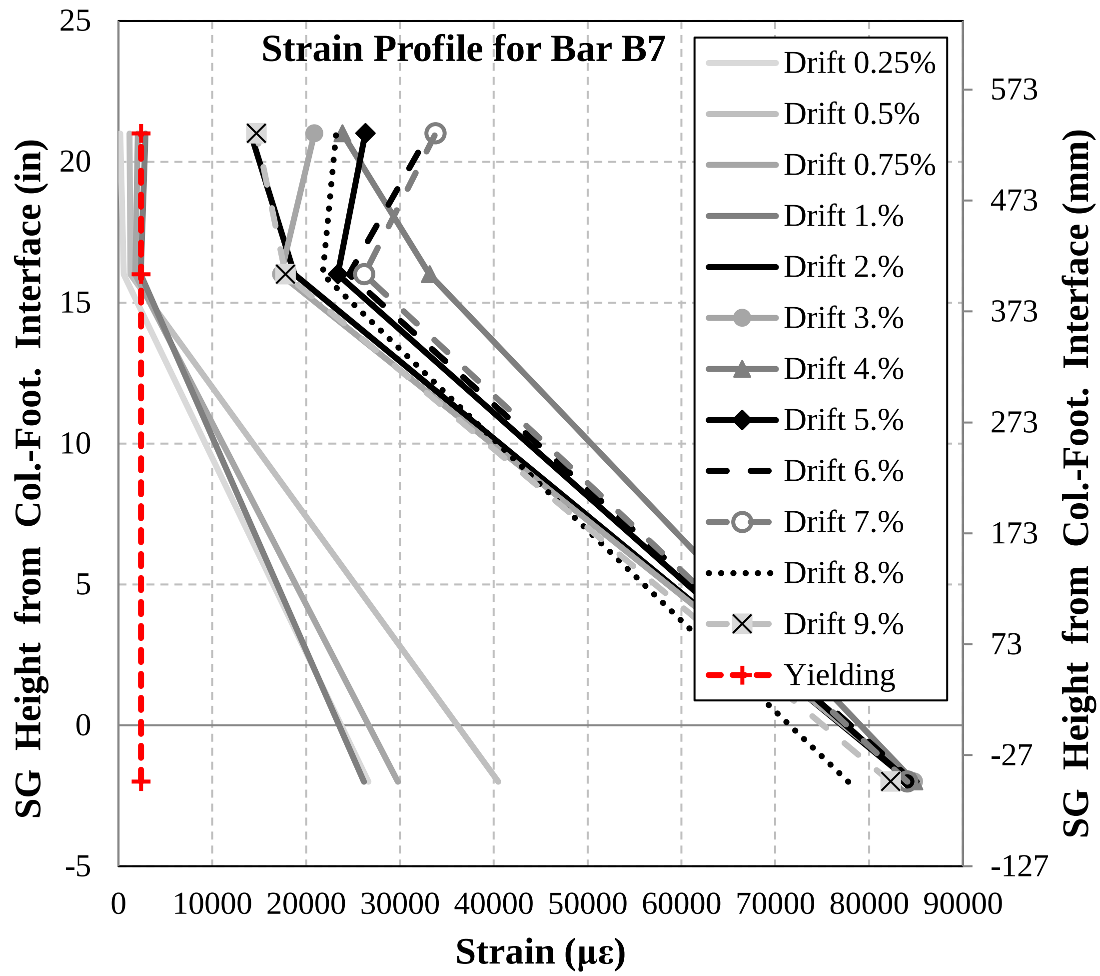

Figure 3.116. Strain Profile for PGS Column Bar B7

3.5.4.4 Measured Rotation and Curvature

Rotations and curvatures were determined in the same manner as CIP. Figure 3.117 shows the measured curvature profile for the PGS column at drift ratios of 0.25% to 4.0%. The highest curvature always occurred at the base due to concentrated concrete cracking and bar-slip near the column-footing interface. The grouted couplers used in PGS increased the column stiffness in the coupler region leading to a shift of nonlinearity outside of the coupler. The figure confirms this observation in which the curvature was

relatively high near the column base, minimal along the coupler region, and high above the coupler levels.

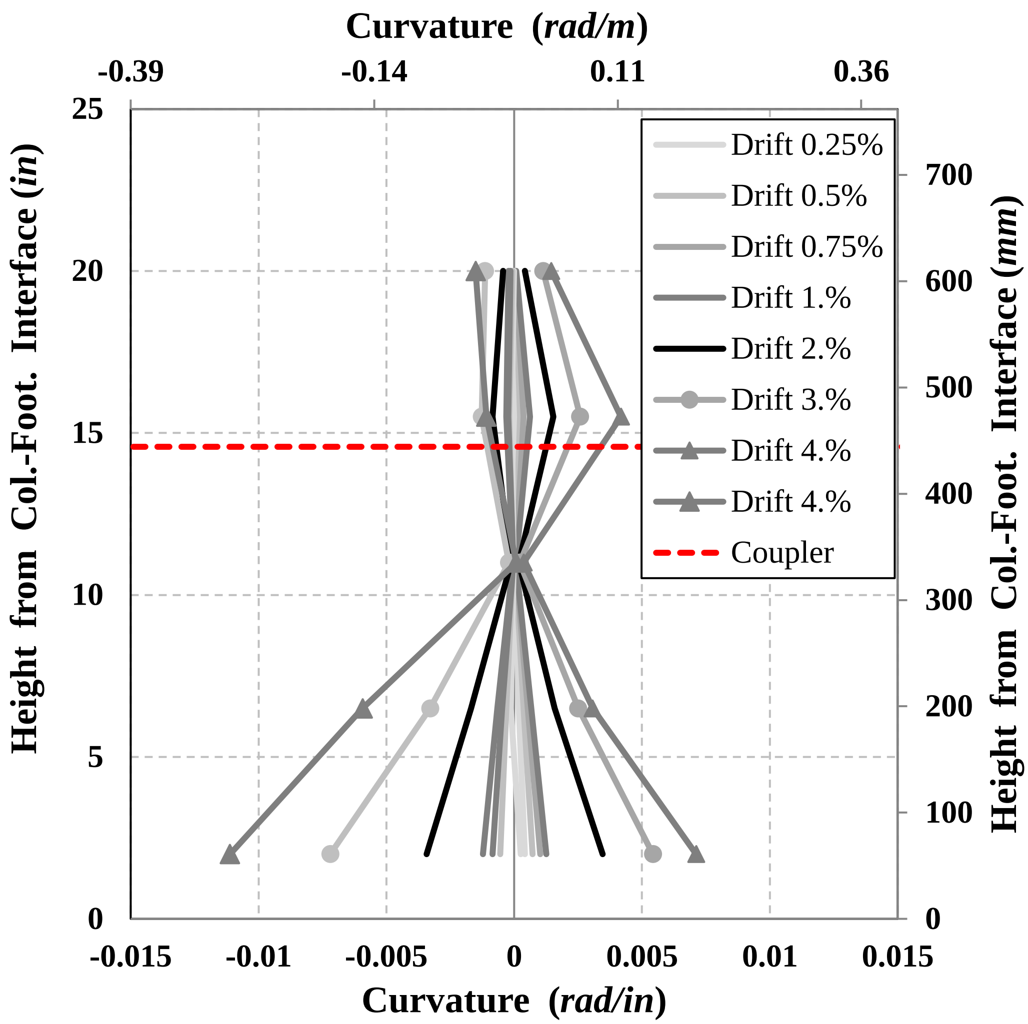

Figure 3.117. Curvature Profile for PGS Column

3.5.4.5 Energy Dissipation

Figure 3.118 shows the measured cumulative energy dissipation of the PGS column at different drift ratios. The dissipated energy is negligible until 1% drift ratio, where bar yielding was minimal. At higher drift ratios, the hysteretic loops began to widen which led to a higher dissipated energy. PGS dissipated 5,744 kip-in. (653 kN-m) of energy prior to the failure.

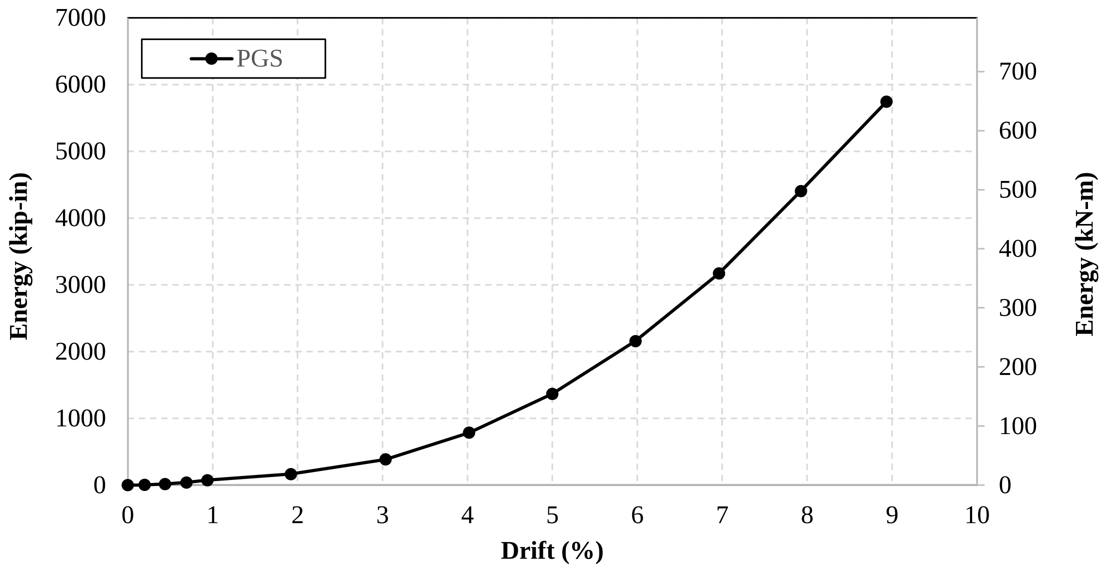

Figure 3.118. Energy Dissipation for PGS Column

3.5.5 PHD Column Results

The seismic performance of the precast column using the Dextra Groutec-S grouted-threaded hybrid coupler, PHD, is presented in this section.

3.5.5.1 Observed Damage

The PHD column followed the same testing procedure as the CIP column. Table 3.9 provides damage observed for each push or pull loads for the PHD column. show the PHD plastic hinge damage in the second cycle of push or push for each drift level.

Flexural cracks were occurred in the first cycle of 0.25% drift ratio (Fig. 3.119 & 3.120). Shear cracks were first observed in the first cycle of 0.5% drift ratio (Fig. 3.121 & 3.122). The first yielding in occurred in bar B1 at 0.58% drift in the first push run of the 0.75% drift cycle under a lateral load of 45.9 kips (204.3 kN) (Fig. 3.123). Concrete spalling began to occur on both the North and South faces of the column during the 3% drift cycles (Fig. 3.129 & 3.130). Finally, longitudinal bars pulled out of the couplers at

the 4% drift cycle leading to a major strength reduction and the end of the test (Figure 3.131 & 3.132).

The PHD Column mode of failure was longitudinal bar longitudinal bar pullout during the 4% drift cycles.

Table 3.9. Summary of Damage in PHD

Drift Ratio, %	Observed Damage
+0.25	• Minor flexural cracks • Flexural cracks at top of coupler
-0.25	• Minor flexural cracks • Flexural cracks at top of coupler
+0.50	• Flexural and inclined cracks
-0.50	• Flexural and inclined cracks • Cracking at column base
+0.75	• Flexural Cracks • Bar Yielding
-0.75	• Flexural Cracks • Bar Yielding
+1.00	• Flexural Cracks • Vertical cracks
-1.00	• Flexural Cracks
+2.00	• Vertical, flexural, and inclined cracks
-2.00	• Vertical, flexural, and inclined cracks
+3.00	• Flexural cracks • Initiation of spalling on South face of column
-3.00	• Flexural cracks • Initiation of spalling on North face of column
+4.00	• Longitudinal reinforcement pullout from coupler on North Face
-4.00	• Longitudinal reinforcement pullout from coupler on South Face

Note: Positive drifts were based on displacements away from the reaction blocks (North to South)

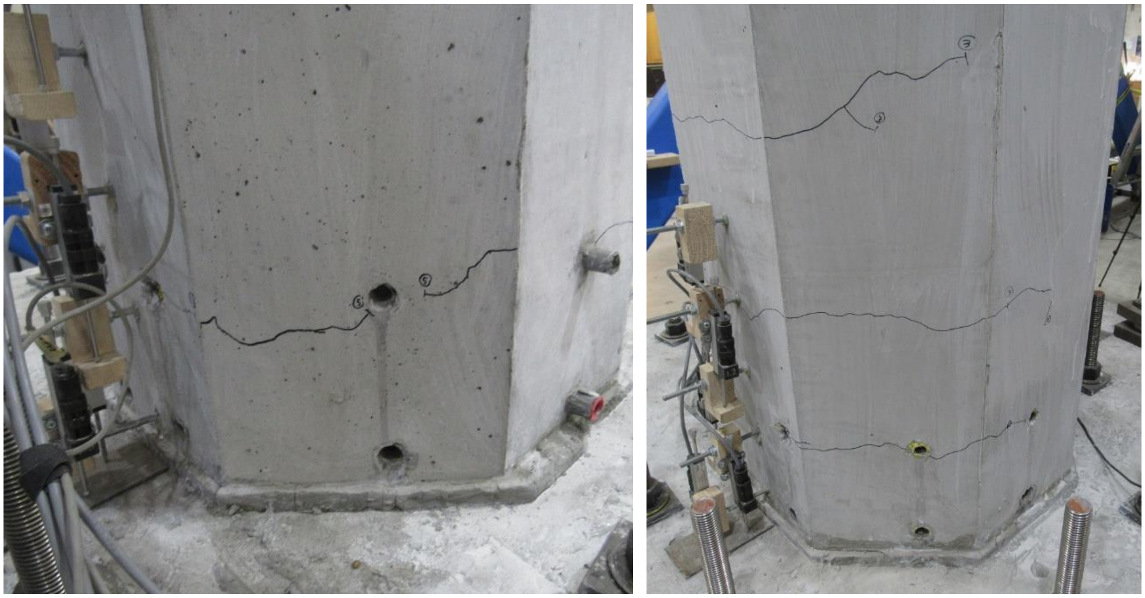

a) North-West Side b) South-East Side

Figure 3.119. PHD Column Plastic Hinge Damage, Second Push of 0.25% Drift Cycle

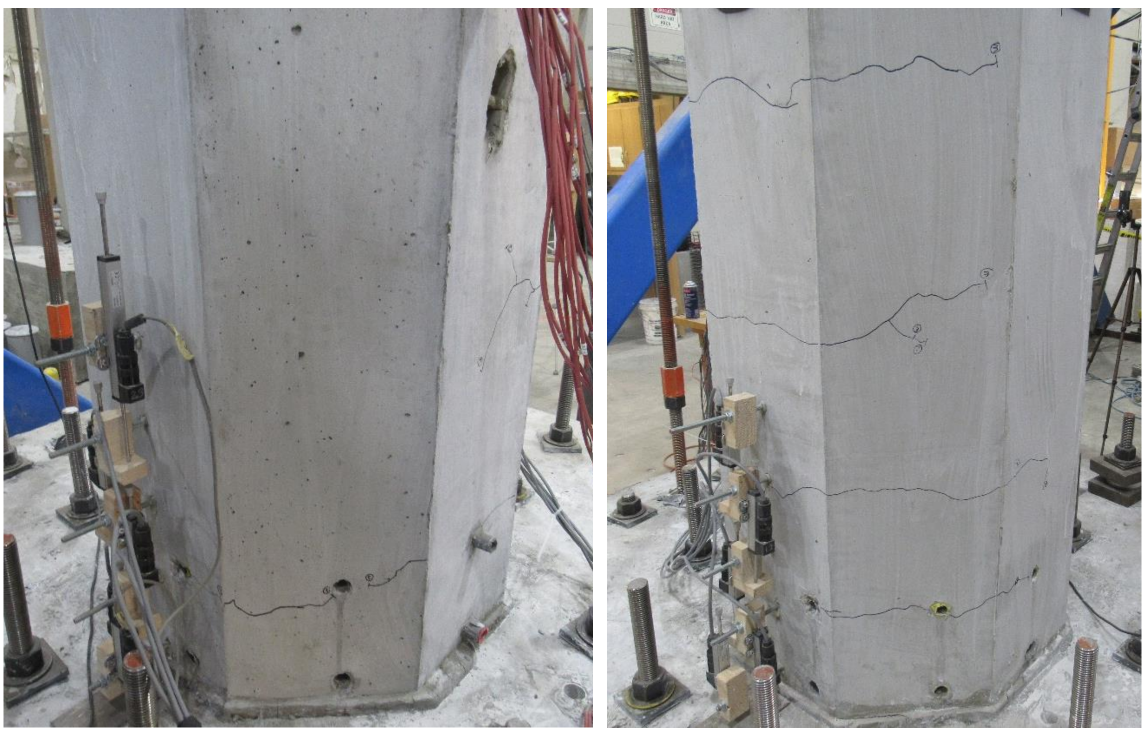

a) North-West Side b) South-East Side

Figure 3.120. PHD Column Plastic Hinge Damage, Second Pull of 0.25% Drift Cycle

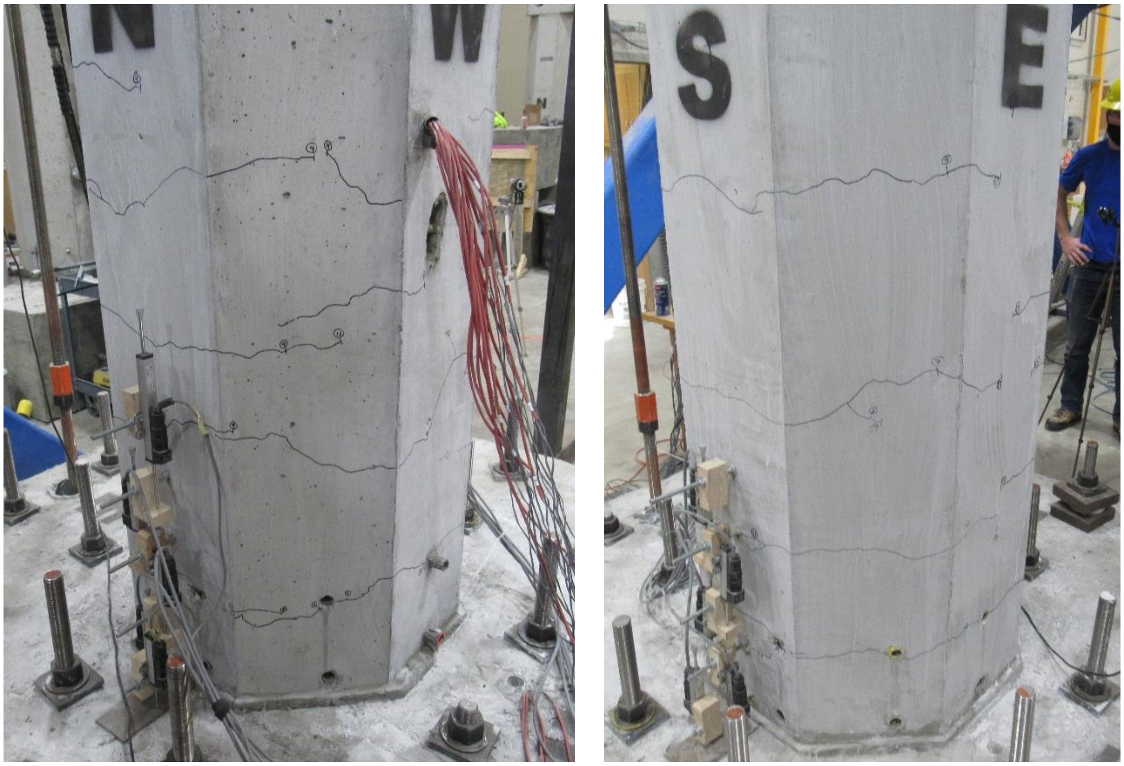

a) North-West Side b) South-East Side

Figure 3.121. PHD Column Plastic Hinge Damage, Second Push of 0.50% Drift Cycle

a) North-West Side b) South-East Side

Figure 3.122. PHD Column Plastic Hinge Damage, Second Pull of 0.50% Drift Cycle

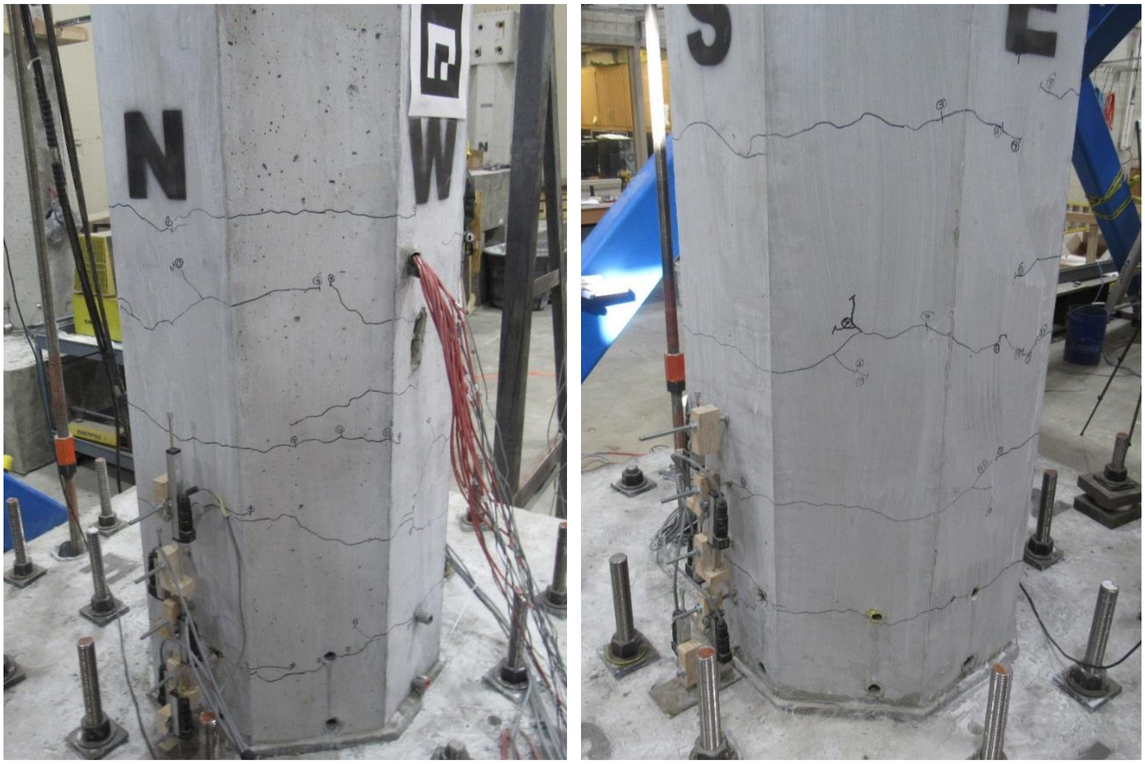

a) North-West Side b) South-East Side

Figure 3.123. PHD Column Plastic Hinge Damage, Second Push of 0.75% Drift Cycle

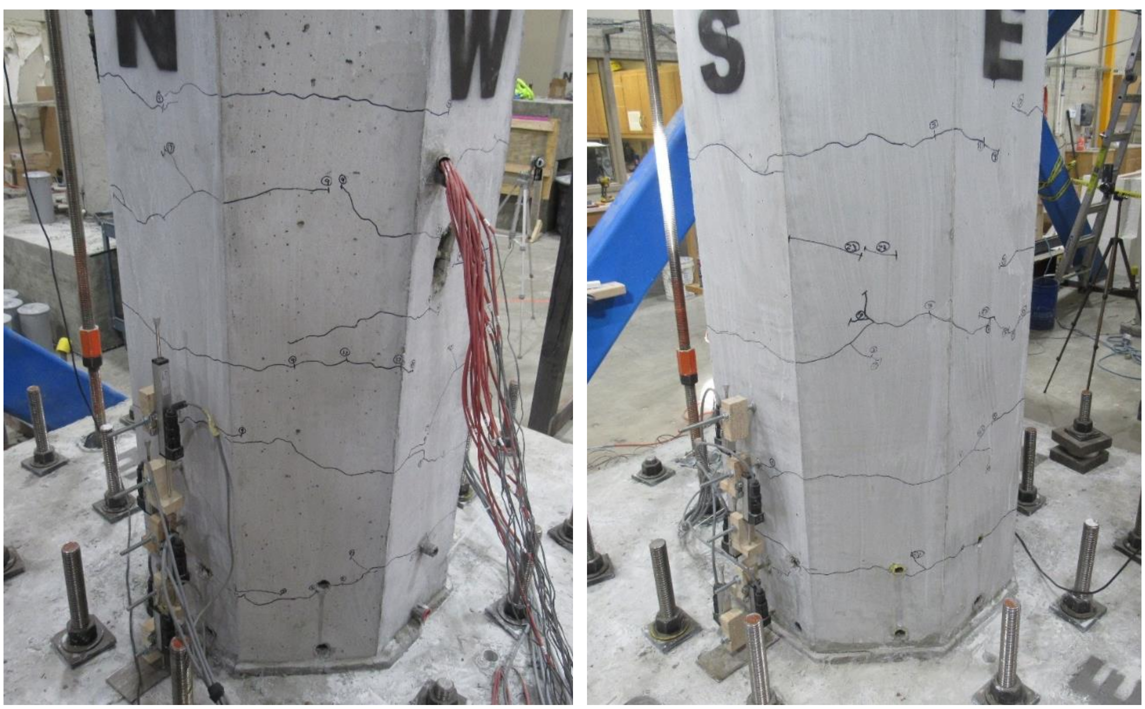

a) North-West Side b) South-East Side

Figure 3.124. PHD Column Plastic Hinge Damage, Second Pull of 0.75% Drift Cycle

a) North-West Side b) South-East Side

Figure 3.125. PHD Column Plastic Hinge Damage, Second Push of 1.00% Drift Cycle

a) North-West Side b) South-East Side

Figure 3.126. PHD Column Plastic Hinge Damage, Second Pull of 1.00% Drift Cycle

a) North-West Side b) South-East Side

Figure 3.127. PHD Column Plastic Hinge Damage, Second Push of 2.00% Drift Cycle

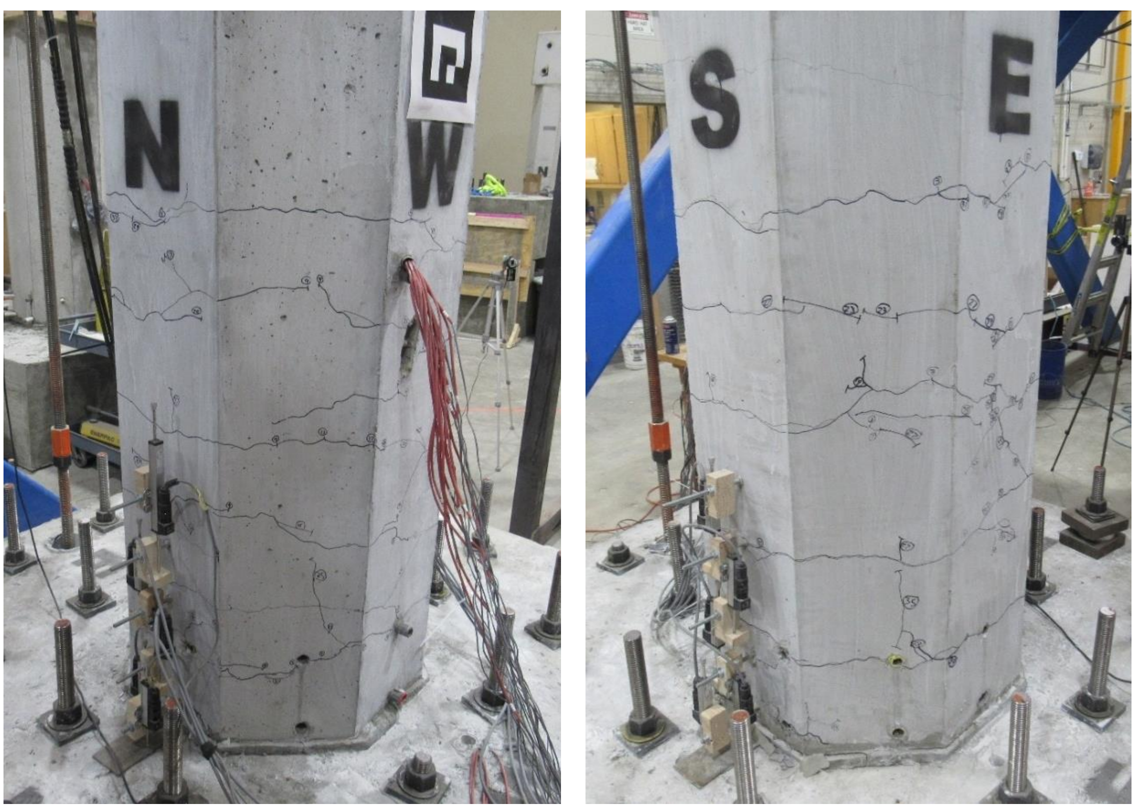

a) North-West Side b) South-East Side

Figure 3.128. PHD Column Plastic Hinge Damage, Second Pull of 2.00% Drift Cycle

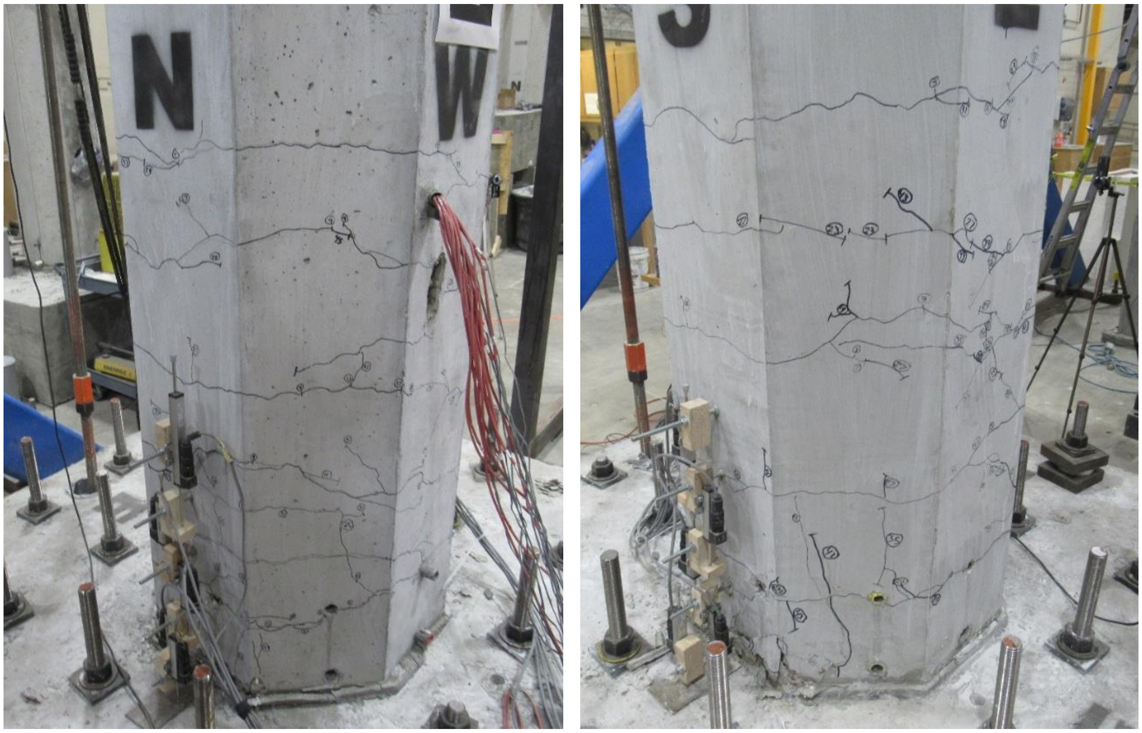

a) North-West Side b) South-East Side

Figure 3.129. PHD Column Plastic Hinge Damage, Second Push of 3.00% Drift Cycle

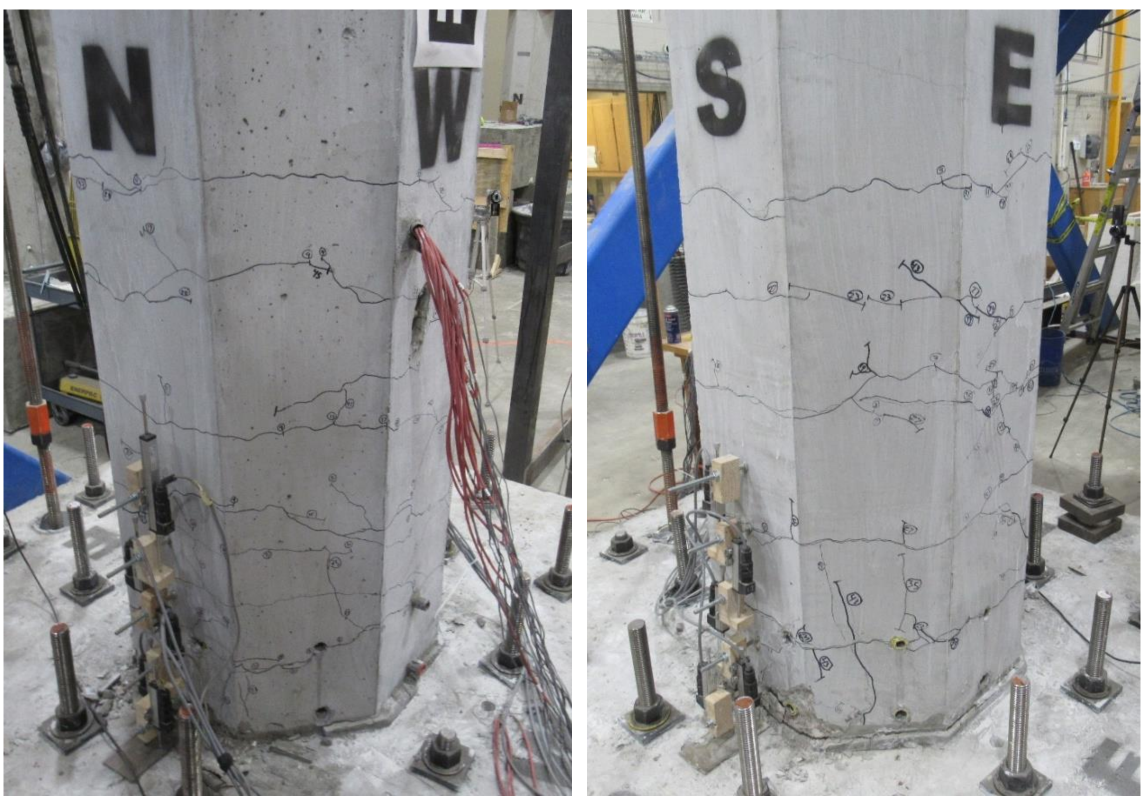

a) North-West Side b) South-East Side

Figure 3.130. PHD Column Plastic Hinge Damage, Second Pull of 3.00% Drift Cycle

a) North-West Side b) South-East Side

Figure 3.131. PHD Column Plastic Hinge Damage, Second Push of 4.00% Drift Cycle

a) North-West Side b) South-East Side

Figure 3.132. PHD Column Plastic Hinge Damage, Second Pull of 4.00% Drift Cycle

3.5.5.2 Force-Displacement Relationship

Figure 3.133 shows the measured lateral force-drift hysteretic and envelope responses of PHD. The envelope is shown until 85% of the base shear capacity. The PHD column exhibited a maximum lateral load of 71.5 kips (318 kN) at 3% drift ratio and exhibited a rapid strength degradation afterwards. A significant strength and stiffness degradation was observed due to bar pullout from the coupler base. The column was slightly stronger in the push direction. The PHD longitudinal bars yielded at 0.54% drift ratio in the push under a lateral load of 41.4 kip (184.2 kN), and at -0.78% drift ratio in the pull direction at a lateral load of -52.8 kip (234.9 kN).

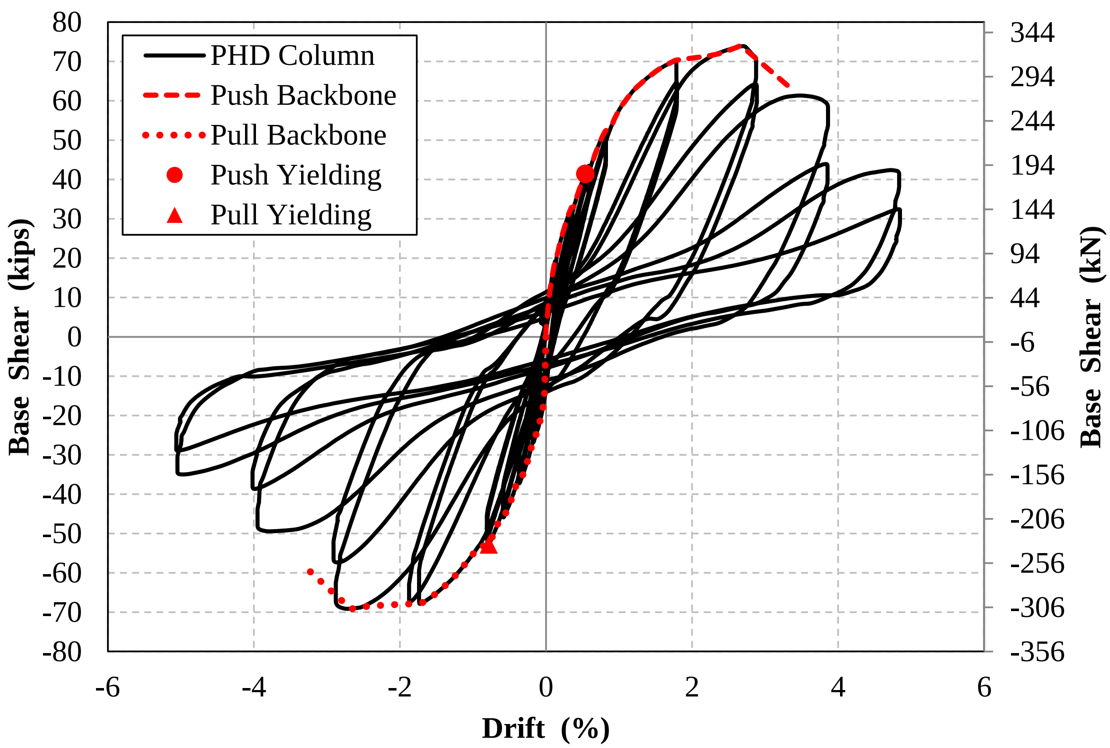

Figure 3.133. PHD Column Force-Drift Hysteretic and Envelope Responses

Figure 3.134 shows the average envelope for the push and pull directions of PHD. The average yield drift ratio was 0.66% occurred at a lateral force of 47.1 kips (209.5 kN). Based on the 15% load drop discussed before as the column failure point, the drift

capacity of the PHD column was estimated as 3.33%. Furthermore, Fig. 3.134 shows the idealized curve for the average PHD envelope. The effective yield drift ratio was 0.93% at the effective yield lateral force of 65.2 kip (290.0 kN) resulting in a displacement ductility capacity of 3.60 for the PHD column.

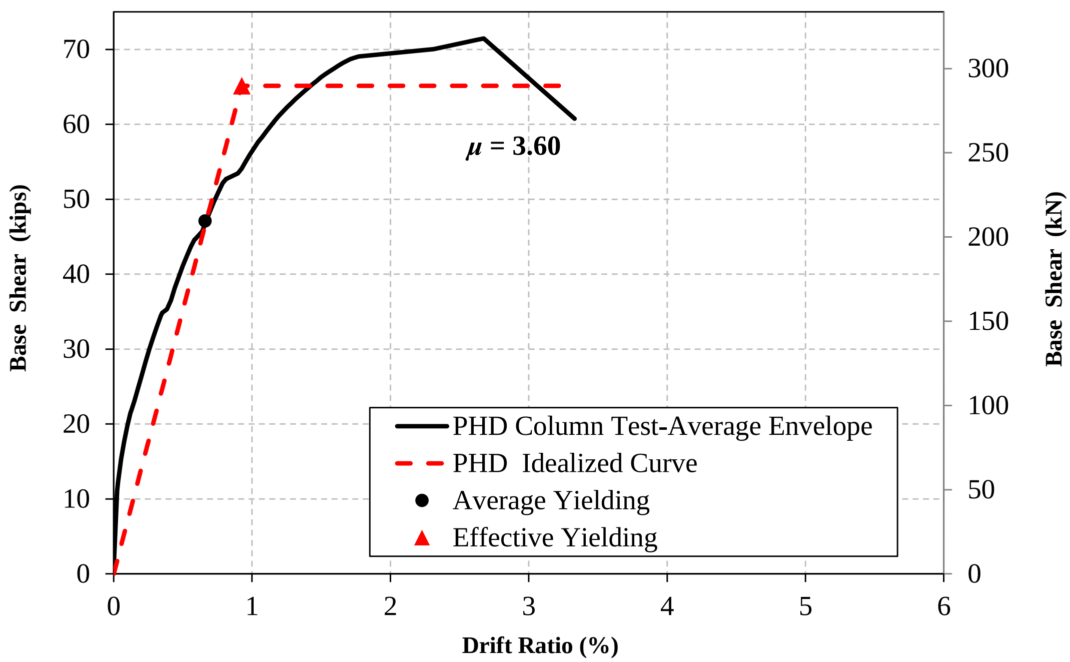

Figure 3.134. PHD Column Average Push/Pull Force-Drift Envelope and Idealized Curve

3.5.5.3 Strain Profile

Twenty-three strain gages were installed on the PHD reinforcing steel bars at three levels on the column height. Figures 3.135 to 3.138 show the measured strain profiles of the column for Bars B1, B2, B6, and B7.

The strain profile was uniform prior to the bar yielding. The strain was generally higher closer to the column-footing-interface and decreased along the height of the column once the bars yielded. The bar strains decreased significantly along the height of the column as the height exceeded the column analytical plastic hinge length

(approximately 20 in. or 500 mm). It should be noted that the strain profiles for a mechanically spliced column do not follow those of CIP because couplers are stiff and strong and shift the nonlinearity away from the coupler regions. Thus, the column longitudinal bar strains are higher at the coupler ends. This observation will be discussed further in Sec. 3.6.

The strain on the reinforcing hoops was also monitored. The yield strain for the hoops in precast columns was 2.3%. The maximum measured strain in the hoops was 0.4% and occurred in a hoop immediately above the top of the coupler.

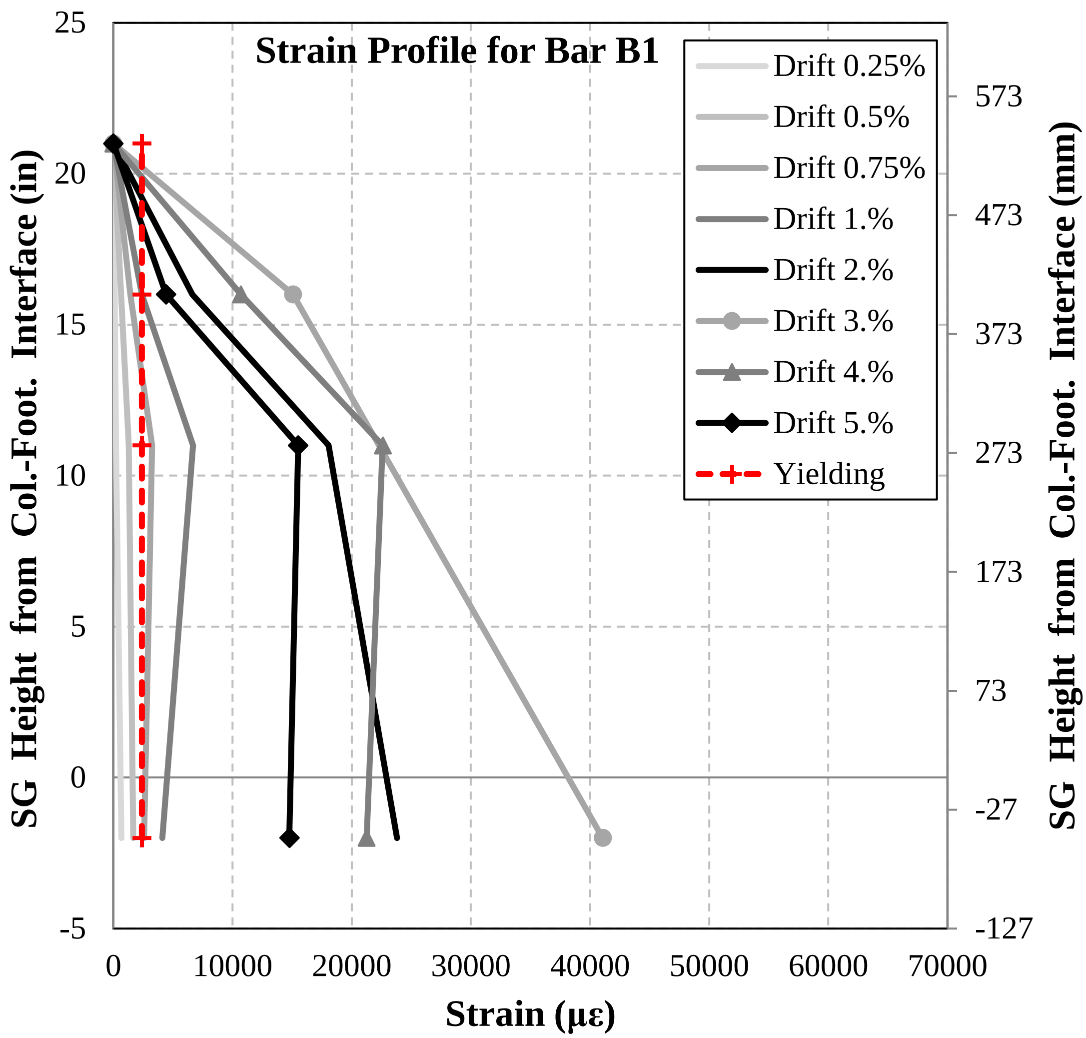

Figure 3.135. Strain Profile for PHD Column Bar B1

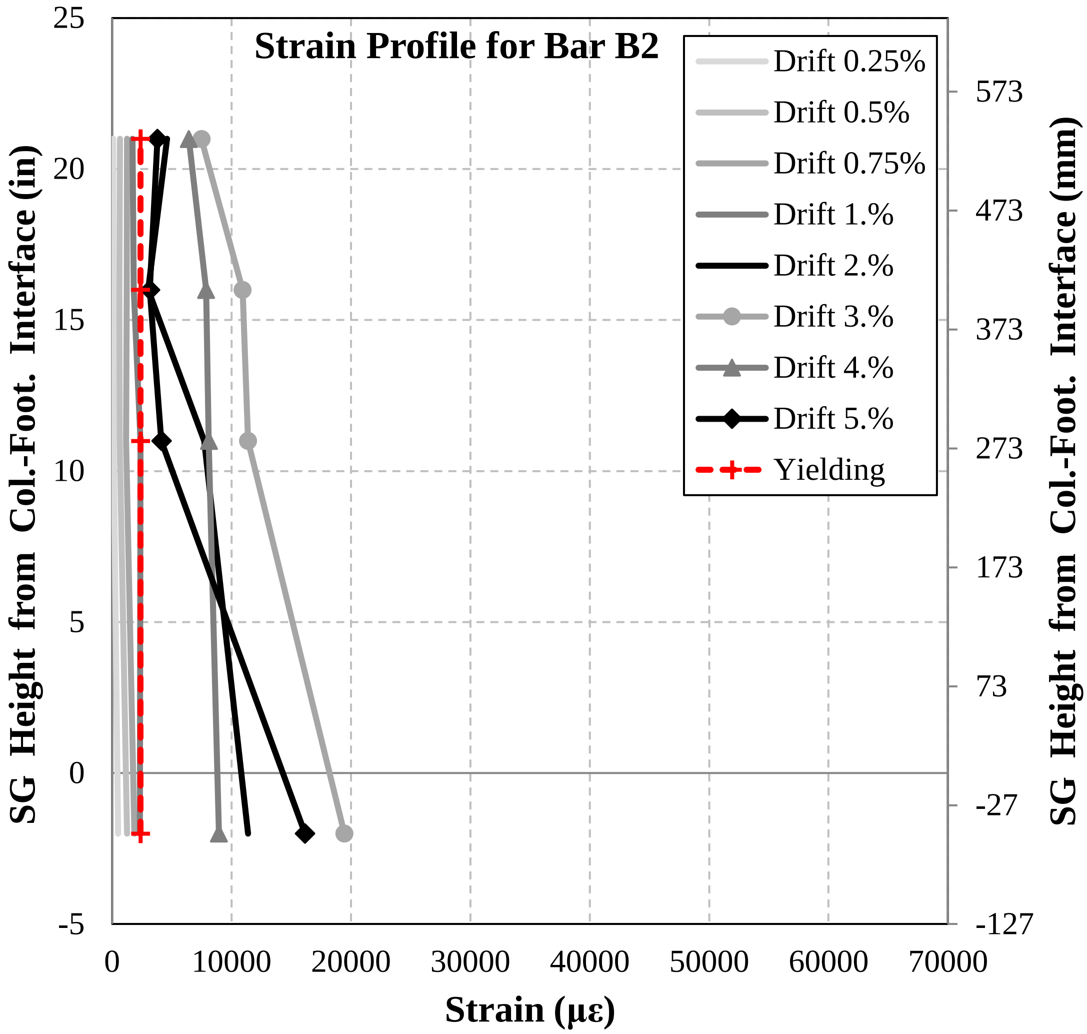

Figure 3.136. Strain Profile for PHD Column Bar B2

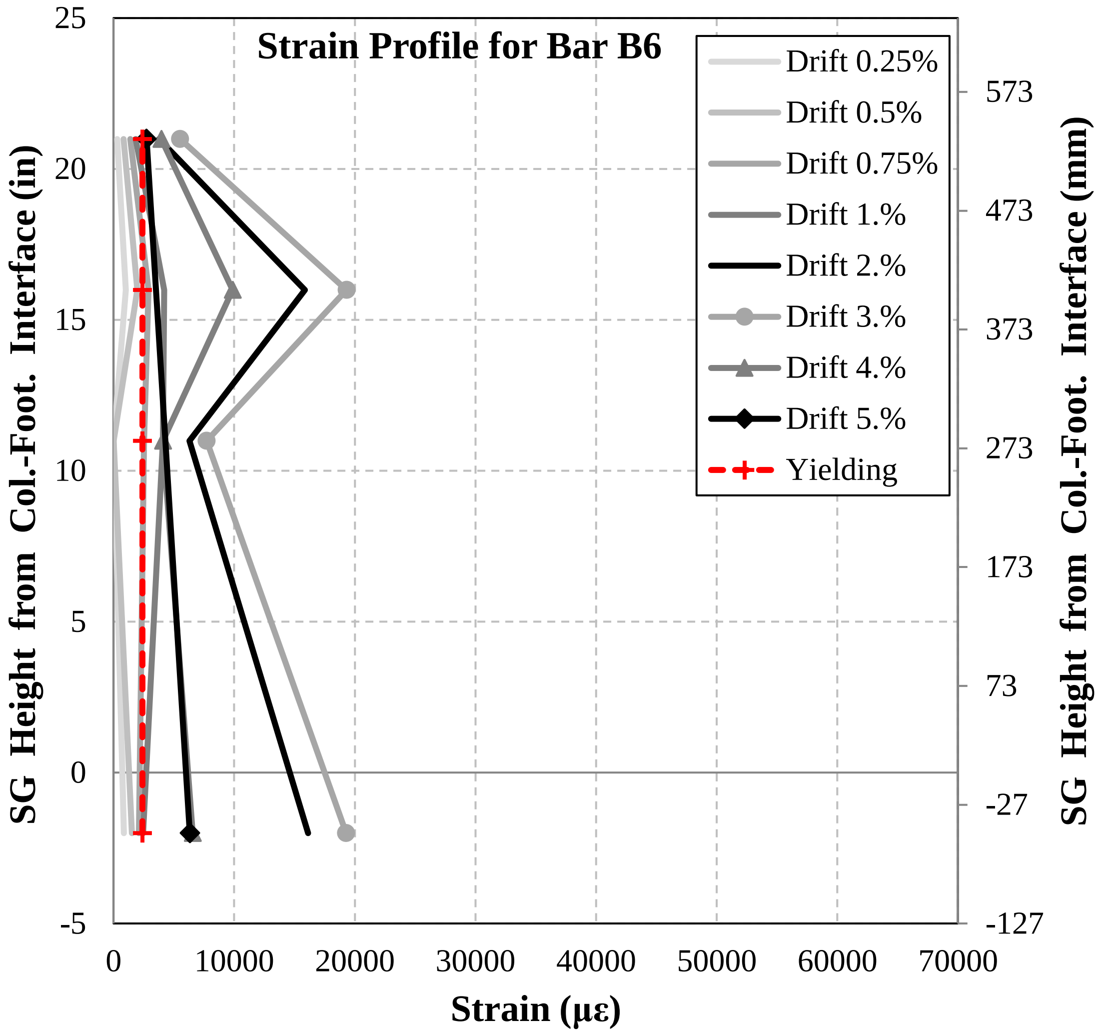

Figure 3.137. Strain Profile for PHD Column Bar B6

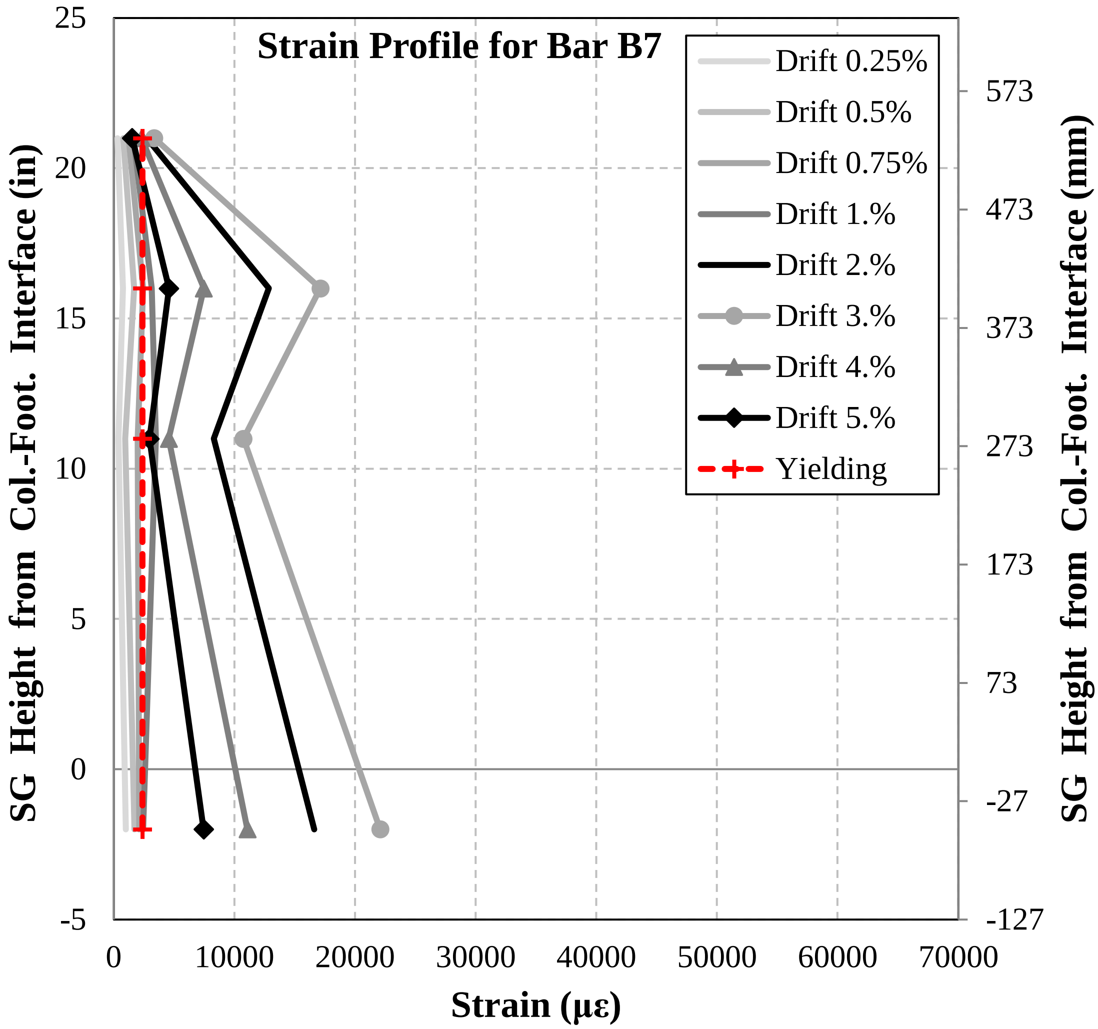

Figure 3.138. Strain Profile for PHD Column Bar B7

3.5.5.4 Measured Rotation and Curvature

Rotations and curvatures were determined in the same manner as CIP. Figure 3.139 shows the measured curvature profile for the PHD column at drift ratios of 0.25% to 4.0%. The highest curvature always occurred at the base due to concentrated concrete cracking and bar-slip near the column-footing interface. The grouted couplers used in PHD increased the column stiffness in the coupler region leading to a shift of nonlinearity outside of the coupler. The figure confirms this observation in which the curvature was

relatively high near the column base, minimal along the coupler region, and high above the coupler levels.

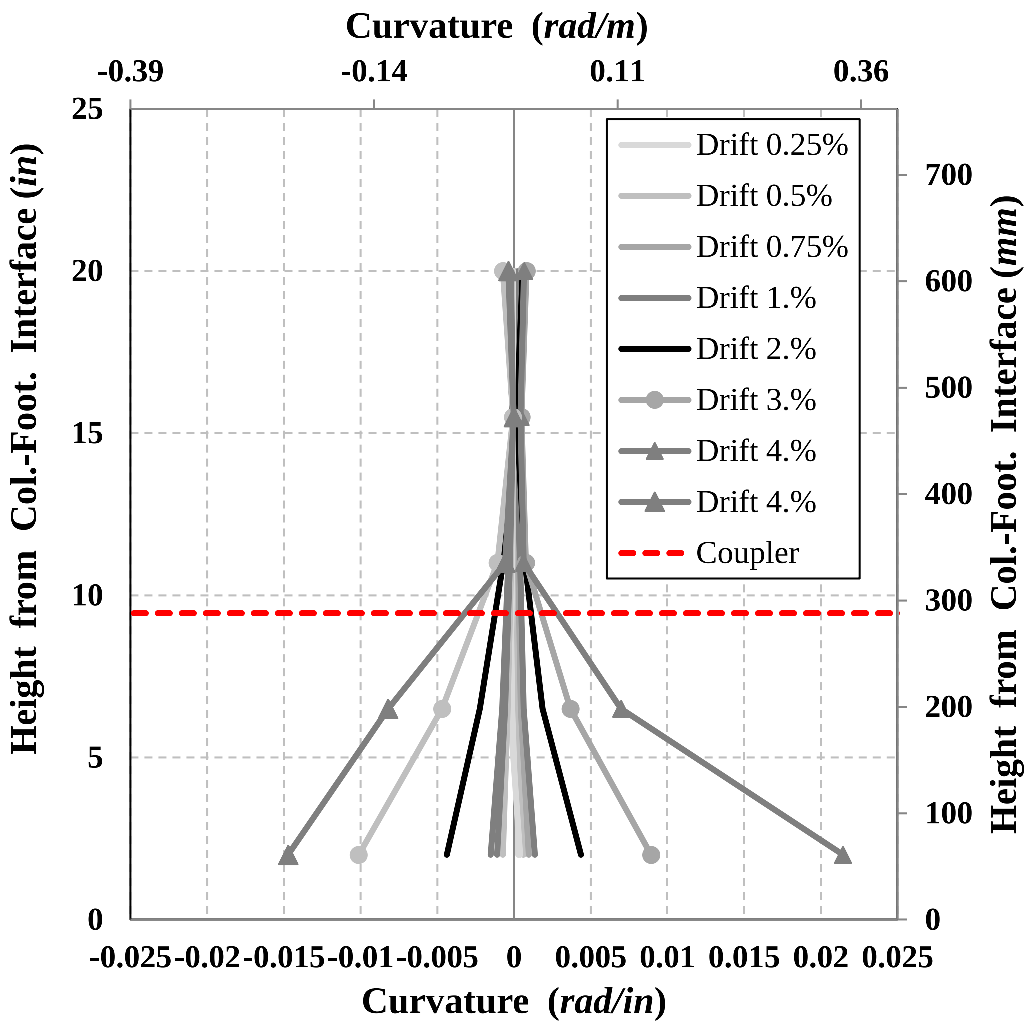

Figure 3.139. Curvature Profile for PHD Column

3.5.5.5 Energy Dissipation

Figure 3.140 shows the measured cumulative energy dissipation of the PHD column at different drift ratios. The dissipated energy is negligible until 1% drift ratio, where bar yielding was minimal. At higher drift ratios, the hysteretic loops began to widen which led to a higher dissipated energy. PHD dissipated 1,021 kip-in. (115 kN-m) of energy prior to the failure.

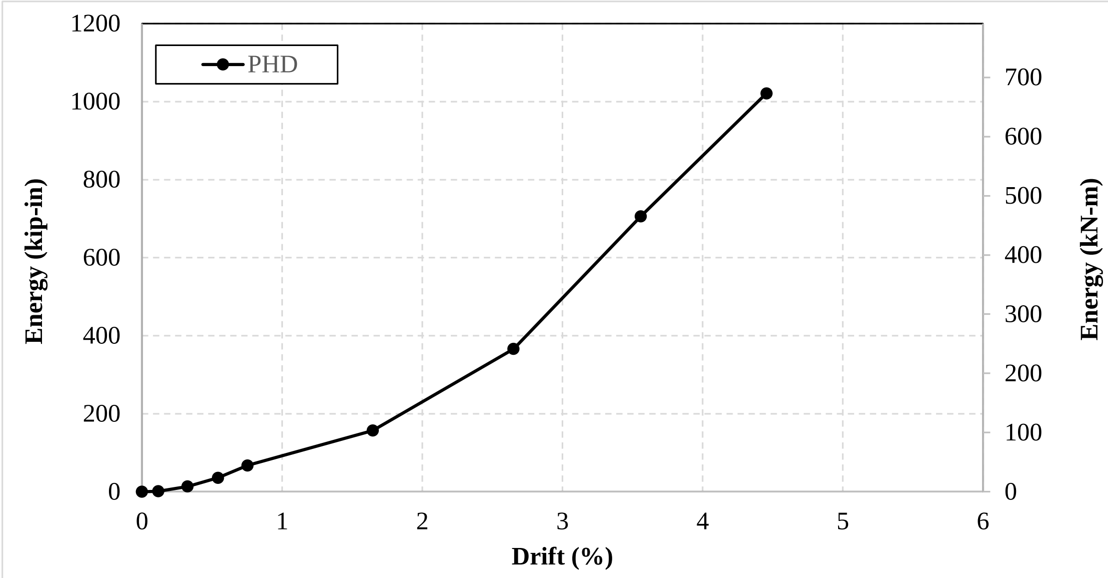

Figure 3.140. Energy Dissipation for PHD Column

3.6 Precast Column Evaluation

The test results were presented for each column individually in the previous sections. This section evaluates the precast columns, PGD, PGS, and PHD, in comparison with the reference CIP column. The force-displacement relationship, strain profiles, and energy dissipation of the columns are compared.

3.6.1 Observed Damage

Figure 3.141 shows the damage of the plastic hinge for CIP, PGD, PGS, and PHD after the second pull of the 2% drift cycle. The coupler used in PGD was the longest of the couplers used in the precast specimens. PGD also showed the least number of cracks within the plastic hinge region. CIP, PGS, and PHD had numerous cracks in the plastic hinge region after the 2% drift cycle.

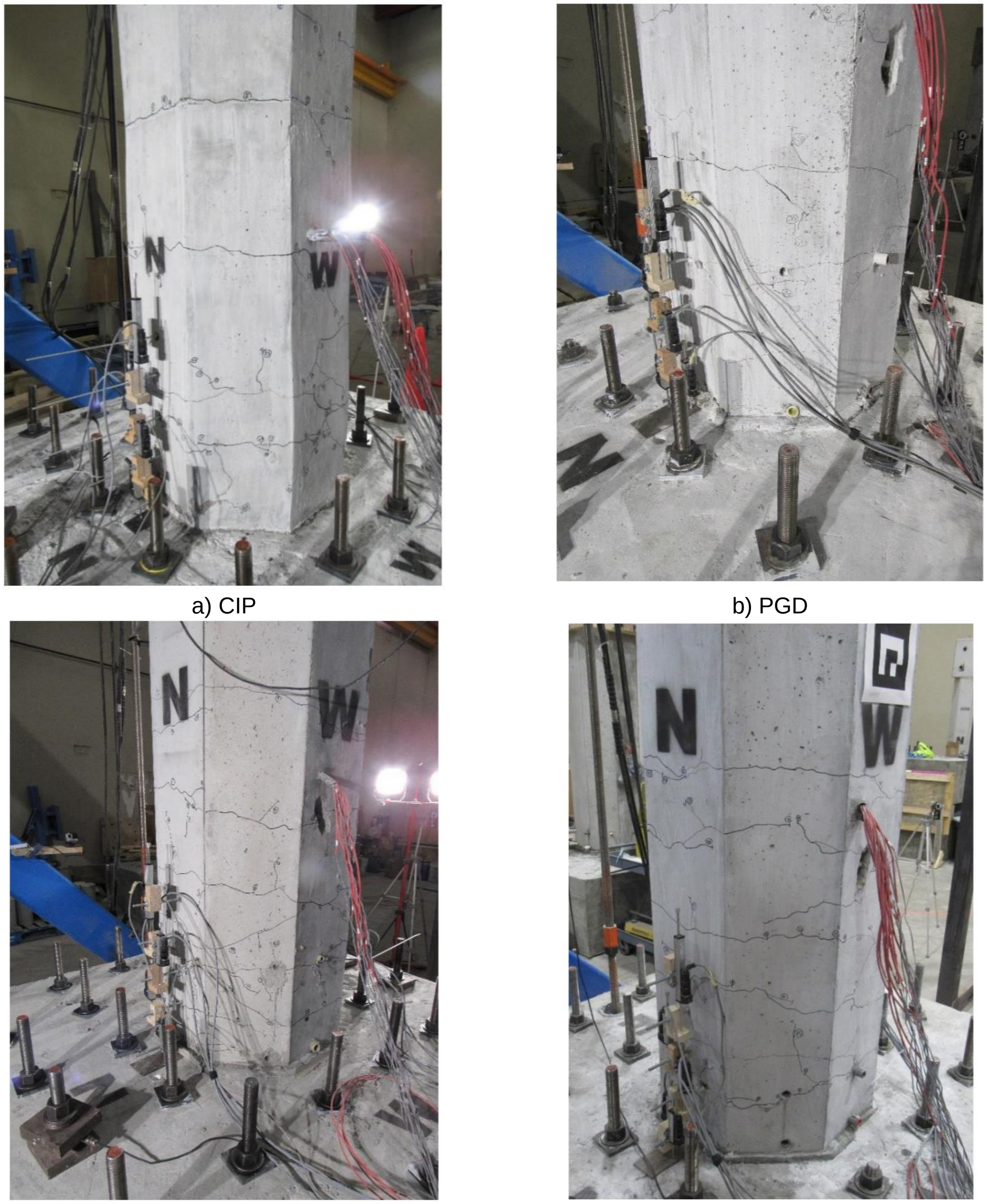

a) CIP b) PGD

c) PGS d) PHD

Figure 3.141. CIP, PGD, PGS, and PHD Plastic Hinge Damage after 2% Drift Cycle

Figure 3.142 shows the damage of the plastic hinge for CIP, PGD, PGS, and PHD at the respective failure states. CIP and PGS both had extensive concrete spalling and longitudinal bar exposure at the failure state before failing due to longitudinal bar rupture. PGD and PHD showed minor concrete spalling at the failure state before failing due to longitudinal bar pullout from the coupler.

a) CIP – 10%


b) PGD – 6%

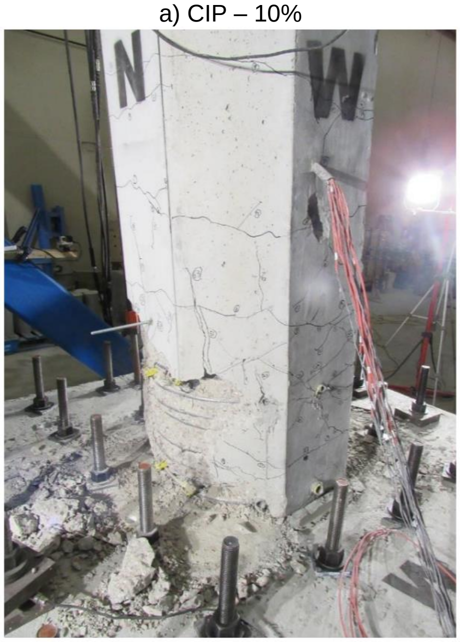

c) PGS – 9%

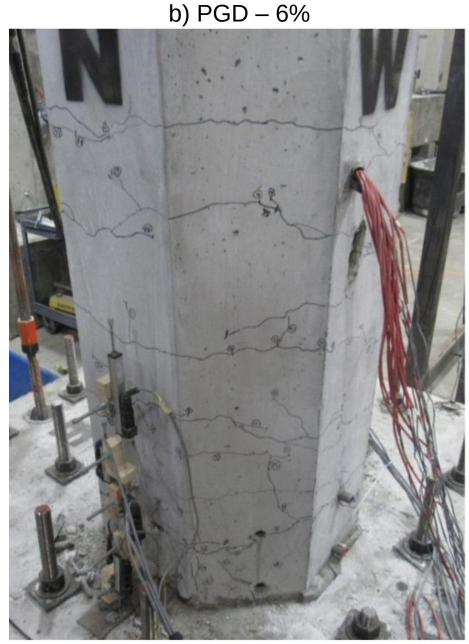

d) PHD – 4%

Figure 3.142. CIP, PGD, PGS, and PHD Plastic Hinge Damage at Failure State

3.6.2 Force-Displacement Relationship

Figure 3.143 shows the measured lateral force-drift hysteretic curves for CIP, PGD, PGS, and PHD. The precast columns exhibited similar behavior compared with that of CIP up to their failure point. All columns showed a wide and stable hysteretic

behavior. The precast columns showed a slightly higher stiffness and a higher lateral resistance compared with CIP due to the higher concrete compressive strength.

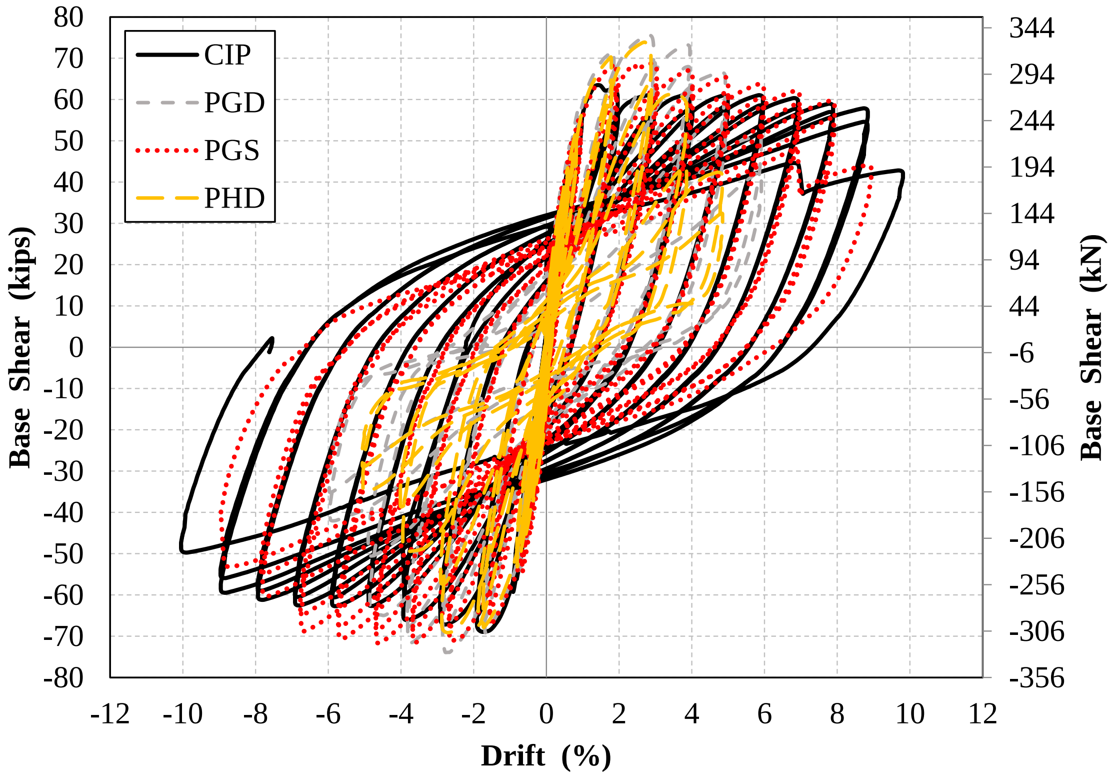

Figure 3.143. Measured CIP, PGD, PGS, and PHD Force-Drift Hysteretic Responses

Figure 3.144 shows the measured average push and pull lateral force-drift (pushover) envelopes for all columns. The displacement ductility capacity of PGD, PGS, and PHD was 53%, 27%, and 71% less than CIP, respectively. Both PGD and PHD failed due to longitudinal bar pullout from the coupler based. PGS failed by longitudinal bar rupture, and therefore showed the highest displacement ductility capacity. The displacement capacity of PGD, PGS, an PHD was 45%, 14%, and 63% less than that of CIP, respectively. Also included in the figure, is the design level drift demand based on the AASHTO spectrum for Downtown of Los Angeles, CA, which is a high seismic area. It can be seen that all columns including the precast ones meet the current seismic design

requirements since (i) they had a displacement ductility capacity that was higher than the minimum required displacement ductility capacity of 3, (ii) they showed a displacement capacity that exceeded the design displacement demand (e.g., for LA), and (iii) their displacement ductility demand was less than 5.

Overall, even though some precast columns performed better than others, they are all acceptable and can be used in all seismic regions of the nation.

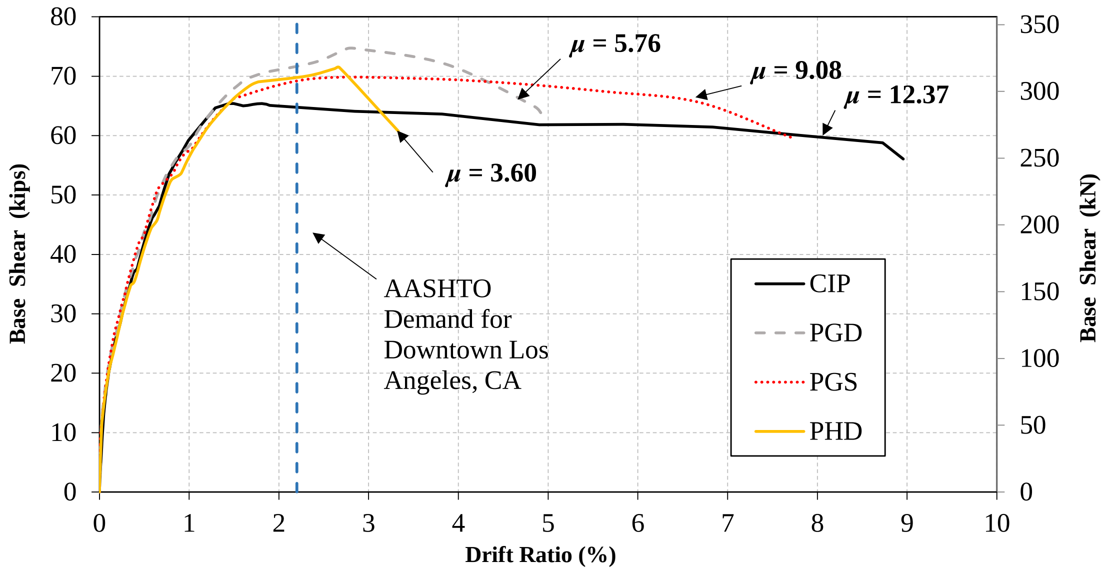

Figure 3.144. Measured CIP, PGD, PGS, and PHD Column Pushover Envelope

3.6.3 Strain Profile

Figures 3.145 to 3.146 show the peak tensile strain profiles at various levels for CIP, PGD, PGS, and PHD. Note that stain gauges were not placed on the couplers. Therefore, strain data is not available at some levels for PGD, PGS, and PHD. All columns generally had ~~a~~ higher strains at the column base. The strain profile for CIP was typical in which the strain was the highest at the base and gradually reduced above and below the column-footing interface (solid black lines). However, at larger drift ratios, the mechanically spliced precast columns exhibited higher strains below and above the

coupler levels compared with CIP. This is due to the fact the coupler region is much stiffer and; therefore, shifts the nonlinearity outside of the coupler region causing a higher strains on the longitudinal bar immediately beyond the coupler.

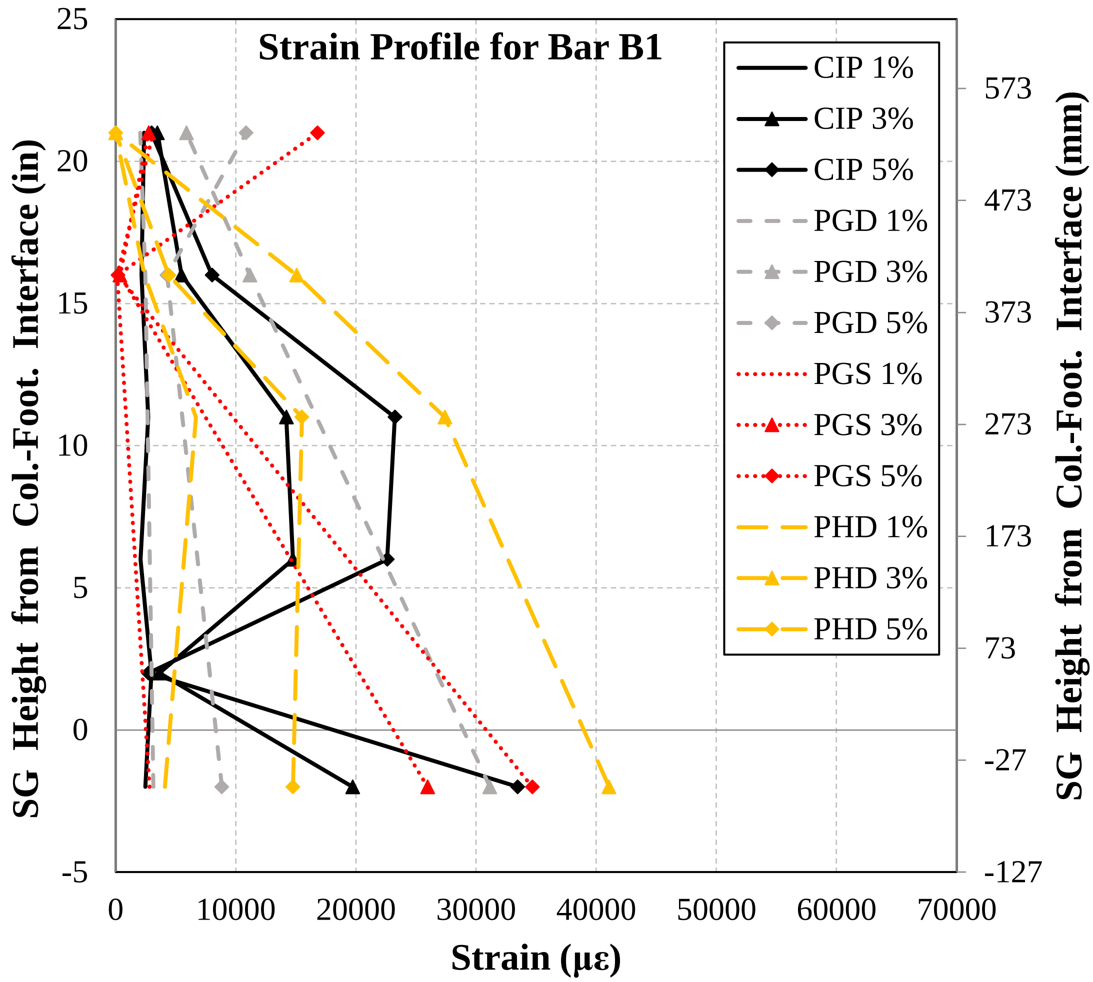

Figure 3.145. Measured CIP, PGD, PGS, and PHD Strain Profile for Bar B1

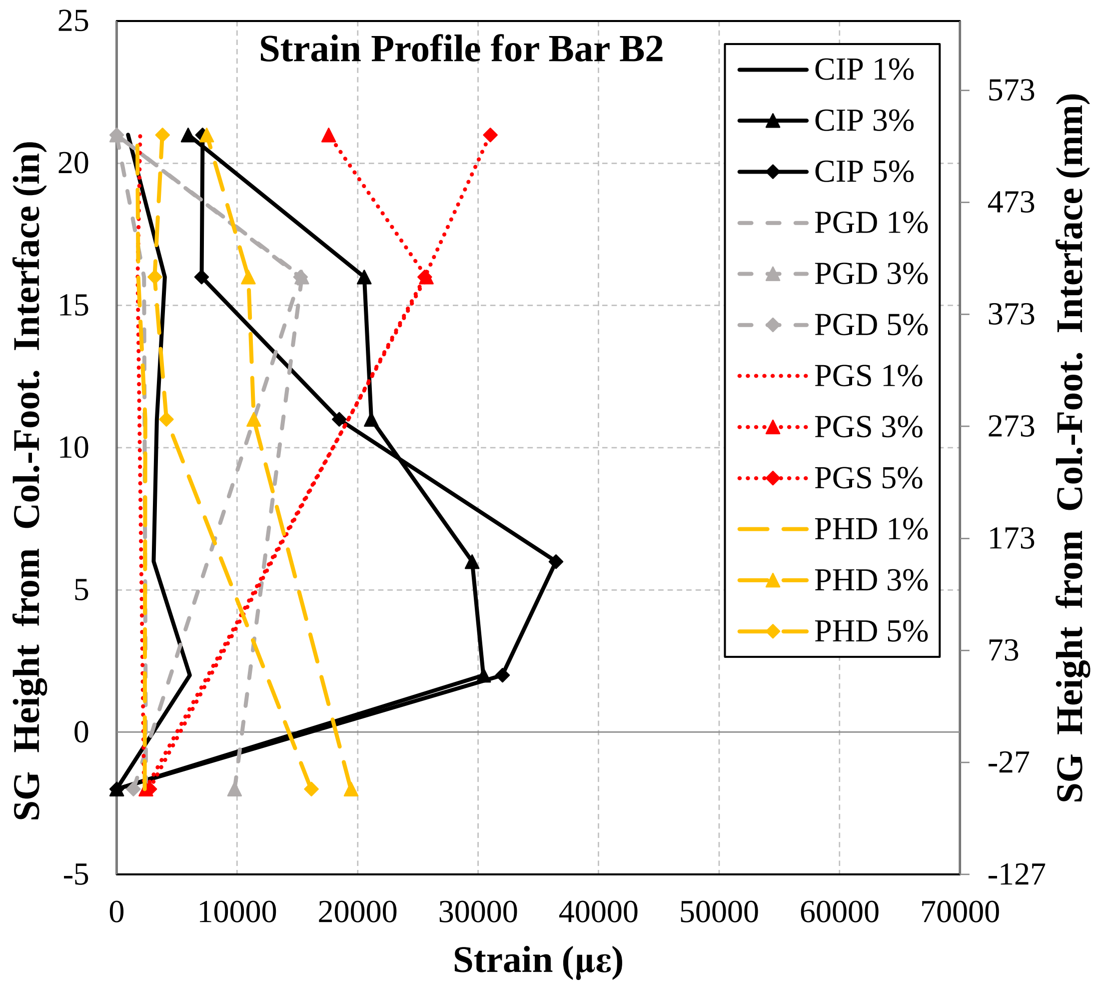

Figure 3.146. Measured CIP, PGD, PGS, and PHD Strain Profile for Bar B2

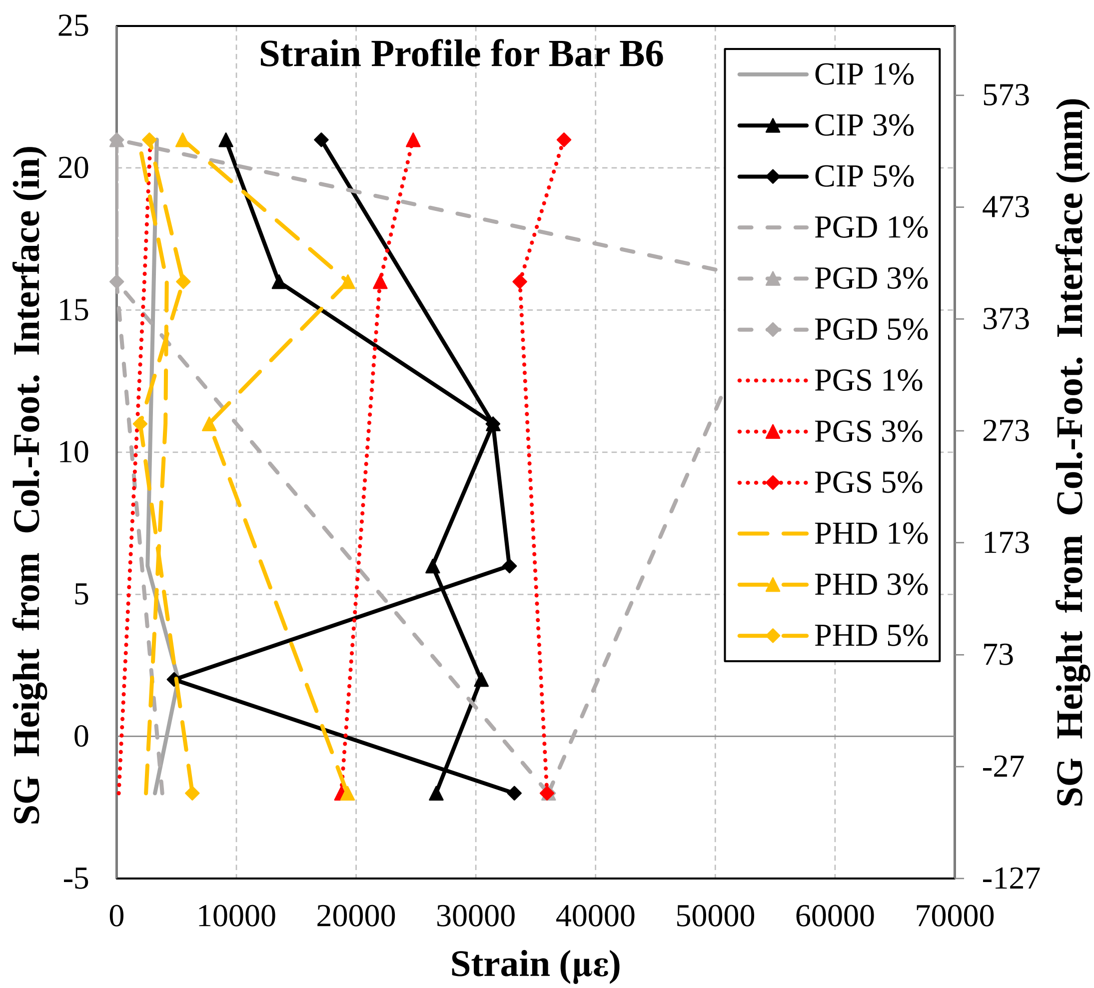

Figure 3.147. Measured CIP, PGD, PGS, and PHD Strain Profile for Bar B6

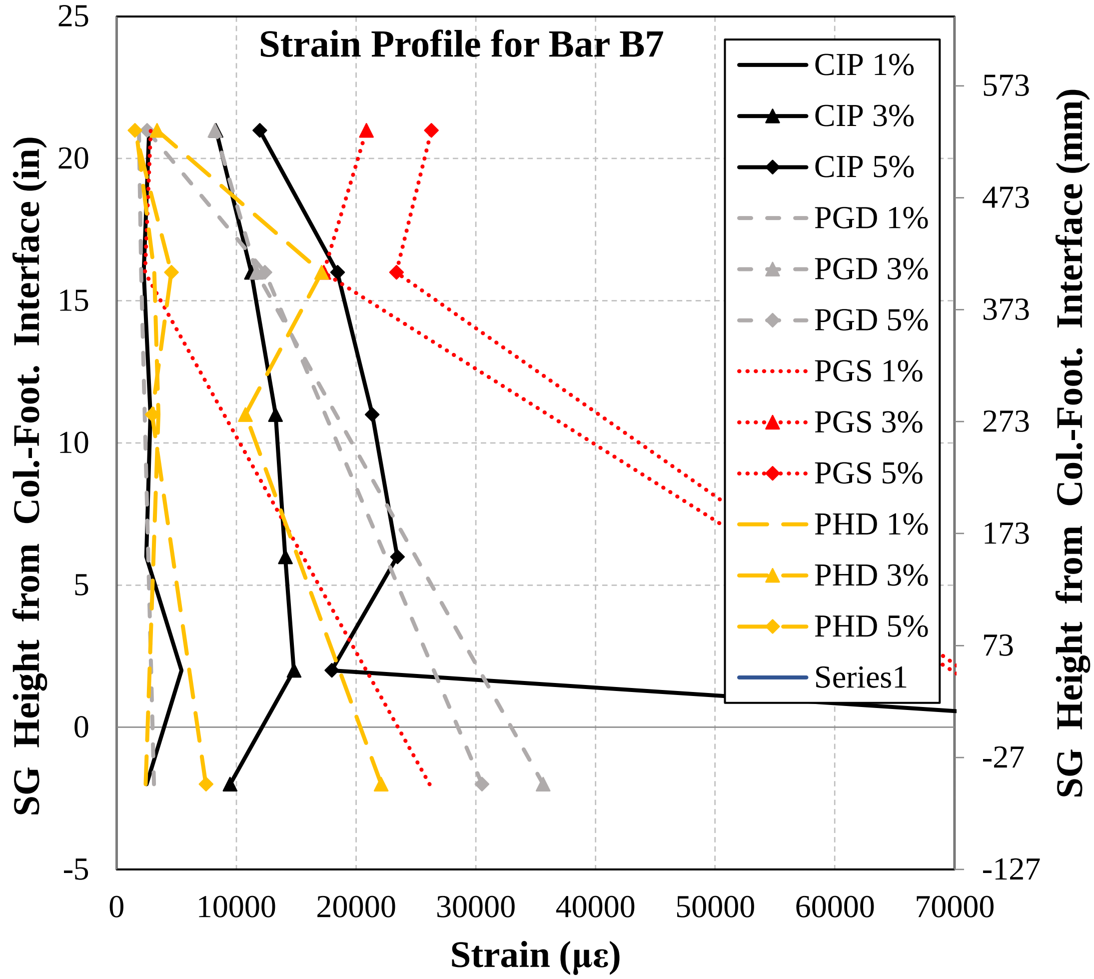

Figure 3.148. Measured CIP, PGD, PGS, and PHD Strain Profile for Bar B7

3.6.4 Energy Dissipation

Figure 3.149 shows the cumulative energy dissipation of CIP, PGD, PGS, and PHD. The precast columns all had a lower energy dissipation than CIP. The precast columns never showed more than 25% less energy dissipation than CIP at a given drift ratio. The energy dissipation of PGD, PGS, and PHD plotted along nearly the same line, limited to the displacement capacity of the respective column.

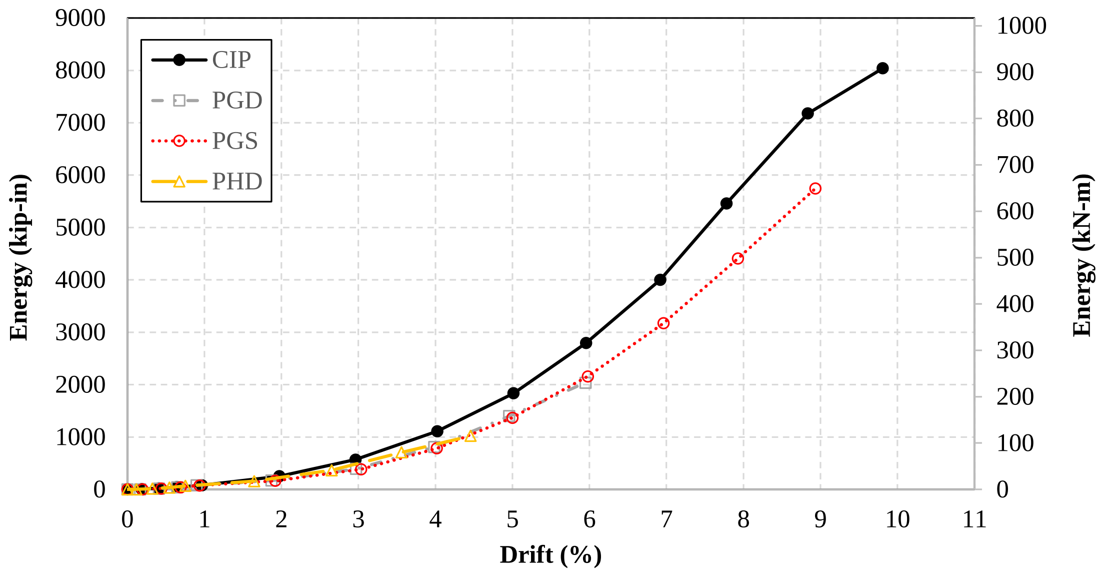

Figure 3.149. Energy Dissipation for CIP, PGD, PGS, and PHD

3.7 Summary and Conclusions

Four half-scale columns were tested under a slow cyclic loading to failure. One column was a cast-in-place column (CIP), which served as the reference. Three columns were precast, PGS, PGD, and PHD, that incorporated different mechanical bar splices at the column-to-footing connection. The summary of the experimental findings is as follows:

- The mode of failure for CIP and PGS was the longitudinal bar rupture.
- The mode of failure for PGD and PHD was the longitudinal bar pullout from the base~~d o~~ of the mechanical bar splices.
- The drift ratio capacity for CIP, PGD, PGS, and PHD was 9.0%, 4.9%, 7.7%, and 3.3% respectively.
- All columns including the precast columns met the AASHTO seismic requirements thus they are recommended for use in all 50 states of the nation.

3.8 References

AASHTO SGS (2011) “AASHTO Guide Specifications for Seismic Bridge Design,” Washington, D.C., American Association of State Highway and Transportation Officials.

ACI 374.2R-13 (2013). “Guide for Testing Reinforced Concrete Structural Elements Under Slowly Applied Simulated Seismic Loads.” American Concrete Institute (ACI) Committee 374, Farmington Hills, MI, 2013.

ASTM A706 (2016). “Standard Specification for Low-Alloy Steel Deformed and Plain Bars for Concrete Reinforcement.” West Conshohocken, PA, 6 pp.

ASTM E8 (2012). “Standard Test Methods for Tension Testing of Metallic Materials.” ASTM International, West Conshohocken, PA.

ASTM A1034 (Sep. 2016). “Standard Test Methods for Testing Mechanical Splices for Steel Reinforcing Bars.” ASTM International, West Conshohocken, PA.

ASTM C109/C109M-11b. (2011). “Standard Test Method for Compressive Strength of Hydraulic Cement Mortars (Using 2-in. or [50-mm] Cube Specimens),” West Conshohocken, PA.

ASTM C39/C39M-12. (2012). “Standard Test Method for Compressive Strength of Cylindrical Concrete Specimens,” West Conshohocken, PA.

ASTM E8 (2012). “Standard Test Methods for Tension Testing of Metallic Materials.” ASTM International, West Conshohocken, PA.

Caltrans. (2019). “Caltrans Seismic Design Criteria (SDC), Version 2.0” Sacramento, CA.: California Department of Transportation, 250 pp.

Dahal, P.K., and Tazarv, M. (2020). “Mechanical Bar Splices for Incorporation in Plastic Hinge Regions of RC Members,” Construction and Building Materials, Vol. 258, 120308, 17 pp.

Hewes, J.T. (2013). “Analysis of the State of the Art of Precast Concrete Bridge Substructure Systems.” Arizona. Dept. of Transportation, Research Center, Report No. FHWA-AZ-13-687, 124 pp.

Krawinkler, H. and Moncarz, P.D. (1982). Similitude Requirements for Dynamic Models.” ACI Special Publication, Vol. 73, pp. 1-22.

LaVoy, M.R. (2020). “Seismic Performance of Mechanically Spliced Bridge Columns Through Analytical Studies.” MS Thesis, South Dakota State University, 106 pp.

Tazarv, M. and Saiidi, M.S. (2016). “Seismic Design of Bridge Columns Incorporating Mechanical Bar Splices in Plastic Hinge Regions,” Engineering Structures, DOI: 10.1016/j.engstruct.2016.06.041, Vol 124, pp. 507-520.

Chapter 4. Analytical Investigation of Column Test Specimens

4.1 Introduction

The experimental results of four half-scale bridge columns were presented in the previous chapter. In this chapter, an analytical study is performed to verify the current modeling methods of bridge columns, specifically mechanically spliced bridge columns. A finite element computer program, Opensees (2016), was used for simulations.

There are several successful studies on how to simulate conventional bridge columns, a few models were developed by the research team (e.g., Tazarv and Saiidi, 2016; LaVoy, 2020). One of those analytical methods will be discussed in the next section for conventional bridge columns. However, modeling methods for mechanically spliced bridge columns are limited. Haber et al. (2015) proposed a multi-element fiber-section finite element method including a new coupler material model to simulate the response of mechanically spliced columns (Fig. 4.1). Tazarv and Saiidi (2016) and later in NCHRP 935 (2020) proposed three methods to analyze and design mechanically spliced bridge columns, which are summarized in Table 4.1. They also proposed a stress-strain model for couplers (Fig. 4.2), which was discussed in Ch. 2 of this document. Ameli and Pantelides (2017) developed an iterative finite element lumped plasticity model for coupler columns in which the length of the plastic hinge region, which was

required in lumped plasticity elements, was iterated. Of different modeling techniques for mechanically spliced bridge columns, the distributed plasticity model developed by Tazarv and Saiidi (2016) (Method 3 in Table 4.1) was selected for further investigation.

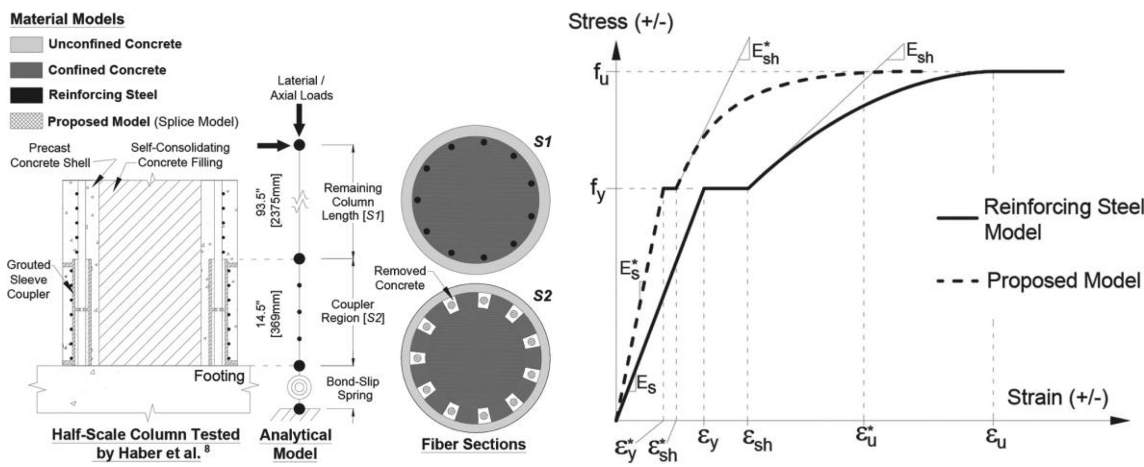

(a) Column Model (b) Coupler Model

Figure 4.1. Finite Element Modeling Method for Mechanically Spliced Bridge Columns (Haber et al., 2015)

Table 4.1. Summary of Modeling Methods for Mechanically Spliced Columns (Tazarv and Saiidi, 2016)

Design Method	Analysis Type	Column Element in Pushover Analysis	Analysis Requirements
Cast-in-place (CIP) columns	Moment-Curvature or Pushover	Usually conducted using a lumped plasticity model, which requires an analytical plastic hinge length. However, distributed plasticity model can also be utilized	AASHTO Guide Specifications for LRFD Seismic Bridge Design
Method 1. Spliced columns using a displacement ductility equation	Use CIP analysis results	Use CIP analysis results	$\frac{\mu_{sp}}{\mu_{CIP}} = (1 - 0.18\beta)(\frac{H_{sp}}{L_{sp}})^{0.1\beta}$
Method 2. Spliced columns using modified plastic hinge length equation	Moment-Curvature or Pushover	Lumped plasticity model only	Similar to CIP but with $L_p^{sp} = L_p - (1 - \frac{H_{sp}}{L_p})\beta L_{sp} \leq L_p$
Method 3. Spliced columns using proposed stress-strain model for couplers	Pushover only	Distributed plasticity model only	Coupler stress-strain model (Fig. 4.2)

Note: μ_{sp}: The mechanically spliced bent displacement ductility capacity; μ_{CIP}: The corresponding non-spliced cast-in-place bent displacement ductility capacity; β: The coupler rigid length ratio; H_{sp}: The distance from the column end to the nearest face of the coupler embedded either inside the column or inside the column adjoining member (*in*.); L_{sp}: The coupler length (*in*.); L_p^{sp}: The modified plastic hinge length for mechanically spliced bridge columns; L_p: The conventional column analytical plastic hinge length according to the current AASHTO SGS.

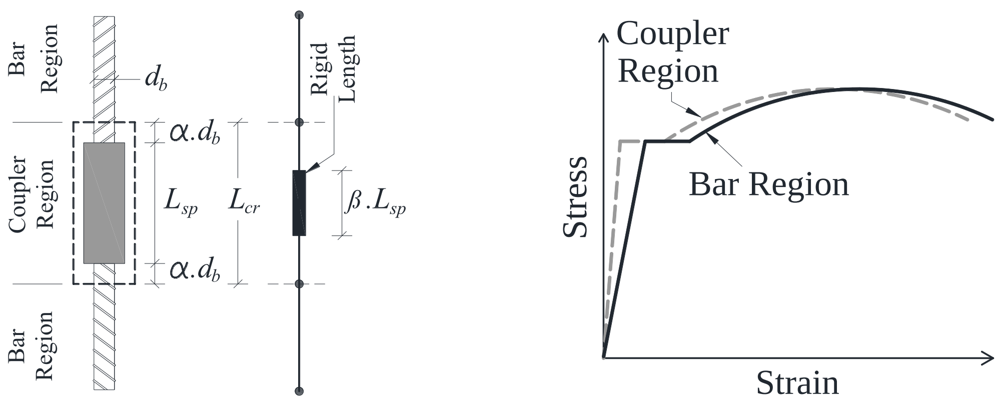

(a) Coupler Region (b) Coupler Stress-Strain Model

Figure 4.2. Generic Stress-Strain Model for Mechanical Bar Splices (Tazarv and Saiidi, 2016)

4.2 Analysis of Column Test Specimens

This section describes the modeling methods developed for the four column specimens tested in this project.

4.2.1 Modeling Methods

A three-dimensional fiber-section finite element model with six degrees of freedom (DOFs) was used to simulate the CIP, PGD, PGS, and PHD columns in Opensees (2016). The height for all columns was 8 ft (2.44 m). An octagonal cross-section was used in all columns, which had a side dimension of 24 in. (610 mm) across flats. Each column was longitudinally reinforced with 10 – No. 8 (25-mm) bars (ρ_L = 1.66%) and transversely with No. 4 (13-mm) hoops at 2 in. (51 mm).

Figure 4.3 shows the analytical finite element model developed for CIP, in which a single "forceBeamColumn" element with four integration points was used for the entire column length since the cross section was consistent. The CIP column sectional properties were simulated with the cover, core, and rebar uniaxial fibers. The core concrete was discretized into 50x50 fibers and modeled with "Concrete01". The cover concrete was discretized into 10x4 fibers and modeled with "Concrete01". The clear cover was defined as the minimum distance between the column surface to the exterior of the confining reinforcement. The column fiber properties were based on the measured mechanical properties of each material discussed in Chapter 3. The properties of the confined (or core) concrete were calculated using the model proposed by Mander et al. (1988). Table 4.2 presents a summary of the material models used in the CIP analytical model. The P-Δ effects and the bond-slip effects (based on a modified stress-strain relationship of steel bars according to Tazarv and Saiidi, 2014) were included.

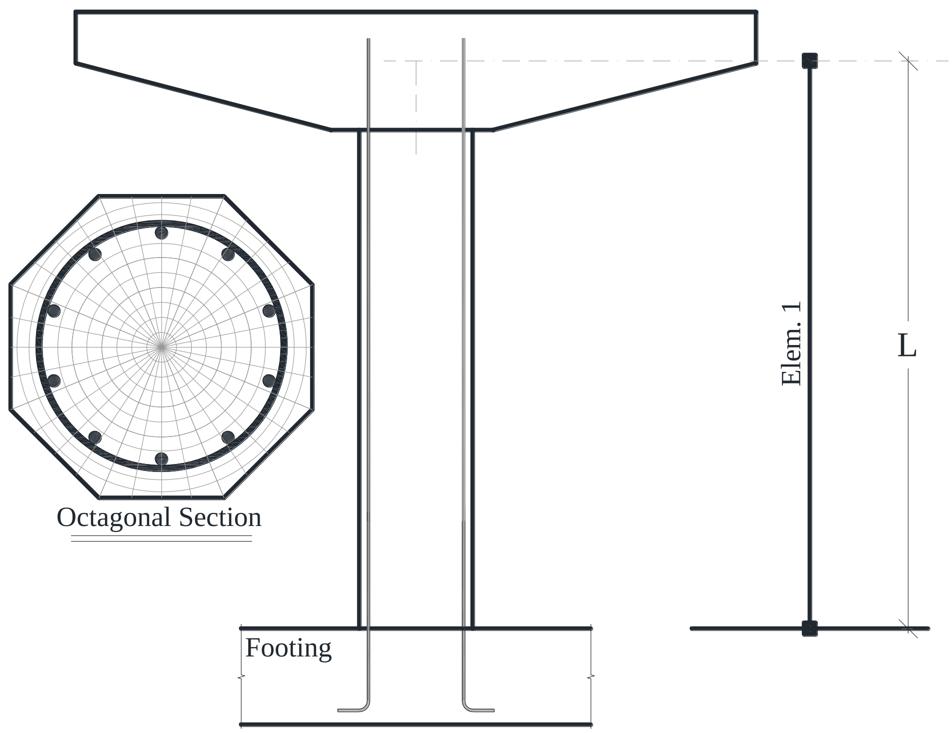

Figure 4.3. Analytical Modeling Method for Cast-in-Place Column

Table 4.2. Sectional Fiber Material Properties Used in CIP

Concrete Fibers	
Application: unconfined concrete Type: Concrete01 f'_{cc} = 4300 psi (29.6MPa) ε_{cc} = -0.002 in/in f'_{cu} = 0.0 psi (0 MPa) ε_{cu} = -0.005 in/in	Application: confined concrete (based on Mander's model) Type: Concrete01 f'_{cc} = 7930 psi (54.7 MPa) ε_{cc} = -0.0104 in/in f'_{cu} = 6950 psi (47.9 MPa) ε_{cu} = -0.0341 in/in
Steel Fibers	
Application: unspliced bars at the base including bond-slip effects Type: ReinforcingSteel f_y = 69.3 ksi (477.8 MPa) f_{su} = 97.4 ksi (671.5 MPa) E_s = 10640 ksi (20000 MPa) E_{sh} = 840 ksi (5880 MPa) ε_{sh} = 0.009 in/in ε_{su} = 0.126 in/in	Application: unspliced bars above the base Type: ReinforcingSteel f_y = 69.3 ksi (477.8 MPa) f_{su} = 97.4 ksi (671.5 MPa) E_s = 29000 ksi (20000 MPa) E_{sh} = 853 ksi (5880 MPa) ε_{sh} = 0.005 in/in ε_{su} = 0.12 in/in

The behavior of the three mechanically spliced precast bridge columns, PGD, PGS, and PHD, were simulated using a consistent modeling method based on Method 3 (Table 4.1) developed by Tazarv and Saiidi (2016). Figure 4.2 shows the analytical model for the coupler columns. Similar to CIP, a three-dimensional fiber-section finite element model with six DOFs was used to simulate the precast column behavior in OpenSees (2016). However, three elements were needed to successfully include the sectional changes. Element 1 was a “zeroLength” element to monitor the stress-strain behavior of steel and concrete fibers. In this element, the bond-slip effects can also be included by modifying the longitudinal steel reinforcement properties (e.g., Table 4.3). Elements 2 and 3 were “forceBeamColumn” elements, each with five integration points. Element 2 was used to include the coupler effects by modifying the steel bar properties based on the coupler model (Fig. 4.2). The coupler rigid length factor was based on the measured properties (Table 3.5 of Ch. 3). Figure 4.5 shows the reproduced coupler stress-strain behavior that was used in the analytical study for the three coupler types used in the three precast columns. Note that the curves for the three couplers are approximately the same since the coupler rigid length factor for these couplers were close (0.7, 0.7, 0.79 for couplers respectively used in PGD, PGS, and PHD). Tables 4.3 – 4.5 provide a summary of the material models used for PGD, PGS, and PHD, respectively.

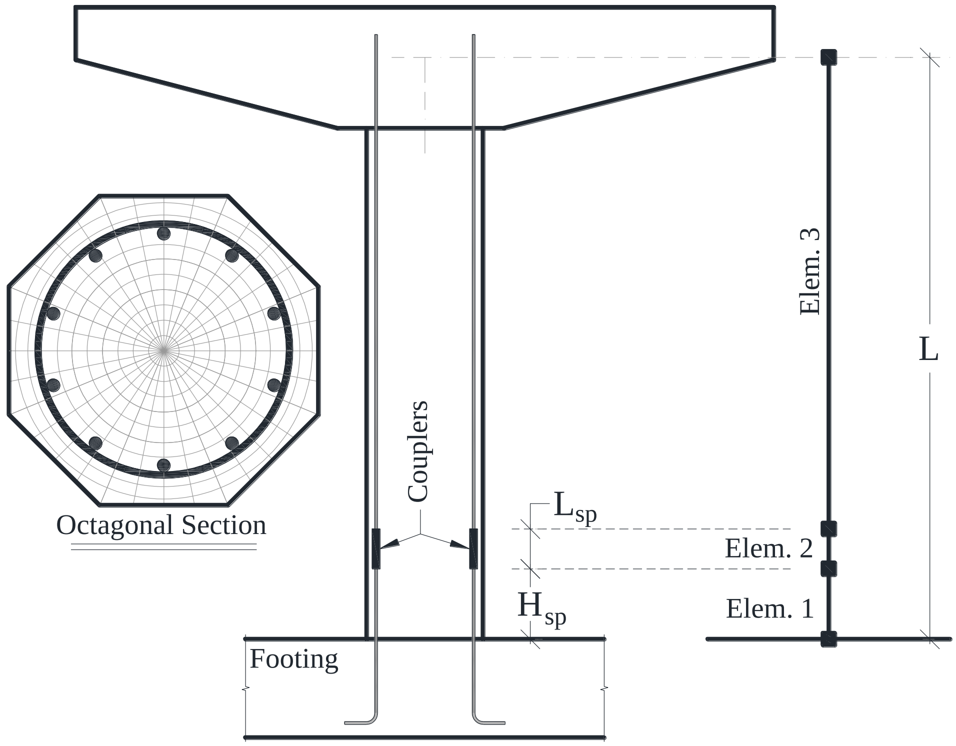

Figure 4.4. Analytical Modeling Method for Mechanically Spliced Columns

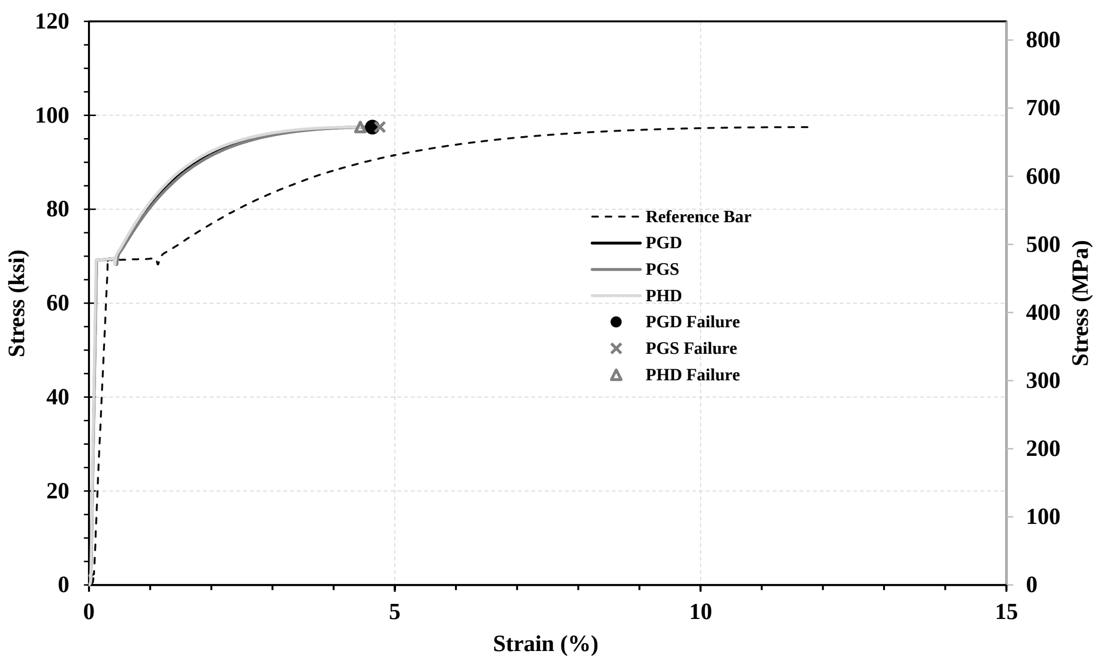

Figure 4.5. Coupler Stress-Strain Used in Mechanically Spliced Column Analytical Models

Table 4.3. Sectional Fiber Material Properties Used in PGD

Concrete Fibers	
Application: unconfined concrete Type: Concrete01 f'_{cc} = 7950 psi (54.8 MPa) ε_{cc} = -0.002 in/in f'_{cu} = 2540 psi (17.5 MPa) ε_{cu} = -0.005 in/in	Application: confined concrete (based on Mander's model) Type: Concrete01 f'_{cc} = 11730 psi (80.9 MPa) ε_{cc} = -0.0068 in/in f'_{cu} = 8810 psi (60.8 MPa) ε_{cu} = -0.0226 in/in
Steel Fibers	
Application: unspliced bars (Element 1) including bond-slip effects Type: ReinforcingSteel f_y = 69.3 ksi (477.8 MPa) f_{su} = 97.4 ksi (671.5 MPa) E_s = 10640 ksi (20000 MPa) E_{sh} = 840 ksi (5880 MPa) ε_{sh} = 0.009 in/in ε_{su} = 0.126 in/in	Application: spliced bars (Element 2) with Beta = 0.70 Type: ReinforcingSteel f_y = 69.3 ksi (477.8 MPa) f_{su} = 97.4 ksi (671.5 MPa) E_s = 83700 ksi (577000 MPa) E_{sh} = 2460 ksi (17000 MPa) ε_{sh} = 0.0040 in/in ε_{su} = 0.0416 in/in
Application: unspliced bars (Element 3) without bond-slip effects Type: ReinforcingSteel f_y = 69.3 ksi (477.8 MPa) f_{su} = 97.4 ksi (671.5 MPa) E_s = 29000 ksi (200000 MPa) E_{sh} = 853 ksi (5880 MPa) ε_{sh} = 0.005 in/in ε_{su} = 0.12 in/in	

Table 4.4. Sectional Fiber Material Properties Used in PGS

Concrete Fibers	
Application: unconfined concrete Type: Concrete01 f'_{cc} = 8880 psi (61.2 MPa) ε_{cc} = -0.002 in/in f'_{cu} = 2840 psi (19.6 MPa) ε_{cu} = -0.005 in/in	Application: confined concrete (based on Mander's model) Typeoncrete01 f'_{cc} = 12480 psi (88.5 MPa) ε_{cc} = -0.0065 in/in f'_{cu} = 9090 psi (62.7 MPa) ε_{cu} = -0.0218 in/in
Steel Fibers	
Application: unspliced bars (Element 1) including bond-slip effects Type: ReinforcingSteel f_y = 69.3 ksi (477.8 MPa) f_{su} = 97.4 ksi (671.5 MPa) E_s = 10640 ksi (20000 MPa) E_{sh} = 840 ksi (5880 MPa) ε_{sh} = 0.009 in/in ε_{su} = 0.126 in/in	Application: spliced bars (Element 2) with Beta = 0.70 Type: ReinforcingSteel f_y = 69.3 ksi (477.8 MPa) f_{su} = 97.4 ksi (671.5 MPa) E_s = 75400 ksi (520000 MPa) E_{sh} = 2220 ksi (15300 MPa) ε_{sh} = 0.0044 in/in ε_{su} = 0.0461 in/in
Application: unspliced bars (Element 3) without bond-slip effects Type: ReinforcingSteel f_y = 69.3 ksi (477.8 MPa) f_{su} = 97.4 ksi (671.5 MPa) E_s = 29000 ksi (200000 MPa) E_{sh} = 853 ksi (5880 MPa) ε_{sh} = 0.005 in/in ε_{su} = 0.12 in/in	

Table 4.5. Sectional Fiber Material Properties Used in PHD

Concrete Fibers	
Application: unconfined concrete Type: Concrete01 f'_{cc} = 9640 psi (66.5 MPa) ε_{cc} = -0.002 in/in f'_{cu} = 3080 psi (21.2 MPa) ε_{cu} = -0.005 in/in	Application: confined concrete (based on Mander's model) Type: Concrete01 f'_{cc} = 13640 psi (94.0 MPa) ε_{cc} = -0.0062 in/in f'_{cu} = 9410 psi (64.9 MPa) ε_{cu} = -0.0205 in/in
Steel Fibers	
Application: unspliced bars (Element 1) including bond-slip effects Type: ReinforcingSteel f_y = 69.3 ksi (477.8 MPa) f_{su} = 97.4 ksi (671.5 MPa) E_s = 10640 ksi (20000 MPa) E_{sh} = 840 ksi (5880 MPa) ε_{sh} = 0.009 in/in ε_{su} = 0.126 in/in	Application: spliced bars (Element 2) with Beta = 0.79 Type: ReinforcingSteel f_y = 69.3 ksi (477.8 MPa) f_{su} = 97.4 ksi (671.5 MPa) E_s = 83300 ksi (574000 MPa) E_{sh} = 2450 ksi (16900 MPa) ε_{sh} = 0.0040 in/in ε_{su} = 0.0418 in/in
Application: unspliced bars (Element 3) without bond-slip effects Type: ReinforcingSteel f_y = 69.3 ksi (477.8 MPa) f_{su} = 97.4 ksi (671.5 MPa) E_s = 29000 ksi (200000 MPa) E_{sh} = 853 ksi (5880 MPa) ε_{sh} = 0.005 in/in ε_{su} = 0.12 in/in	

The stress-strain data was monitored for the extreme concrete and steel fibers at the column base (Element 1). Furthermore, the column tip displacements and lateral forces were recorded. The column analytical failure point was the displacement in which one of the following limit states first occurred:

1) The extreme steel fiber reached its ultimate tensile strain,
2) The extreme concrete core fiber reached the ultimate compressive strain,
3) The column lateral load carrying capacity reduced by 15% compared to the peak lateral strength.

4.2.2 Force-Displacement Relationships

The calculated pushover response of each column model is compared with its corresponding test column response in this section. In future studies, the full cyclic response will be included for completeness.

Figure 4.6 shows the calculated and measured force-displacement relationships for CIP. The calculated and measured initial stiffness matched well. Between drifts of 1% and 3%, the calculated forces were lower than those measured in the test due to the loss of the large cover concrete used in CIP. Note that the CIP column concrete cover was higher than a typical conventional column. This was done to include the coupler size and to have a same bar distribution in CIP and precast columns. The calculated forces were slightly lower than the measured forces after 3% drifts, but overall matched well. The CIP calculated peak lateral strength was 60.8 kips (270 kN) while the CIP measured lateral strength was 65.4 kips (291 kN), or a 7.0% difference. Most importantly, the CIP calculated failure drift ratio was 8.65% whereas the CIP measured failure drift was 8.96% (less than 4% error). Furthermore, the model predicts that CIP fails in bar fracture, which was also seen in the actual test. Overall, the analytical model for CIP was able to reproduce the actual behavior with a reasonable accuracy especially in terms of the initial stiffness and the ultimate displacement.

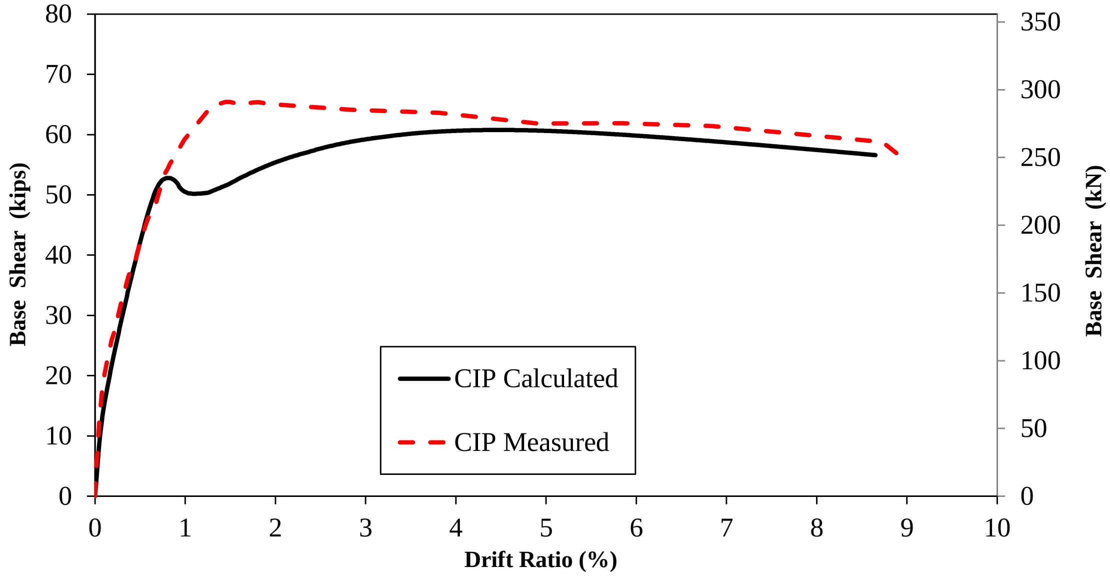

Figure 4.6. Calculated and Measured Force-Drift Relationship for CIP

Figure 4.4. shows the calculated and measured force-displacement relationships for PGD. The calculated and measured initial stiffness matched well. The calculated forces were higher at low drift ratios and lower at high drift ratios, though the force matched well overall. The PGD calculated peak lateral strength was 69.0 kips (307 kN) while its measured lateral strength was 74.7 kips (332 kN), or a 7.6% difference. The PGD calculated failure drift ratio was 4.98% and its measured failure drift was 4.93% (less than 1% error). This is a very interesting finding, specially noting that bars pulled out from the coupler base; however, the proposed column and coupler models were able to capture the failure displacement Overall, the analytical model for PGD was able to reproduce the actual behavior with a good accuracy.

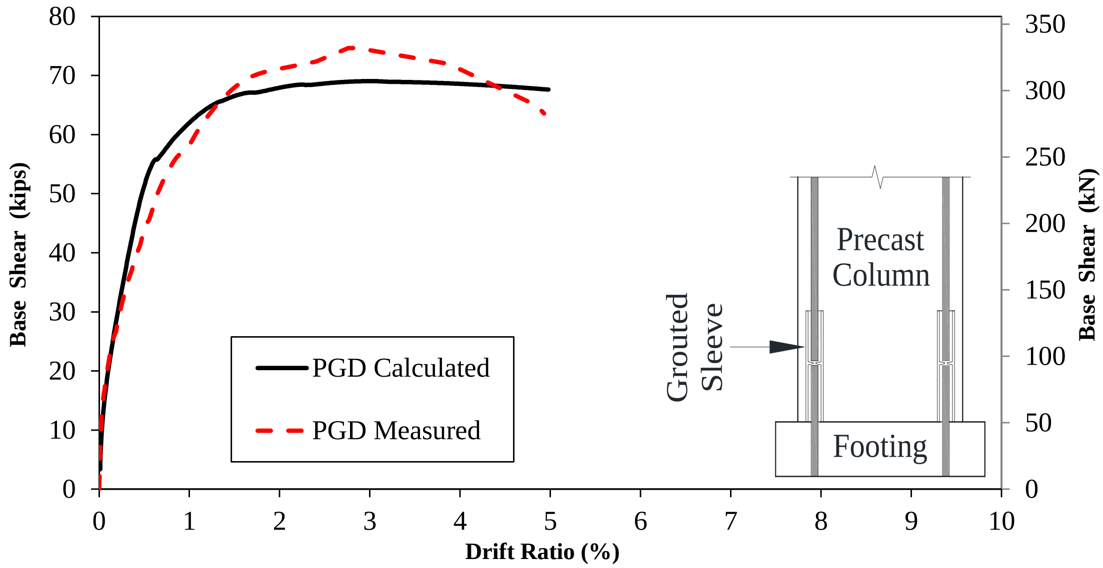

Figure 4.7. Calculated and Measured Force-Drift Relationship for PGD

Figure 4.8 shows the calculated and measured force-displacement relationships for PGS. The calculated and measured initial stiffness matched well. The calculated forces were slightly higher at drift ratios between 0.25% and 1.5%, though the force matched well overall. The PGS calculated peak lateral strength was 69.0 kips (307 kN) while its measured lateral strength was 69.6 kips (310 kN), or less than 1% difference. The PGS calculated drift capacity was 8.50% and its measured failure drift was 7.81% (approximately 8% error). Furthermore, the model predicts that PGS fails in bar fracture, which was also seen in the actual test. Overall, the analytical model for PGS was able to reproduce the actual behavior with a good accuracy.

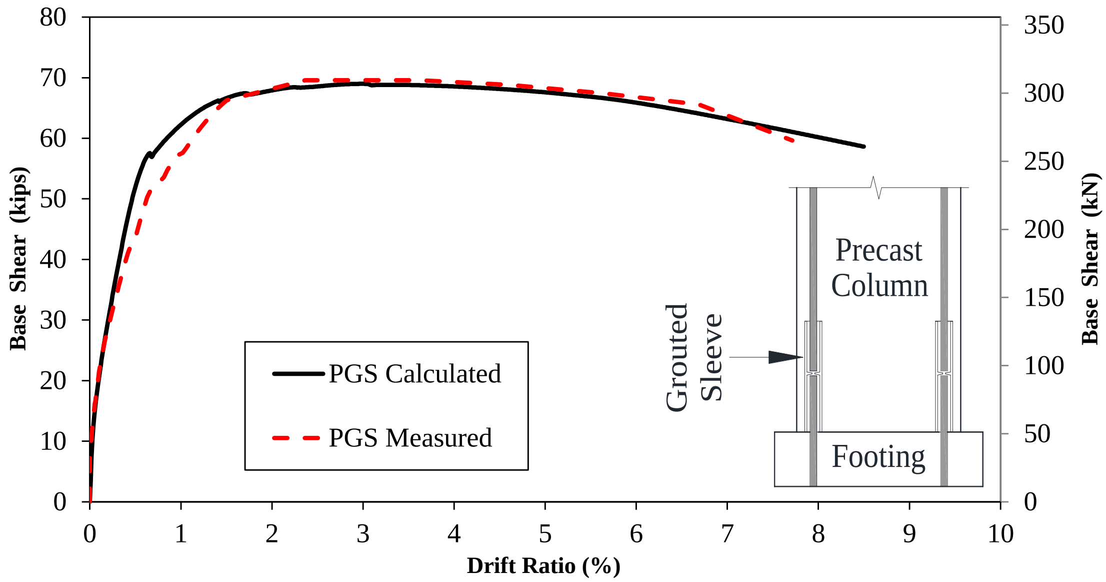

Figure 4.8. Calculated and Measured Force-Drift Relationship for PGS

Prior to the PHD column testing, five couplers were prepared and tested. Four out of five couplers failed by bar pullout in the in-air tensile testing. The PHD column with these couplers also failed by bar pullout at a lower displacement than other columns. Only seismic couplers should be used in bridge columns while those tested for PHD were not. Furthermore, the coupler model by Tazarv and Saiidi (2016, Fig. 4.2) has only been verified for seismic couplers (those that show bar fracture but not bar pullout or coupler fracture).

Figure 4.9 shows the calculated and measured response for PHD. The calculated drift capacity based on the same method used for other precast columns using the average $\beta = 0.79$ was 7.43, which was significantly higher than that measured in the test. The simulation was repeated but with a $\beta = 1.0$, which was for the case in which the bar pullout with the lowest strain capacity of 2.36% (Table 3.5, Ch. 3). Figure 4.9 shows that the PHD drift capacity using this method was 3.90%, which was overestimated by 17%.

In an attempt to estimate the failure displacement of the PHD column using the current analytical model, a new technique was explored in which the analysis was stopped where the coupler strain (the first integration point in Element 2) reached the average coupler test strain of 3.52%. Note in all other analyses, the strain of steel bar in Element 1 (base element) was monitored but not the coupler strain because the couplers are supposed to be stronger than their anchoring bars (seismic couplers). A good estimation of the column failure point was observed using this technique. The calculated and measured initial stiffness matched well. The calculated force was slightly higher at drift ratios between 0.25% and 1.5%, though the force matched well overall. The PHD calculated peak lateral strength was 70.3 kips (313 kN) while its measured lateral strength was 71.5 kips (318 kN), or a 1.7% difference. The PHD calculated drift capacity using the technique discussed above (stopping at the coupler failure) was 3.52% and the measured failure drift was 3.33%. Overall, the proposed method captured the PHD column performance with a reasonable accuracy.

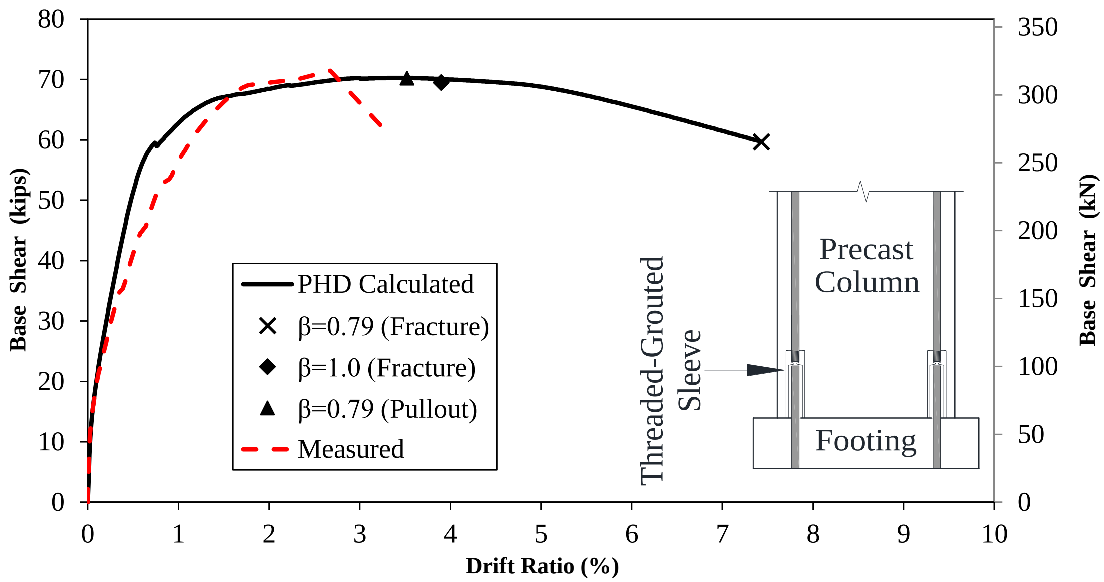

Figure 4.9. Calculated and Measured Force-Drift Relationship for PHD

4.3 Summary and Conclusions

In this chapter, analytical modeling methods were developed, and pushover analyses were performed for the CIP and mechanically spliced precast columns tested in this project. The CIP and precast models were able to successfully reproduce the force-displacement relationship of each column. Overall, the proposed models were found viable and may be used for the analysis and design of bridge columns incorporating seismic couplers.

4.4 References

AASHTO. (2014). "AASHTO Guide Specifications for LRFD Seismic Bridge Design," Washington, DC: American Association of State Highway and Transportation Officials.

Ameli, M.J. and Pantelides, C.P. (2017). "Seismic Analysis of Precast Concrete Bridge Columns Connected with Grouted Splice Sleeve Connectors." Journal of Structural Engineering, 143(2), p.04016176.

Haber, Z.B., Saiidi, M.S. and Sanders, D.H. (2015). "Behavior and Simplified Modeling of Mechanical Reinforcing Bar Splices." ACI Structural Journal, 112(2), p.179.

LaVoy, M.R. (2020). "Seismic Performance of Mechanically Spliced Bridge Columns Through Analytical Studies." MS Thesis, South Dakota State University, 106 pp.

Mander, J.B., Priestley, M.J.N., Park, R. (1988). "Theoretical Stress-Strain Model for Confined Concrete," Journal of Structural Engineering, ASCE, Vol. 114, No. 8, pp. 1804-1826.

OpenSees. (2016). "Open System for Earthquake Engineering Simulations," Version 2.4.1, Berkeley, CA, Available online: http://opensees.berkeley.edu.

Saiidi, M.S., Mehraein, M., Shrestha, G., Jordan, E., Itani, A., Tazarv, M., Sanders, D., Murphy, T.M., Reno, M.L., and Pohll, M.N. (2020). "Proposed AASHTO Seismic Specifications for ABC Column Connections," National Academies of Sciences, Engineering, and Medicine, NCHRP Report No. 935, Washington, DC: The National Academies Press, 354 pp.

Tazarv, M. and Saiidi, M.S. (2014) "Next Generation of Bridge Columns for Accelerated Bridge Construction in High Seismic Zones," Center For Civil Engineering Earthquake Research, Department of Civil and Environmental Engineering, University of Nevada, Reno, Nevada, Report No. CCEER-14-06, 400 pp.

Tazarv, M. and Saiidi, M.S. (2016). "Seismic Design of Bridge Columns Incorporating Mechanical Bar Splices in Plastic Hinge Regions," Engineering Structures, DOI: 10.1016/j.engstruct.2016.06.041, Vol 124, pp. 507-520.

Chapter 5. Summary and Conclusions

5.1 Summary

An experimental investigation was performed in the Lohr Structures Laboratory at South Dakota State University to determine the seismic performance of mechanically spliced bridge columns. Four octagonal half-scale bridge columns were designed and tested. One column was a cast-in-place (CIP) to serve as a reference model. Three columns were precast incorporating a mechanical bar splice connection at the column base: a precast column with Dayton Sleeve-Lock couplers (PGD), a precast column with NMB Splice Sleeve couplers (PGS), and a precast column with Dextra Groutec S coupler. All columns were tested the same under a slow cyclic displacement controlled lateral loading to failure. A column was considered failed once one of the following first occurred: (a) longitudinal bar fracture, (b) core concrete failure, and (c) 15% reduction in the lateral load carrying resistance with respect to the peak lateral load.

Furthermore, in-air tensile testing was conducted on each of the mechanical bar splices used in each column to determine their mechanical properties and whether these couplers were "seismic couplers" or not. In a seismic coupler, the failure must be the rupture of the splicing bar outside of the coupler region.

Finally, an analytical study was performed to verify current modeling methods of bridge columns, specifically mechanically spliced bridge columns using finite element

analyses. Pushover analyses were performed to validate the proposed models and to establish the column global performance.

5.2 Conclusion

Based on the experimental and analytical investigations, the following conclusions were drawn from this study:

- CIP showed flexural cracks at until a drift ratio of 3% at which spalling began. Major spalling occurred at large drift ratios leading to longitudinal bar buckling and then bar fracture thus the CIP mode of failure was the longitudinal bar fracture. The CIP lateral load capacity was 65.4 kips (291 kN), and the CIP drift capacity was 8.96%.

- PGD showed flexural cracks at until a drift ratio of 3% at which spalling began. Minor spalling and cracking occurred until the end of the test. The mode of failure for PGD was longitudinal bar pullout from the base of the coupler. The PGD peak lateral force was 74.7 kips (332 kN), and its drift capacity was 4.93%. Unlike CIP, PGD failed due to the longitudinal bar pullout from the coupler whereas CIP failed due to longitudinal bar fracture. The lateral load capacity of PGD was 14% higher than that of CIP, and the drift capacity of PGD was 45% less than that of CIP.

- PGS showed flexural cracks at until a drift ratio of 3% at which spalling began. A spalling continued until the end of the test exposing the couplers and the bars. The mode of failure for PGS was longitudinal bar rupture. The PGS lateral force capacity was 69.6 kips (310 kN), and its drift capacity was 7.81%. PGS and CIP

both failed by longitudinal bar rupture. The lateral force capacity of PGS was 6.4% higher than that of CIP. The displacement capacity of PGS was 13% lower than that of CIP.

- PHD showed flexural cracks throughout the test with some minor spalling occurring during the 4% drift ratio cycle. The mode of failure for PHD was the longitudinal bar pullout from the coupler base. The PHD lateral force capacity was 71.5 kips (318 kN), and its drift capacity was 3.33%. Unlike CIP, PHD failed due to bar pullout whereas CIP failed by bar fracture. The lateral force capacity of PHD was 9% higher than that of CIP. The drift capacity of PGD was 63% less than CIP.

- The pushover analysis for CIP correctly predicted the mode of failure by longitudinal bar rupture. The calculated peak lateral strength was 60.8 kips (270 kN) while the measured lateral strength was 65.4 kips (291 kN), or a 7.0% difference. The calculated failure drift ratio was 8.65% while the measured failure drift ratio was 8.96%, or a 3.5% difference.

- The pushover analysis for PGD predicted the mode of failure by longitudinal bar rupture. The actual mode of failure was bar pullout from the coupler. The calculated peak lateral strength was 69.0 kips (307 kN) while the measured lateral strength was 74.7 kips (332 kN), or a 7.6% difference. The calculated failure drift ratio was 4.93% while the measured failure drift ratio was 4.98% (less than 1% error).

- The pushover analysis for PGS correctly predicted the mode of failure by longitudinal bar rupture. The calculated peak lateral strength was 69.0 kips (307 kN) while the measured lateral strength was 69.6 kips (310 kN), or less than 1% difference. The calculated failure drift ratio was 8.50% while the measured failure drift ratio was 7.81%, or an 8.1% difference.

Since the couplers used in PHD were not seismic couplers per tensile testing performed in this study, the column failure was determined by monitoring the coupler stress-strain behavior not the steel bar outside of the coupler. Using this technique, the PHD calculated peak lateral strength was 70.3 kips (313 kN) while the measured lateral strength was 71.5 kips (318 kN), or a 1.7% difference. The calculated failure drift ratio was 3.52% while the measured failure drift ratio was 3.33%, or a 5.7% difference.

Overall, all mechanically spliced precast columns met the current code seismic requirements thus they are recommended for use in all 50 states of the nation. Furthermore, the cast-in-place and precast models successfully reproduced force-displacement relationships of each column and may be used for the analysis and design of bridge columns incorporating seismic couples.

Chapter 6. References

AASHTO SGS (2011) "AASHTO Guide Specifications for Seismic Bridge Design," Washington, D.C., American Association of State Highway and Transportation Officials.

AASHTO. (2014). "AASHTO Guide Specifications for LRFD Seismic Bridge Design," Washington, DC: American Association of State Highway and Transportation Officials.

ACI 374.2R-13 (2013). "Guide for Testing Reinforced Concrete Structural Elements Under Slowly Applied Simulated Seismic Loads." American Concrete Institute (ACI) Committee 374, Farmington Hills, MI, 2013.

Ameli, M.J., Brown, D.N., Parks, J.E., and Pantelides, C.P. (2014). "Seismic Evaluation of Grouted Splice Sleeve Connections for Precast RC Bridge Piers in ABC." Utah Department of Transportation, Research Division, Report No. UT-14.09.

Ameli, M.J., Brown, D.N., Parks, J.E., and Pantelides, C.P. (2016). "Seismic Column-to Footing Connections Using Grouted Splice Sleeves." ACI Structure Journal, Vol. 113, No. 5, pp.1021-1030

Ameli, M.J. and. Pantelides, C.P (2016). "Seismic Analysis of Precast Concrete Bridge Columns Connected with Grouted Splice Sleeve Connectors." Journal of Structural Engineering, 10.1061/(ASCE)ST.1943-541X.0001678, ASCE, Vol 143, No. 2.

Ameli, M.J. and Pantelides, C.P. (2017). "Seismic Analysis of Precast Concrete Bridge Columns Connected with Grouted Splice Sleeve Connectors." Journal of Structural Engineering, 143(2), p.04016176.

ASTM A706 (2016). "Standard Specification for Low-Alloy Steel Deformed and Plain Bars for Concrete Reinforcement." West Conshohocken, PA, 6 pp.

ASTM A1034 (Sep. 2016). "Standard Test Methods for Testing Mechanical Splices for Steel Reinforcing Bars." ASTM International, West Conshohocken, PA.

ASTM C39/C39M-12. (2012). "Standard Test Method for Compressive Strength of Cylindrical Concrete Specimens," West Conshohocken, PA.

ASTM C109/C109M-11b. (2011). "Standard Test Method for Compressive Strength of Hydraulic Cement Mortars (Using 2-in. or [50-mm] Cube Specimens)," West Conshohocken, PA.

ASTM E8 (2012). "Standard Test Methods for Tension Testing of Metallic Materials." ASTM International, West Conshohocken, PA.

Bompa, D.V., Elghazouli, A.Y. (2019), "Inelastic Behaviour of RC Members Incorporating Threaded Reinforcement Coupler." Engineering Structures, DOI: 10.1016/j.engstruct.2018.11.053, Vol. 180, pp.468-483.

Caltrans. (2019). "Caltrans Seismic Design Criteria (SDC), Version 2.0" Sacramento, CA.: California Department of Transportation, 250 pp.

Dahal, P.K., Tazarv, M., and Wehbe, N. (2019). "Mechanical Bar Splices for Accelerated Construction of Bridge Columns," North Dakota State University - Upper Great Plains Transportation Institute, Fargo: Mountain-Plains Consortium (MPC), MPC Report No. 19-372, 142 pp.

Dahal, P.K., and Tazarv, M. (2020). "Mechanical Bar Splices for Incorporation in Plastic Hinge Regions of RC Members," Construction and Building Materials, Vol. 258, 120308, 17 pp.

Haber, ZB, Saiidi, MS, and Sanders, DH (2013). "Precast Column Footing Connections for Accelerated Bridge Construction in Seismic Zones." Rep. No. CCEER 13-08 Center for Civil Engineering Earthquake Research, Dept. of Civil and Environmental Engineering, Univ. of Nevada, Reno. NV.

Haber, Z.B., Saiidi, M.S. and Sanders, D.H. (2015). "Behavior and Simplified Modeling of Mechanical Reinforcing Bar Splices." ACI Structural Journal, 112(2), p.179.

Hewes, J.T. (2013). "Analysis of the State of the Art of Precast Concrete Bridge Substructure Systems." Arizona. Dept. of Transportation, Research Center, Report No. FHWA-AZ-13-687, 124 pp.

Krawinkler, H. and Moncarz, P.D. (1982). Similitude Requirements for Dynamic Models." ACI Special Publication, Vol. 73, pp. 1-22.

LaVoy, M.R. (2020). "Seismic Performance of Mechanically Spliced Bridge Columns Through Analytical Studies." MS Thesis, South Dakota State University, 106 pp.

Mander, J.B., Priestley, M.J.N., Park, R. (1988). "Theoretical Stress-Strain Model for Confined Concrete," Journal of Structural Engineering, ASCE, Vol. 114, No. 8, pp. 1804-1826.

OpenSees. (2016). "Open System for Earthquake Engineering Simulations," Version 2.4.1, Berkeley, CA, Available online: http://opensees.berkeley.edu.

Saiidi, M.S., Mehraein, M., Shrestha, G., Jordan, E., Itani, A., Tazarv, M., Sanders, D., Murphy, T.M., Reno, M.L., and Pohll, M.N. (2020). "Proposed AASHTO Seismic Specifications for ABC Column Connections," National Academies of Sciences, Engineering, and Medicine, NCHRP Report No. 935, Washington, DC: The National Academies Press, 354 pp.

Tazarv, M. and Saiidi, M.S. (2014) "Next Generation of Bridge Columns for Accelerated Bridge Construction in High Seismic Zones," Center For Civil Engineering Earthquake Research, Department of Civil and Environmental Engineering, University of Nevada, Reno, Nevada, Report No. CCEER-14-06, 400 pp.

Tazarv, M. and Saiidi, M.S. (2016). "Seismic Design of Bridge Columns Incorporating Mechanical Bar Splices in Plastic Hinge Regions," Engineering Structures, DOI: 10.1016/j.engstruct.2016.06.041, Vol 124, pp. 507-520.

Wang, Z., Qu, H., Li, T., Wei, H., Wang, H., Duan, H. (2018). "Quasi-Static Cyclic Tests of Precast Bridge Columns with Different Connection Details for High Seismic Zones," Engineering Structures, DOI: 10.1016/j.engstruct.2017.12.035, Vol 158, pp. 13-27.